# Development and Validation of a Parametric Mandible Reconstruction Plate Design Method

by
Brett Ian Giddy

*Thesis presented in partial fulfilment of the requirements for the degree of*
*Master of Engineering (Mechanical) in the*
*Faculty of Engineering at Stellenbosch University*

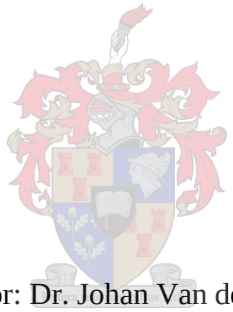

Supervisor: Dr. Johan Van der Merwe

March 2021

# Declaration

By submitting this thesis electronically, I declare that the entirety of the work therein is my own, original work, that I am the sole author thereof (save to the extent explicitly otherwise stated), that reproduction and publication thereof by Stellenbosch University will not infringe any third-party rights and that I have not previously in its entirety or in part submitted for obtaining any qualification.

Date: . . . . . March 2021 . . . . . .

# Abstract

**Parametric Mandible Reconstruction Plate**

BI Giddy

*Department of Mechanical and Mechatronic Engineering,*

*Stellenbosch University,*

*Private Bag X1, Matieland 7602, South Africa*

Thesis: MEng (Mechanical)

March 2021

This study investigated the feasibility and attempted to develop a parametric mandible reconstruction plate design method in order to reduce surgical lead time, improve fit and structural performances. This method includes a CAD template that accepts a range of realistic mandible dimensions as the input. The output is a 3-dimensional mandible reconstruction plate. A reconstruction plate/mandible comparison test was performed on several combinations in order to determine whether the parametric plate provided a suitable alternative to conventional reconstruction plates in terms of fit and structural performance. 37 male and 37 female random mandibles were generated and measured. These measurements were used to create the corresponding parametric plates. The plates were aligned with their mandibles and the Hausdorff distances were recorded. A Finite Element Analysis was performed on the male and female mandibles which exhibited the most curvature, with three common plate configurations in literature. All boundary conditions such as the displacements, supports, muscle force vectors and magnitudes, as well as mandible and plate material properties were taken from literature.

The comparison test indicated that the parametric plate provides a reasonable approximation of mandible geometry. The mean mandible plate deviation for lateral short and symphyseal plates was less than 2 mm for the male and female configurations. The mean hemimandible plate deviation was less than 2.6 mm for both the male and female plates. Some bending may be required due to the irregularities in mandible geometry, however significantly less than what is required to shape the commercial straight mandible reconstruction plate. The Finite Element Analysis results indicate that the maximum Von-mises stresses in parametric plate were noticeably lower in all three plate configurations when compared to the commercial straight reconstruction plates. The lowest recorded maximum stress recorded in the parametric plates was in the male symphyseal plate at 102.31 MPa. The highest maximum stress recorded in the parametric plates was in the female hemimandible plate at 623.38 MPa. Whereas the respective stresses in the commercial straight plates were 223.09 MPa in the male symphyseal and 652.25 MPa in the female hemimandible plates. Reaction values were compared with hand calculations as a means of model validation.

# Uittreksel

**Parametriese Kakebeen Rekonstruksie Plaat**

BI Giddy

*Departmente van Meganiese en Megatroniese Ingenieurswese,*

*Universiteit van Stellenbosch,*

*Privaat Saak X1, Matieland 7602, Suid Afrika*

Tesis: MIng (Meganiese)

Maart 2021

Hierdie studie ondersoek die vermoeë en probeer om 'n parametriese kakebeen rekonstruksieplaat te ontwikkel om chirurgiese lei tyd te verminder, sowel as die pas en strukturele prestasie te verbeter. Hierdie metode bevat ‘n CAD-sjabloon wat ‘n reeks realistiese onderkaakafmetings aanvaar as die insette. Die uitset is 'n driedimensionele onderkaakrekonstruksieplaat. 'n Rekonstruksieplaat / kakebeen vergelykingstoets is op verskeie kombinasies uitgevoer om vas te stel of die parametriese plaat 'n geskikte alternatief vir konvensionele rekonstruksieplate bied wat pas en strukturele prestasie betref. 37 manlike en 37 vroulike kakebene is gegenereer en gemeet. Hierdie metings is gebruik om die ooreenstemmende parametriese plate te skep. Die borde is in lyn gebring met hul kakebene en die Hausdorff-afstande is aangeteken. 'n Eindige elementanalise-simulasie is uitgevoer op die manlike en vroulike onderkaak wat die meeste kromming vertoon, met drie algemene plaatkonfigurasies in die literatuur. Alle randtoestande soos verplasings, drade, spierkragvektore, groottes, onderkaak en plaatmateriaal-eienskappe is uit die literatuur geneem.

Die vergelykingstoets het aangedui dat die parametriese plaat 'n redelike benadering van die kakebene geometrie bied. Die gemiddelde afwyking van die rekonstruksieplaat vir laterale kort en simfisiese plate was minder as 2 mm vir die manline en vroulike konfigurasie. Die gemiddelde afwyking van die halwe-kakebeen plaat was minder as 2.6 mm vir beide die manlike en vroulike plate. Moontlike buiging kan nodig wees as gevolg van die onreëlmatighede in die onderkaakgeometrie, maar aansienlik minder as wat nodig is om die kommersiële onderkaakrekonstruksieplaat te vorm. Die resultate van die eindige elementanalise dui aan dat die maksimum Von-mises spanning in die parametriese plaat opvallend laer was in al drie plaatkonfigurasies in vergelyking met die kommersiële reguit rekonstruksieplate. Die laagste aangetekende maksimum spanning wat in die parametriese plate aangeteken is, was in die manlike simifisiese plaat op 102.31 MPa. Die hoogste maksimum spanning wat in die parametriese plate aangeteken is, was in die vroulike halwe-kakebeen plaat op 623.38 MPa. Terwyl die oderskeie spannings in die kommersiële reguit plate 223,09 MPa in die manlike en simfisiese was en 652.25 MPa in die vroulike halwe-kakebeen plate. Reaksiewaardes is vergelyk met handberekeninge as 'n middel vir model validering.

# Acknowledgements

Dr. J Van der Merwe. Thank you for providing such an excellent topic that was incredibly interesting from start to finish. Thank you for accepting me as a student despite my late application! I would not have been able to complete this project without your patience, support, and advice. Thank you again.

To the BERG faculty and students, thank you for the good times and the laughs. They were very much needed.

Finally, thanks to my Mom and my late Grandmother. Without your support I would never have made it this far. There are no words to describe my appreciation.

# Contents

# List of Figures

# List of Tables

# Nomenclature

## Symbols

| | | |
|---|---|---|
| • E | Young's Modulus | GPa |
| • ΔT | Change in Temperature | ˚C |
| • μ | Mean | |
| • υ | Poisson's Ratio | |
| • ρ | Density | $kg/m^3$ |
| • σ | Standard Deviation. | |
| • σ* | Stress | MPa |

## Abbreviations

- 2D 2-Dimensional
- 3D 3-Dimensional
- ATP Adenosine Triphosphate
- CAD Computer Aided Design
- CS Commercial Straight
- CT Computerized Tomography
- FEA Finite Element Analysis
- FEM Finite Element Method
- MRI Magnetic Resonance Imaging
- NH Novel Hybrid
- PCA Principal Component Analysis
- PDE Partial Differential Equations
- PET Positron Emission Tomography
- RMS Root Mean Square
- SSM Statistical Shape Model
- STL Stereolithography
- TMJ Temporomandibular Joint
- TML Temporomandibular Ligament

# 1. Introduction

## 1.1. Background

A mandible implant is required when there has been damage to the mandible structure which can have adverse effects on the patient's quality of life. The damage can refer to deformation in the mandible due to tumorous growths, missing mandible sections due to tumor resection or severe trauma from vehicle collisions, sports injuries, falls and assaults. Unrepaired defects can cause mastication difficulties, disfigurement, and loss of speech. The goals the surgeon aims to achieve during reconstructive surgery are to establish continuity, establish alveolar height, arch form, arch width, maintain bones, and improve facial contours (Lin, Lin and Jeng, 2011). Factors that may affect the reconstruction process include the condition of the temporomandibular joint and distribution of remaining bone. The more specific problem relates to implant rejection or failure. Conventional implants are intraoperatively bent to fit the patient. These implants often suffer from a lack of bone infusion, plate fracture, bleeding, and structural failure at the bending site.

## 1.2. Motivation

Patient-specific implants can overcome the disadvantages of intraoperatively bent reconstruction plates by pre-forming the implant to the patient's geometry during planning. This leads to reduced surgery time, improved fit and eliminates plastic deformation. The preparation for such an implant is more complex than previous reconstructive methods. It requires knowledgeable designers, surgeons, and experience to produce an effective implant. From start to finish, it is more costly than off-the-shelf designs such as titanium plates. A middle ground between a conventional and patient specific implant design approach would be to complete time-consuming activities before the first consultation with the patient, while still allowing some degree of customization afterwards. One way to achieve this is by developing a parametrized, adjustable implant model based on mandible parameters which have been pre-determined and pre-validated using population-based data. These parameters will accept mandible dimensions as input. Finally, the CAD model will produce an implant that reproduces a healthy mandible shape, which can then be manufactured. This study does not include a cost analysis and clinical evaluation. However, literature evidence suggests that patient-specific reconstruction plates do offer a decreased lead time and increased cost. Removing the design-heavy elements associated with patient-specific plates by using a parametric model the cost should be reduced as well. This study will focus on generating a design that works and meets performance measurements associated with reconstruction plates in general, such as that are structurally strong and fit well. Specific performance measures will be given in the relevant sections.

## 1.3. Aim and Objectives

The aim of this project is to develop and validate a parametric mandible reconstruction plate design method. The specific objectives are:

1. Develop a CAD template that accepts mandible measurements as parameters and produces the corresponding Mandible Reconstruction Plate (MRP),

2. Investigate and refine the fit of the parametric MRP compared to a sample population of mandibles and compare these to their corresponding MRPs. Record the measurements of fit and compare to values in literature.
3. Investigate the structural strength of a pre-formed MRP in comparison with straight plates bent to fit patient geometry. Compare maximum Von-mises stresses to literature and determine whether the parametric design method successfully reduces these stresses.

# 2. Literature Study

This chapter begins with the anatomy and pathology of the mandible, offering background on the sub-systems of the mandible and common ailments. Information on the cephalometric analysis and implant design processes is provided. Finally, the trends in relevant FEA literature are discussed.

## 2.1. Anatomy of the Mandible

The mandible, more commonly referred to as the lower jaw or the jawbone, is the strongest bone in the human face. It is located below the maxilla (upper jaw) and is one of the few bones in the human skull capable of movement (Standring and Gray, 2008). A short description of the mandible regions are given below.

Figure 1 shows the anatomy of the mandible. The body of the mandible, viewed from above, is curved and defines the jawline. The ramus extends cranially (superiorly, towards the skulls) at an angle of 110 degrees. The meeting of the ramus and the body is known as the gonial angle, which is ± 90 degrees and ± 110 degrees in adult men and women respectrively (Breeland and Patel, 2019). The ramus serves as the attachment site for various facial muscles and ligaments. The masseter muscle attaches laterally to the ramus and facillitates mastication (chewing). The medial pterygoid muscle attaches to the inner face of the ramus and facillitates closing of the jaw, assists in mastication and to a lesser degree contributes to the protrusion of the mandible (underbite). The ramus divides into two processes, with the coronoid process located anteriorly (towards the front) and the condylar process located posteriorly (towards the rear). Above the condylar process is the ball-and-socket joint, the temporomandibularjoint (TMJ). This joint is responisible for the movement of the mandible such as opening, closing and protrusion. The coronoid process attaches to the temporalis muscle. Although the cornoid process is not in direct contact with the TMJ, it is the attrachment site for of the mandibular muscles. This attachment point facillates the opening and closing of the jaw as well as mastication. The condylar process forms the lower portion of the TMJ. It is more slender than the coronoid process with a large, ball-shaped protrusion on top. This allows for the interaction with the TMJ as well as attachment for the lateral pterygoid muscle. The lateral pterygoid muscle is the main muscle involved in speech and the opening and closing of the jaw.

The alveolar process supports the teeth via a fibrous, mobile peg-and-socket gomphosis joint (Encyclopedia Britannica, 2019). The teeth are for chewing and cutting, they aid in speech and pronunciation as well as provide support for the facial tissue. The alveolar process extends upward from the body of the mandible. The process is symmetrically shaped like a V (when viewed laterally), consisting of two bony plates – the *buccal*, outer, and *lingual*, inner plates. Foramina are cavities in the mandible which allow for transport of the cranial nerve and blood vessel structures. The mandibular foramen is the passage for the inferior alveolar nerve and artery. The mental foramen is

the outer surface of the body which allows for the inferior alveolar nerve and artery to exit the posterior canal and become the mental nerve and artery. The mandibular nerve, is the largest division of the trigeminal nerve. The nerve subdivides into a small, anterior, and a large, posterior, trunk. The anterior trunk branches to the mandible muscles while the posterior trunk branches to three sensory divisions. The auriculotemporal nerve provides sensory innervation the regions on the side of the head, the lingual nerve provides sensory innervation to the anterior two thirds of the tongue and the inferior alveolar nerve provides sensation to the lower teeth.

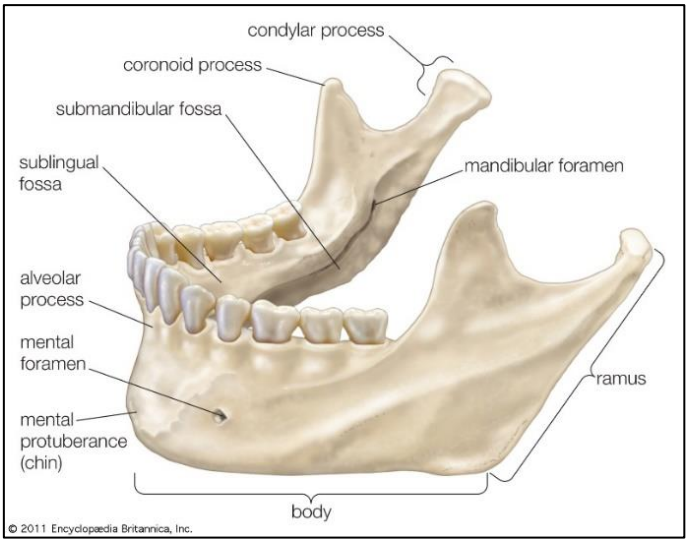


*Figure 1: Mandible Anatomy (Encyclopedia Britannica, 2019)*

## 2.2. Material Properties of Bone Tissue

Bone is not uniformly solid but is comprised of several layers. Cortical Bone is the hard, outer layer also known as compact bone. It has a higher density than trabecular bone, is smooth and white in appearance, and accounts for up to 80% of an adult's total bone mass. Cortical bone is covered by an outer layer called the periosteum and an inner layer called the endosteum. The periosteum serves as a protective layer as well as providing vascular support to the cortical bone tissue while the endosteum is a vascular membrane that separates the cortical and trabecular layers. Trabecular Bone is the spongy, inner layer of bone. It is less dense and more porous than cortical bone allowing for more

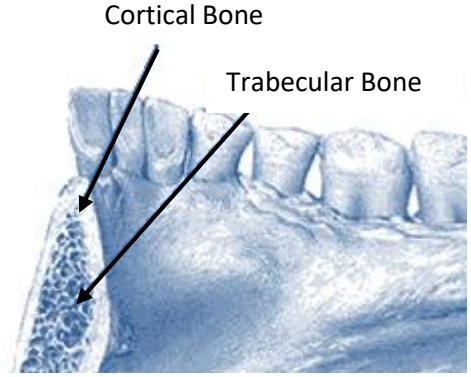


*Figure 2: Mandibular Bone Layers (Illustration: BI Giddy)*

flexibility but less strength. Trabecular bone is highly vascularized and is typically found at the end of long bones and near joints. Figure 2 shows the bone layers in the mandible.

The modulus of compact bone ranges from 10 – 20 GPa (van Eijden, 2000). In trabecular bone (spongy, porous bone) elastic modulus values range from 0.76 – 20 GPa depending on bone density and loading (Turner et al., 1990). Rho, Ashman and Turner (1993) tested 450 trabecular bone samples and 256 cortical bone samples using ultrasonic and microtensile testing. Elastic moduli of 14.8 GPa and 10.4 GPa were observed for ultrasonic and mechanical testing respectively, for trabecular bone, while elastic moduli of 20.7 GPa and 18.6 GPa were observed for ultrasonic and mechanical testing, respectively, for cortical bone.

In bone, the breaking strength is substituted for yield strength. The yield strength will vary depending on the loading type. Reilly and Burstein (1975) reported that the yield strength in femoral cortical bone under shear as 67 MPa, 135 MPa under tensile stress and 205 MPa under compressive stress. This indicates that bone is weakest in shear and strongest under compression.

## 2.3. Temporomandibular Joint

The temporomandibular joint (TMJ) is a complex synovial joint that serves as the interface between the mandible and the skull. It consists of the mandibular condyles and the squamous temporal bone above, located on the lateral skull. The articulation space of the TMJ is divided into an upper and lower compartment by the articular disc which is comprised of dense fibrous connective tissue with varying amounts of fibrocartilage. Translation (retraction or protrusion of the mandible) occurs primarily in the upper compartment, while the lower compartment functions as a rotary joint (elevation and depression of the mandible). Load bearing synovial joints such as the hip or shoulder have hyaline cartilage (glass-like, smooth cartilage that allows joints to glide) lining their articulation surfaces. The articulation surfaces of the TMJ are lined with avascular, fibrous connective tissue. This has led some researchers to assume that the TMJ must not experience any loading or stress (Hylander, 2006). However, there is evidence that indicates that the TMJ is in fact a load-bearing joint (Carlson and Ribbens, 1985; Hylander, 2006)

### 2.3.1. Mandibular Condyle and Articular Disc

The lower compartment of the TMJ consists of the mandibular condyle. The articular surface of the condyle is the super-anterior surface, illustrated in Figure 3. The lateral surface of the condyle protrudes slightly beyond the lateral surface of the ramus and serves as the attachment site for the temporomandibular ligament (TML). The condyle is in contact with is the articular disc, a dense block of connective tissue that is positioned between the condyle and the glenoid fossa. The articular disc divides the TMJ into an upper and lower compartment. The main function of the articular disc is to distribute the reaction forces of the TMJ more evenly along the surfaces of the joint, helping to reduce the stress concentrations between the condyle and articulation surfaces (McNeill, 1997).

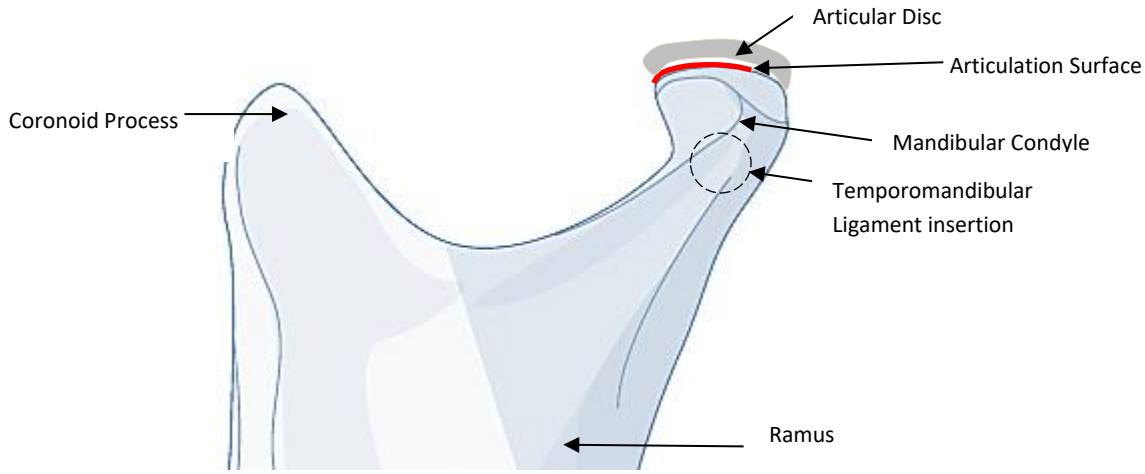


*Figure 3: Temporomandibular Joint Structure (Illustration: BI Giddy)*

### 2.3.2. Glenoid Fossa and Articular Eminence

The glenoid fossa, also known as the mandibular fossa, is the cavity in the squamous temporal bone that houses the mandibular condyle. The posterior wall is formed by the tympanic plate, the anterior wall is formed by the articular eminence and the superior wall is formed by the squamous temporal bone. The roof of the glenoid is paper thin and often appears translucent under light, indicating that the roof of the glenoid fossa is not the main load-bearing portion of the TMJ (Walia et al., 2014). The articular eminence is the posterior root of the zygomatic arch and the anterior wall of the articular fossa (anterior wall of the glenoid fossa lined with articular tissue). It is adjacent to the articular tubercle and while the eminence is involved in joint articulation, the tubercle serves as another attachment site for the TML. The fibrous tissue covering this dense, saddle-shaped element of the TMJ is thick and firm, providing a smooth articulation surface. The morphology of the articular eminence indicates routine loading due to joint reaction forces produced by the TMJ elements (Hylander, 2006). Figure 4 shows the lateral view of the TMJ.

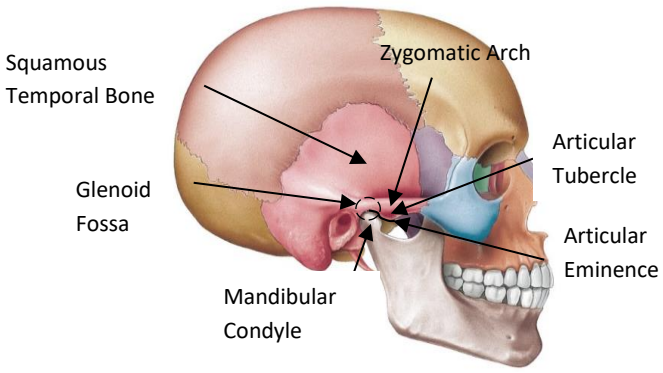


*Figure 4: Lateral View of the TMJ (Koen, 2013)*

### 2.3.3. Articular Capsule

The articular capsule is a fibrous sheath that houses the elements of the TMJ. The capsule is anchored to the articular eminence and the neck of the mandibular condyle. The articular capsule is relatively thin medially and posteriorly but thickens laterally. This lateral thickening of the articular capsule attaches to the articular tubercle and forms the TML (Dubrul, 1988). The TML is thicker above, nearer to the zygomatic insertion, than below. The main functions of the TML and articular capsule are to prevent excessive displacement of the mandible. The vertical fibers of the capsule limit the ability of the condyle to distract form the articular eminence, the horizonal fibers of the TML limit retrusive movements of the mandible and the posterior fibers of the capsule and TML limit protrusion of the mandible (Hylander, 2006). Figure 5 shows the anatomy of the articular capsule.

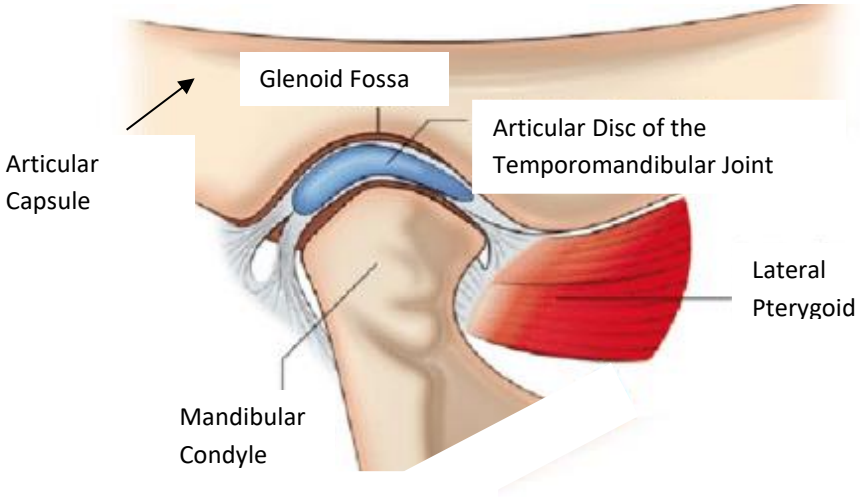


*Figure 5: Articular Capsule Anatomy (Emes, Aybar and Dergin, 2018)*

The TML also prevents the mandibular condyle from being driven upward and fracturing the base of the skull (Orthopaedicsone.com, 2019). Synovial tissue lines the inner surface of the capsule. TMJ blood supply, specifically the disc and capsule, is provided by a maxillary artery. The innervation of the TMJ is derived from the auriculotemporal and masseteric nerves which stem from the mandibular branch of the trigeminal nerve (Davidson et al., 2003).

### 2.3.4. Accessory Ligaments

There are two accessory ligaments associated with the TMJ and the articulation of the joint. The Sphenomandibular Ligament originates from the spine of the sphenoid bone and directs inferiorly and laterally. It inserts two thirds of the way up the ramus in a region known as the mandibular lingula. It has no influence on mandibular movements but serves to protect mandibular blood vessels and nerves passing through the mandibular foramen during depression and elevation of the mandible (Schwartz, 1959). The Stylomandibular Ligament is a sheet that extends from the styloid process and inserts on the inferior-posterior region of the ramus. Other fibers of the stylomandibular ligament insert onto the medial surface of the medial pterygoid muscle. This ligament is inactive during opening and closing of the mandible. It tenses when the mandible is maximally protruded, limiting protrusive

movements from damaging the mandible muscles and the TMJ (Hylander, 2006). Figure 6 shows the TMJ ligaments as well as their origin and insertion points.

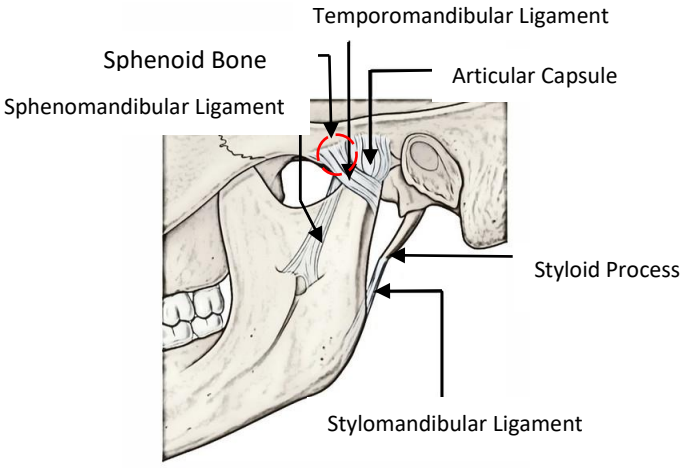


*Figure 6: Internal View of the TMJ (Dashnyam et al., 2018)*

## 2.4. Muscles of the Mandible

There are four muscles attached to the mandible. They are commonly referred to as the masticatory muscles. However, there are muscles in the face, tongue and palate that act in conjunction with these muscles to facilitate mastication (Hylander, 2006). The muscles attached to the mandible will simply be referred to as the mandibular muscles. The mandibular muscles generate different loadings on the mandible depending on where the bite force is located. Under the stress and strain patterns that the mandible experiences the superior portion of the mandible is generally designated as the tension zone and the inferior portion is the compression zone (Petrova et al., 2016), shown in Figure 7.

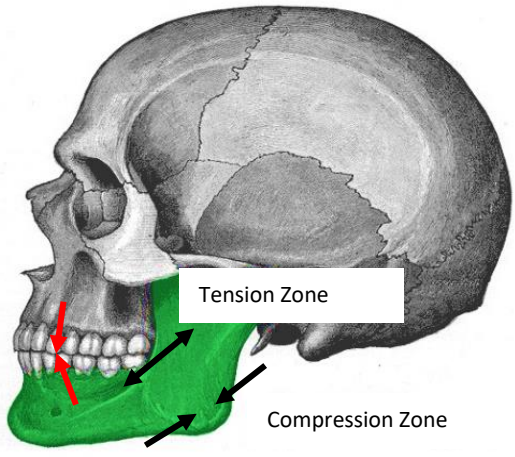


*Figure 7: Stress Zones of the Mandible (Petrova et al., 2016)*

### 2.4.1. Masseter Muscle

The masseter muscle is powerful muscle that assists in the chewing of plant matter. This muscle consists of two sections, a superficial and deep masseter muscle, shown in Figure 8. The masseter muscle is an elevator of the mandible. Hylander (2006) states that the masseter muscle, as a whole, exerts a lateral force on the mandible. Both muscle divisions originate at the zygomatic arch. The superficial head extends along two thirds of the zygomatic arch and inserts along the angle of the mandible and the lower third, lateral surface, of the ramus. The deep head of the masseter muscle is larger and more muscular in texture. It extends from the remaining third of the zygomatic arch and inserts along the superior portion of the ramus, sometimes as high as the coronoid process. Some of the fibers of the deep head radiate from the TMJ capsule (Meyenberg, Kubik and Palla, 1986).

The innervation of all the mandibular muscles is provided by the trigeminal nerve (Barral and Croibier, 2009; Washmuth, 2019): The mandibular branch of the trigeminal nerve is responsible for the innervation of the masseter muscle. It also includes a sensory filament that terminates in the TMJ (Barral and Croibier, 2009).

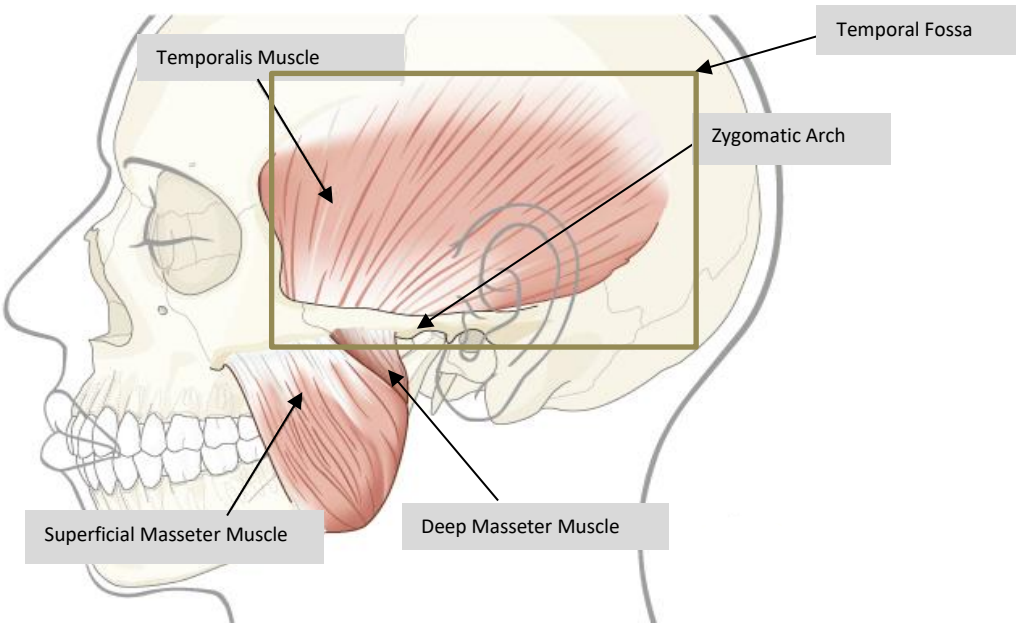


*Figure 8: Lateral View of the Skull (Matic and Yao, 2019)*

### 2.4.2. Temporalis Muscle

The temporalis muscle is a wide, “fan-shaped” muscle that originates from the temporal fossa. The temporal fossa is a shallow depression bounded by the temporal lines which terminates just below the zygomatic arch. The bundles of temporalis muscle fibers continue towards the temporal foramen (the opening located between the lateral surface of the skull and the zygomatic arch) and insert at the coronoid process of the mandible, which extends into the temporal foramen. The anterior fibers of the temporalis, which are the major bulk of the temporalis, are vertical; the medial fibers are oblique, the posterior fibers are largely horizontal and bend around the zygomatic arch, continuing vertically downwards towards the mandible (Hylander, 2006).

Due to the “fan-shaped” muscle the direction of pull and consequently the directional forces varies depending on which sections of the muscle are mechanically active (Van Eijden, 1990). Posterior fibers of the temporalis primarily exert an upward force on the mandible but due to the proximity of the posterior fibers to the mandibular condyle, they also act as a stabilizer of the TMJ (Hylander, 2006). The anterior and medial portions of the temporalis are capable of a vertical and retracting pull, a forward pull and finally the deep fibers of the anterior temporalis can pull the mandible medially (Gatterman, 2012). The middle and posterior fibers insert along the crown of the coronoid process and along the posterior slope, while the anterior fibers insert along the crown of the coronoid process, the anterior slope and the most superior part of the mandibular ramus. Figure 9 illustrates this. Another insertion point for the temporalis is the retromolar fossa. This is a small depression located posteriorly to the wisdom tooth.

The temporalis muscle is covered by the temporal fascia, a strong fibrous sheet that is divided into easily distinguishable deep and superficial layers. The function of the temporal fascia is to enclose the structure of the temporalis into discrete patterns (Lam and Carlson, 2014) and the combination of superficial and deep layers allows the scalp to maintain structural integrity with necessary mobility (Bohr and Shermetaro, 2019). Similar to the masseter muscle, the temporalis muscle elevates the mandible and is innervated by the anterior trunk of the trigeminal nerve.

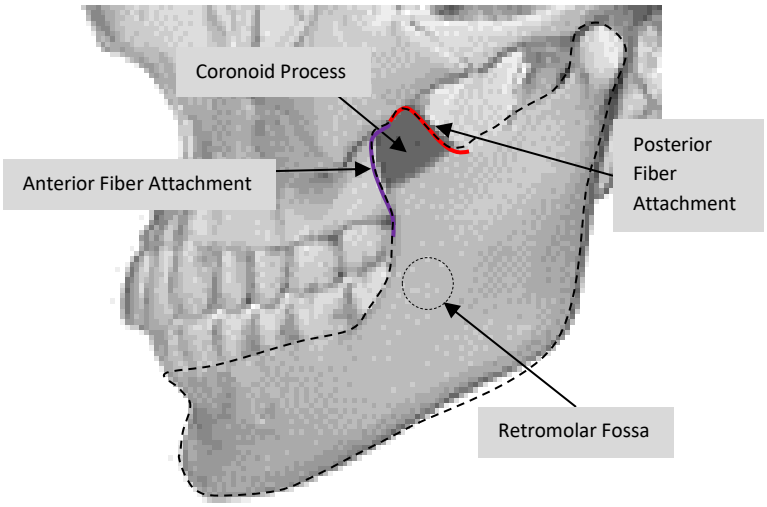


*Figure 9: Temporalis Attachment Sites (Illustration: BI Giddy)*

### 2.4.3. Medial Pterygoid Muscle

The medial pterygoid muscle is located on the inner face of the mandibular ramus. Viewed laterally, it is the anatomical counterpart of the masseter muscle. The medial pterygoid muscle is an elevator of the mandible and exerts a medial force component on the mandible, as opposed to the masseter muscle which exerts a lateral force (Hylander, 2006). The medial pterygoid muscle, similar to the masseter muscle, has two heads. The main portion of muscle fibers originates as the deep head above the inner surface of the lateral pterygoid plate. The smaller bundle of fibers, known as the superficial head, originate from the maxillary tuberosity and the pyramidal process of the palatine bone. The muscle fibers of the medial pterygoid angle downwards towards the mandible and insert into the lower back portion of the ramus and angle of the mandible. The medial fibers and the masseter fibers form a tendinous connection below the mandibular angle known as the pterygomasseteric sling (Klineberg and Eckert, 2016). The medial pterygoid is innervated by the mandibular branch of the trigeminal nerve. Figure 10 shows the region of the skull associated with the medial pterygoid.

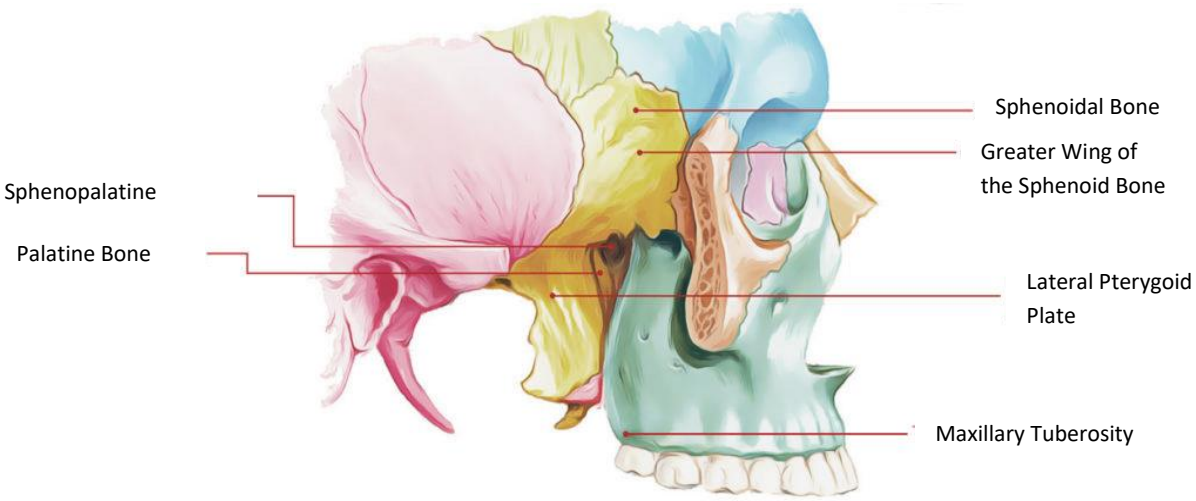


*Figure 10: Skull Anatomy Associated with the Medial Pterygoid (Earth's Lab, 2019)*

### 2.4.4. Lateral Pterygoid Muscle

The lateral pterygoid muscle consists of two heads. The inferior head of the muscle is three times larger than the superior head (Honée, 1972). The superior pterygoid originates from the temporal surface of the greater wing of the sphenoid bone and the inferior head originates from the lateral surface of the lateral pterygoid plate. The fibers of the superior head run posteriorly at an angle of 45 degrees relative to the inferior head, while the inferior head remains almost horizontal to point of insertion. While the lateral pterygoid muscle begins as two distinct heads the superior and inferior portions fuse together in front of the TMJ (Carpentier et al., 1988). The fibers of the superior head insert onto the articular disc and fibrous capsule of the TMJ, while the inferior fibers insert onto the neck of the condylar process.

The function of the lateral pterygoid muscle ambiguous. Gibbs et al. (1984) state that the superior head contracts the mandible during closure, and Wood, Takada and Hannam (1986) state that the inferior head contracts during protraction, opening and shifting the mandible to either side. This

would indicate that each head performs specific functions. Koolstra, Naeije and Van Eijden (2001) consider the lateral pterygoid muscle as two sperate muscles, the superior and inferior part. Due to muscles being anatomically named and not functionally named this method of separating the muscle is not preferred (Hylander, 2006). To simplify the functional aspect of the lateral pterygoid, the superior and inferior portion are analyzed together. Therefore, the primary function of the lateral pterygoid muscle is to pull the condylar head out of the mandibular fossa to facilitate protrusion of the mandible. This movement causes a forward and medially directed force on the mandible. The lateral pterygoid also assists in stabilizing the condyle during biting and mastication (Sava and Scutariu, 2012). The lateral pterygoid muscle is the only mandibular muscle to assist in depressing the mandible (Kenhub, 2019). Similar to the other mandibular muscles, the lateral pterygoid is innervated by the trigeminal nerve, specifically, the *lateral pterygoid nerve* which is a branch of the mandibular nerve.

## 2.5. Pathology of the Mandible

Pathology refers to the study of disease. It underlies all aspects of patient care, from diagnosis and testing to treatment, and treatment technology (Rcpath.org, 2019). Mandible Pathology includes diseases such as *Osteomyelitis*, tumors, cysts, and lesions of the mandible structure (Chi et al., 2019). While mandible fractures are not diseases, they are important to consider when one talks about the pathology of the mandible as mandible fractures can be severe.

Initially when making a diagnosis of a mandible lesion the surgeon will begin by taking a medical history and a physical examination of the patient's jaw, mouth and teeth. Given the large spectrum of pathologic features of the mandible it is crucial that image findings are corroborated with a biopsy, as some malignant lesions present the same as benign lesions on images and vice-versa.

### 2.5.1. Inflammatory Conditions

Osteomyelitis is a broad term used to describe infection of the bone due to a number of causes, such as traumatic injuries or chemical substances. Symptoms of osteomyelitis appear when pus has invaded the bone layers and compromised the local blood supply. This leads to bone necrosis which is a classic sign of osteomyelitis. Common forms of Osteomyelitis include *Primary Chronic Osteomyelitis (PCO)* and *Chronic Suppurative Osteomyelitis (CSO)*. The diseases differ in that PCO does not characteristically sequestrate, and PCO does not have an obvious cause (such as bacterial infection in the case of CSO). *Alveolar Osteitis* begins to appear after tooth extraction. A blood clot is formed and slow destruction of the clot at the extraction site delays healing and leads to *Alveolar Osteitis*.

### 2.5.2. Odontogenic and Non-Odontogenic Cysts

Mandible cysts and lesions are either odontogenic or non-odontogenic. Odontogenic cysts are mandible cysts that form from odontogenic tissue (tissue involved in tooth development). Odontogenic cysts can be classified into three groups (Morrison, 2019):

- Inflammatory: These cysts typically present in teeth bearing areas of the mandible. More precise locations depend on the type of cyst.
- Developmental: Developmental and neoplastic cysts present in various locations across the mandible and maxilla. Once more, precise locations depend on cyst type.
- Neoplastic: Uncontrolled division of cells.

Odontogenic epithelial tissue is crucial for proper tooth development. Once epithelial tissue has completed tooth formation it degenerates to epithelial rests (residual epithelial tissue that does not completely disappear). Common odontogenic tumors are inflammatory cysts such as a *Residual Cyst*. This cyst is caused by fibrous and granulated tissue originating at the surrounding region of a tooth. If this fibrous tissue is not removed before dental extraction a residual cyst such as a *Calcifying Odontogenic Cyst (COC)* may form. This cyst is a benign ameloblastoma-like (ameloblastoma refers to a cyst originating from tooth enamel) group of cells which calcify. COC's are rare with an occurrence rate of 5% and very rarely does the tumor transform to malignant (Motosugi et al., 2009).

Developmental cysts such as a *Dentigerous Cyst* originate from the crown of an unerupted tooth. The pressure exerted by the tooth on the dental follicle can potentially obstruct local blood flow causing fluid buildup and ultimately a cyst. Complications that can arise from untreated dentigerous cysts are ameloblastoma or in more severe cases squamous cell carcinoma, a type of malignant tumor (Magliocca and Morrison, 2019).

Non-odontogenic cysts, sometimes referred to as *Fissural Cysts* are, as previously stated, cysts that are not involved in tissue related to tooth formation. The term fissural cysts apply only to cysts that arise from cell remnants within the fusion lines of the facial processes (Med-college.de, 2019). Developmental and odontogenic cysts are more common in the pediatric population, with non-odontogenic relatively rare (Jones and Dillon, 2016). Non-odontogenic cysts are typically caused by the inclusion of foreign material or epithelial tissue in the lines of closure during the developmental phase of the facial features and structures (Med-college.de, 2019). The sites for non-odontogenic cysts are as follows (Martinez and Magliocca, 2019):

- Epidermoid Cyst: Floor of the mouth
- Dermoid Cyst: Soft tissue of the floor of the mouth
- Globulomaxillary Cyst: Located between the maxillary lateral incisor and canine teeth
- Median Palatine Cyst: Midline of the hard palate
- Nasolabial Cyst: Nasolabial region
- Nasopalatine duct cyst: Anterior midline of the hard palate
- Palatine Cyst: Midline of soft palate tissue

The most common non-odontogenic cysts are the *Traumatic Bone Cavity* (cyst commonly linked to trauma)*, Aneurysmal Bone Cyst* (cyst commonly found in bone)*, Nasopalatine Cyst and Nasolabial Cyst* (Jones and Dillon, 2016).

### 2.5.3. Benign and Malignant Tumors

Tumors are an abnormal growth of cells. While cysts are almost always benign, tumors can be benign or malignant. Benign tumors remain in one place while malignant tumors spread and cause new tumors to appear in other parts of the body. Tumors are almost always diagnosed in two parts. An image is taken of the tumor (MRI, CT, X-ray, PET), and should the doctor or physician suspect cancer, a biopsy will be performed (extraction of sample cells for examination). The following are examples of benign and malignant tumors provided by literature from Chi et al., (2019).

Benign Tumors:

- *Adenomatoid Odontogenic Tumor*:
  This is also known as adenoameloblastoma, is relatively uncommon. It is more common in the young population, while two thirds of the cases are found in females (Pernick, 2019). Diagnosis is straightforward with a well-defined lesion surrounding the crown of an unerupted tooth.
- *Ameloblastic Fibroma*:
  Ameloblastic fibroma is a rare tumor compromising of epithelial and mesenchymal (connective) tissue. This type of tumor usually occurs in patients who are 20 years old or less (Pernick, 2019). While associated with an unerupted tooth this tumor can occur anywhere in the mandible or maxilla but more commonly in the posterior region of the mandible. Widely considered benign with low recurrence and malignant transformations rates, literature may suggest that this lesion has great potential for recurrence and malignant transformation (Ponnam, Srivastava and Smitha, 2012).
- *Ameloblastoma*:
  This locally aggressive tumor of the odontogenic tissue has a 25 - 35% recurrence rate. It is the second most common odontogenic tumor (after odontoma). It is found equally in men and women with a mean age-of-appearance of 39 years (Magliocca and Martinez, 2019). 80% of all ameloblastomas are found on the mandible, with two thirds occurring along the posterior region of the mandible. Often overlooked, this tumor is asymptomatic, discovery usually occurs during routine dental examinations or when the swelling reaches a noticeable level.

Malignant Tumors:

- *Ameloblastic Fibrosarcoma*:
  An Ameloblastic fibrosarcoma is a rare (less than 100 reported cases in English literature) *mixed* tumor consisting of a benign epithelial component and a malignant connective tissue component. 80% of cases are found in the posterior mandible however, being malignant the maxillary area can be involved, and it has been known to spread to the sinus (Magliocca and Martinez, 2019). This tumor appears as a multilocular (many compartments) radiolucent lesion on imaging scans, with pain and swelling experienced in the affected area (Loya-Solis et

al., 2015). The terminology differs depending on the tissue present in the malignant portion, or stroma, of the tumor.

- *Osteosarcoma*:
  Osteosarcoma is the most common type of cancer found in bones (Mayo Clinic, 2019). It is a malignant tumor where the tumor cells constantly produce osteoid (bone). *Chondroblastic Osteosarcoma* is a subtype of osteosarcoma that contains a cartilaginous component. Complete surgical resection of the affected area is the treatment of choice in osteosarcoma (Jaffe, Bruland and Bielack, 2009). Chemotherapy is used to kill remaining cancer cells and to reduce the risk of recurrence. Should the limb damage be severe enough the option to have rotationplasty (the affected limb is removed, and the non-involved portion is rotated and reattached) after tumor resection exists, this greatly improves mobility and functional aspects especially in younger patients as the usual methods of reconstruction are not applicable (Jacobs, 1984). Craniofacial osteosarcomas account for ± 7% of all osteosarcomas with 25% of these craniofacial osteosarcomas presenting as the chondroblastic subtype (Martinez and Magliocca, 2019). Common sites for osteosarcoma in the mandible include the body and the ramus.

## 2.6. Cephalometry

Cephalometry is the study and measurement of the head (commonly the human head). Medical imaging techniques such as CT scans, MRI scans and X-rays are employed to recreate a model of the skull, from which measurements can be taken. Cephalometry is used in various fields such as ancestral tracking and biological anthropology (Darkwah et al., 2018). Cephalometric analysis refers to the clinical application of cephalometry. This clinical application consists of oral and maxillofacial surgery, both cosmetic and reconstructive.

During such a study the relationships between the dental and skeletal components of the human skull are analyzed. In the case of oral and maxillofacial surgery, the components are required for useful landmarks on the skull and the analysis refers to the positional measurement of these landmarks. These results are used prior to treatment to diagnose facial abnormalities or develop a surgical plan, during treatment to evaluate progress and post-treatment to determine whether surgical goals were reached (Predoctoral Orthodontic Laboratory Manual, 2008). Cephalometric images and measurements provide reliable presurgical and postsurgical data on soft tissue skeletal relationships (Kryger et al., 2011).

Cephalometric analyses gradually evolved to form cephalometric norms that surgeons could use as guidelines during surgery. These norms proved useful as they removed the need for the surgeon to perform a cephalometric analysis for each patient the surgeon deals with. A cephalometric analysis is conducted from a lateral image of the skull (MRI, CT, PET etc.). This is an image of the head taken perpendicular to the patient's saggital (midline) plane. The position of the head is obtained by placing

the patient upright, eyes focused on a set point straight ahead. Figure 11 shows the natural head position with important cephalometric planes used by researchers Toman et al. (2011). .

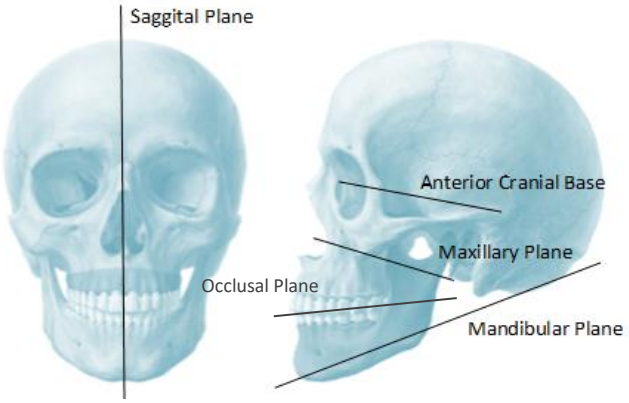


*Figure 11: Natural Head Position (Illustration: BI Giddy)*

The basic elements of an analysis are angles and distances. A cephalometric study can be categorized as follows:

- Angular – Study dealing with angular measurements of anatomical landmarks.
- Linear – Study dealing with distance measurements of anatomical landmarks.
- Coordinate – Study dealing with the Cartesian or 3-D planes (Ricketts, 1960).
- Arcial – Study dealing with the construction of arcs to develop a relation between anatomical landmarks.

These categories can further by classified by the following:

- Mononormative: Deals with arithmetic or geometrical means (Garcia, 1975).
- Multinormative: A range of norms are used while the subjects age and sex are considered.
- Correlative: Used to assess individual variations of facial structure in order to establish relationships.

### 2.6.1. Landmarks

The identification of landmarks is the most important step in the cephalometric process. These landmarks will form the basis of all measurements, norms, conclusions, and predictions. The chosen landmarks should be easily identifiable and analogous to the human skull (especially to the *Natural Head Position*). Early cephalometric analysis relied heavily on 2 – Dimensional (2D) imaging. The unreliability of early 2D cephalograms lead to inaccurate cephalograms which affected surgical outcomes. Landmark identification has become more straightforward since the introduction of more advanced imaging techniques such as *Cone-Beam Computed Tomography* (CBCT). 3 – Dimensional (3D) imaging boasts many advantages over 2D images. The introduction of a third plane reduces the risk of overlapping structures and distortion. The minute head movements of patients during scans, that could otherwise affect the analysis, are ignored as the landmarks retain spatial relationships (Ludlow et al., 2009). Gribel et al. (2011) compared the accuracy of cephalometric measurements made on lateral cephalograms vs. CBCT scans. It was discovered that due to the differences in measurement accuracy between 2D and 3D analyses, 2D cephalometric norms cannot be used for 3D

measurements. Due to the advantages of 3D scans as well as the inability to apply 2D data to 3D, 3D norms have begun to be developed. Tables 1-3 (Gillingham, 2018) and Figures 12 and 13 describe the most common landmarks on the mandible, maxilla, and other cranial regions, as identified by Proffit et al. (1986).

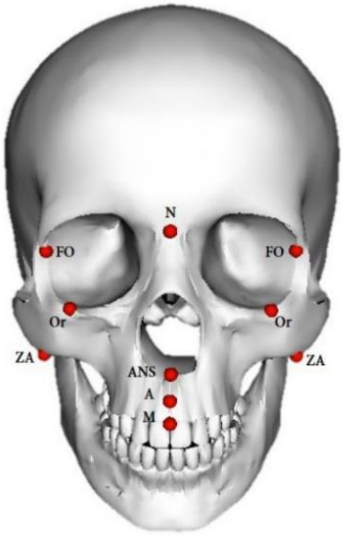


*Figure 12: Cranial and Maxillary Landmarks (Gillingham, 2018)*

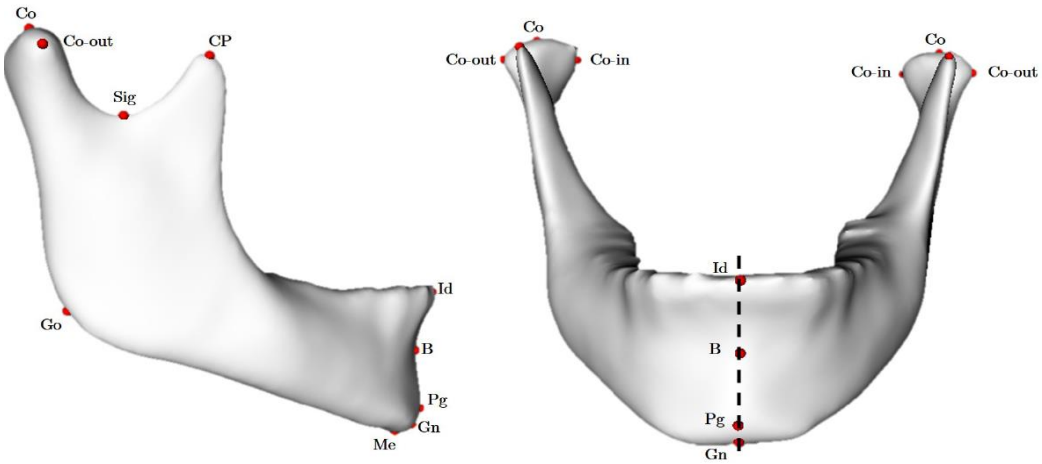


*Figure 13: Mandibular Landmarks (Gillingham, 2018)*

*Table 1: Mandibular Landmarks*

| Landmarks | Symbol | Description |
|---|---|---|
| **B Point** | B | The most posterior point between the Infradentale and pogonion on the sagittal plane |
| **Pogonion** | Pg | The most anterior point on the chin, found along the saggital plane |
| **Gnathion** | Gn | The point found midway between the menton and pogonion on the sagittal plane |
| **Menton** | Me | The most inferior point on the chin, found along the sagittal plane |
| **Gonion** | Go | The most inferior and posterior point found on the angle |
| **Sigmoid Notch** | Sig | The most inferior point found on the sigmoid notch |
| **Condylion** | Co | The most posterior point found on the condyle |
| **Lateral condyle** | Co-out | The most lateral point found on the condyle |
| **Medial condyle** | Co-in | The most medial point found on the condyle |
| **Infradentale** | Id | The highest point of the gym between the two central incisors of the lower jaw |
| **Coronoid process apex** | Cp | The most superior point found on the coronoid process |

*Table 2: Cranial Landmarks*

| Landmarks | Symbol | Description |
|---|---|---|
| **Nasion** | N | The intersection of the nasal and frontonasal suture found on the sagittal plane |
| **Sella** | S | The midpoint of the sella turcica found on the saggital plane |
| **Porion** | Po | The most superior point on the upper margin of the ear canal |
| **Orbitale** | Or | The most inferior point on the lower rim of the orbit |

| | | |
|---|---|---|
| **Frontomalare orbitale** | FO | The point on orbital rim intersecting with the frontozygomatic suture |

*Table 3: Maxillary Landmarks*

| Landmarks | Symbol | Description |
|---|---|---|
| **Anterior nasal spine** | ANS | The most anterior point on the base of the nose |
| **Posterior nasal spine** | PNS | The most posterior point on the base of the nose |
| **Zygomaxillary anteriore** | ZA | The center of the concavity of the zygomatic process of the maxilla |
| **A point** | A | The deepest point on the anterior section of the maxilla found along the sagittal plane |

## 2.7. Implant Design

Mandible implants and mandible reconstruction methods are employed to restore the function and quality of life of a patient whose mandible has been damaged via trauma or severe disease infiltration such as cancer.

### 2.7.1. Reconstruction Methods

There are many methods of mandibular reconstruction, each with their own benefit and drawbacks. The chosen method for reconstruction will depend on a multitude of factors such as the expertise of the surgeon, extent of the mandible damage, available technology etc. The following are a list of mandible reconstruction methods provided by literature from Petrova et. al (2016).

- Tissue Flap: This is a simple reconstruction technique. Flap surgery is used in plastic and reconstructive surgery where a type of tissue (in the case of mandible reconstruction, bone tissue) is lifted from a donor site and moved to the area of interest with an intact blood supply. This is different to a graft which does not have an intact blood supply. A common retrieval site for the bone is the crest of the hip, known as the iliac.
- Mandibular Bridging Plate: This is the most widely employed form of mandible reconstruction (Kumar et al., 2015). This technique involves intraoperatively bending steel, vitallium (cobalt chromium and molybdenum alloy) and titanium plates into the most suitable shape. A combination of screws and bone cement are used as a fixation mechanism. Although common, this method has high instances of short-term failure, <1 year (Mohammed, Fitzpatrick and Gibson, 2017). Failure occurs at the bending site due to the stress concentrations present. Failure is also observed at the mandible-plate integration site. The

forces induced by mandible loading place pressure on an already weakened mandible resulting in fracture.

- Cancellous Bone in Titanium Mesh: This method involves creating a titanium mesh tray into which bone is packed. The tray can be 3D printed or bent from preformed titanium mesh sheets. The tray is then fixed to the mandible and harvested bone, usually from the ilia region, is packed into the tray. Yamada et al. (2016). Two thirds of patients display excellent new bone formation while half experience post-operative complications such as mesh fracture, mesh exposure in the oral cavity and delayed infection. A *Visual Analogue Scale* (VAS), range = 1-100, was used by the authors to evaluate patient satisfaction during the follow-up period. Including the complications, the mean VAS score was 77.6. These results may indicate a method that is clinically useful.
- Vascularized Free Flap: This mandibular reconstruction method involves a vascularized composite flap which contains bone and muscle (van Zyl and Fagan, 2017). Donor sites for vascularized free flaps include the iliac crest, scapula and radial forearm. Vascularized free flaps are at a higher risk for intra- and post-operative complications (van Zyl and Fagan, 2017). Arce et al. (2012) reported a 92% success rate for vascularized free flaps on cancer patients who underwent chemotherapy and external beam radiation therapy. The authors state that the results indicate that this mandibular reconstruction method is highly predictable, results in few major complications and that chemotherapy and radiation alone do not have a statistically significant effect on flap complication rate.
- Tissue Engineered Bone Scaffold: A bone scaffold is made up of porous, biodegradable material that stimulates bone growth and provides mechanical support during bone repair. Bose, Roy and Bandyopadhyay (2012) state that the following are primary concerns when designing a bone scaffold.
    - Biocompatibility: This is described as the ability to stimulate, protect and support cellular repair without poisoning or infecting host tissue (Williams, 2008). Ideal scaffolds should not only stimulate bone growth but also form blood vessels around the implant to support nutrient, oxygen and waste transport (Olszta et al., 2007).
    - Mechanical Properties: The mechanical properties of the bone scaffold should match host bone properties. Due to the large variation in mechanical properties of bone as well as the role geometry plays in affecting this, an ideal bone scaffold is difficult to design (Olszta et al., 2007).
    - Pore Size: Pore size is essential for proper diffusion of nutrients and oxygen for cell survivability. Pore size should be at least 100 µm (Rouwkema, Rivron and van Blitterswijk, 2008). However, pore sizes that range from 200 to 350 µm are optimal for proper tissue growth (Murphy, Haugh and O'Brien, 2010)
    - Bioresorbability: Bone scaffolds need to degrade at a controlled resorption rate. This will create space for the growth of new bone tissue. Bone scaffolds will degrade at varying speeds depending on applications. Scaffolds used in spinal fusion require 9 months or more while scaffolds in cranio-maxillofacial applications require 3 to 6 months (Bose, Roy and Bandyopadhyay, 2012).

### 2.7.2. Custom Implant Design

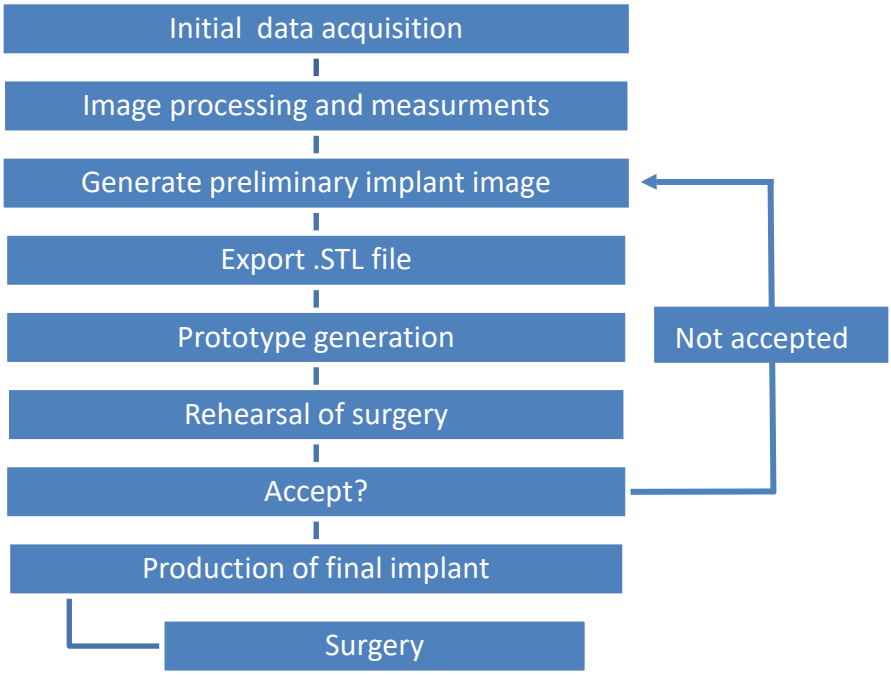


*Figure 14: Patient-Specific Design Process (Illustration: BI Giddy)*

Figure 14 shows the patient-specific design process. Customized, or patient-specific implants are implants that require extensive analysis of patient data. This data can be in the form of CT, x-ray or MRI scans and involves the measurement of the mandible dimensions. Landmark positioning, facial contours and irregularities are measured and recorded. This data is then used to create a patient-specific plate. These implants present with significantly higher success rates than Commercial Straight (CS) implant methods such as the mandibular bridging plate.

The general process for patient-specific implants is as follows: Scans of the patient's head will be taken. A 3D CAD model of the head is generated, with these scans, and measured. These measurements will then be used to create a 3D CAD model of the implant. A trial implant will be generated, and the surgeon will attempt to fit this implant to the patient's mandible. If this implant is suitable the final implant will be manufactured and placed in the patient. If this trial implant is unsuitable a new implant image will be created, and the process will continue until the surgeon is happy with the plate. The final manufactured implant will account for geometry changes much better than a CS model that has been intra-operatively shaped by the surgeon (Ortho Baltic Implants, 2020).

As, previously stated. the quality of the CS implant is dependent on the complexity of the implantation area, surgical skill and experience and the availability of technology and tools that can be used to develop bending and cutting guides that assist in the shaping of the implant. The bending of the implant causes weakness in the material, leading to high failure rates in mandible reconstruction plates. As the customized implant has not been handled or manipulated it is free of the irregularities that plastic deformation introduces, decreasing the rate and risk of failure.

### 2.7.3. Parametric Modelling

A parametric CAD model is similar to the previously mentioned custom implant in the sense that it receives patient data, and a better geometrical match is rendered. A model is parameterized by taking measurements of the desired anatomy such as a hip, shoulder or mandible and identifying landmarks that can be used to assist in the description of the shape. The landmarks and measurements would be taken from a cephalometric analysis of the mandible structure. It is up to the designer to identify important and unimportant landmarks so as best to describe and parameterize the implant model. These landmarks will form the initial input for the parametric CAD file. An approximation of the implant structure will then be generated. These models are especially powerful as they do not require the same lead time, cost and effort that are present with custom implants.

George and Kumar (2013) designed a parametric model for a hip. The authors identified features along the femur and joint such as femoral anatomical axis, head-neck shaft angle and cross section of the medullary canal. Using these features the authors were able to define the following parameters for the implant model: femoral and neck cross sections and radii, femoral head center location and radius of head sphere and lesser trochanter reference.

## 2.8. Finite Element Analysis

To the best of our knowledge there is no standardized method of modelling a mandible reconstruction plate as there are many different approaches to modelling muscle forces, force vectors and displacement boundary conditions in literature. The values, setups and procedures common in mandible FEA literature will be discussed.

### 2.8.1. Mandible Material Assignment

The material properties assigned to mandibles during FEA vary significantly across literature. Narra et al. (2014) and Vajgel et al. (2013) reported isotropic and homogenous trabecular bone with Young's Modulus = 1 500 MPa and a Poisson's ratio = 0.3. Cortical bone mechanical properties were modelled as orthotropic with Young's Modulus ($E_x$, $E_y$, $E_z$), Poisson's Ratio ($\upsilon_{xy}$, $\upsilon_{yz}$, $\upsilon_{zx}$) and Shear Modulus ($G_{xy}$, $G_{yz}$, $G_{zx}$). The mechanical properties for cortical bone are outlined by Schwartz-Dabney and Dechow (2003). Figure 15 shows the bone distribution used in the study performed by Vajgel et al., 2013).

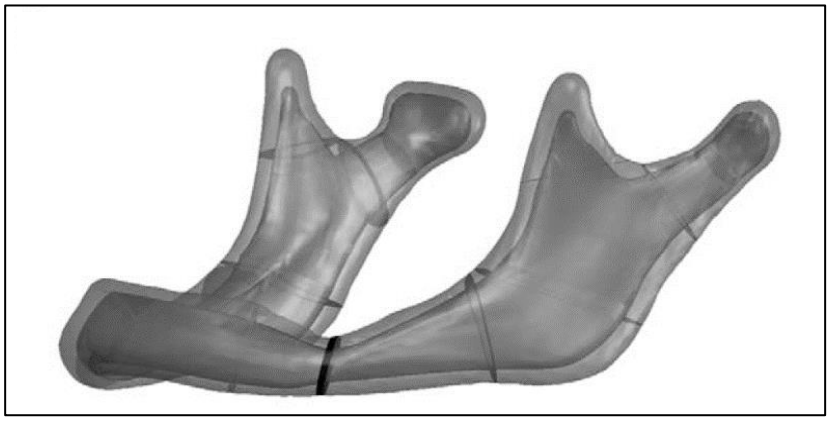

*Figure 15: Cortical and Trabecular Bone Distribution (Vajgel et al., 2013)*

Schwartz-Dabney and Dechow (2003) report that several sites in the mandible did not display consistent directions of maximum stiffness among specimens although each specimen expressed significant orthotropy. Cortical thickness varies significantly between sites and bone stiffness was reported to be 20 – 30 GPa higher in the longitudinal direction compared to the circumferential and tangential direction. The accuracy of stresses calculated varied depending on direction along which the maximum bone stiffness varied. The accuracy of mandibular stress depends on the location. Figure 16 shows the mandible sample sites.

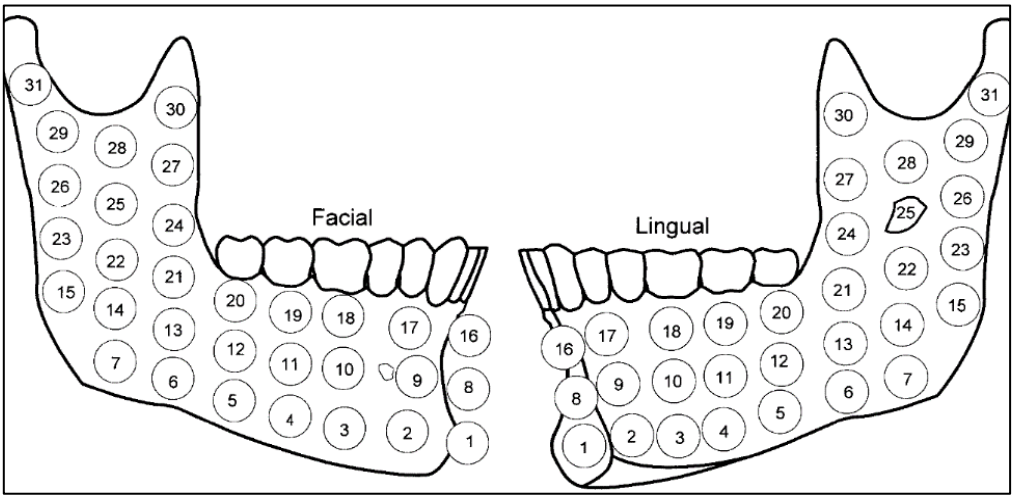


*Figure 16: Mandible Sample Sites for Material Analysis (Schwartz-Dabney and Dechow, 2003)*

Al-Ahmari et al. (2015) and El-Anwar and Mohammed (2014) modelled both the cortical and trabecular mandibular bone as homogenous and isotropic. The mechanical properties of cortical bone are given as Young's Modulus = 13 700 MPa and Poisson's Ratio = 0.3, while trabecular mechanical properties are given as Young's Modulus = 1370 MPa and Poisson's Ratio = 0.3. Knoll, Gaida and Maurer (2006) reported the same assumptions except cortical mechanical properties were a Young's Modulus = 8700 MPa, Poisson's Ratio = 0.3 and a Tensile Strength = 85 MPa. Trabecular mechanical properties were Young's Modulus = 100 MPa, Poisson's ratio = 0.3 and Tensile Strength = 13 MPa.

Arbag et al. (2013) and Gutwald, Jaeger and Lambers (2016) assumed the mandible to be homogenous and isotropic. This means that the bone material properties are constant through every plane and nonlinear stress-strain characteristics would not appear. Arbag et al. (2013), assumed a Young's Modulus = 14 000 MPa and a Poisson's ratio = 0.3. Gutwald, Jaeger and Lambers (2016), assumed a Young's Modulus = 10 000 MPa and a Poisson's ratio = 0.3.

### 2.8.2. Boundary Conditions

The boundary conditions and initial study values are one of the most important aspects of FEA. A bad choice for boundary conditions or the incorrect application of a boundary condition, will lead to solution divergence or a convergence to an incorrect solution. In mandible FEA literature the four mandible muscles are commonly used to describe the loading of the mandible during occlusion (chewing). Other weaker masticatory muscles and muscles involved in opening and translating the mandible were not represented in order to simplify calculations (Daegling and Hylander, 2000; Kimura et al., 2006; Richmond et al., 2005; Ross et al., 2005; Wong et al., 2012). To the best of our knowledge there is no standardized method of modelling a mandible reconstruction plate as there are many

different approaches to modelling muscle forces, force vectors and displacement boundary conditions in literature.

Knoll, Gaida and Maurer (2006) assumed the loading of the mandibular muscles as tension forces only. This was based on the fact that muscles transmit traction and joints transmit pressure. Horizontal muscle forces were neglected in this study as the muscle forces counterbalance each other. A bite force of 135 N was applied to the mandible at the lower incisors. Unknown muscle force values were calculated from equations of equilibrium.

El-Anwar and Mohammed (2014) applied two types of vertical loading during their FEA; firstly, a vertical force of 150 N at the lower lateral incisors and secondly, a 150 N vertical force was applied at the lower canines. Arbag, Korkmaz, Ozturk and Uyar, (2008) applied a vertical force of 62.8 N in the lower incisal region of the mandible. This value was based on a bite force study conducted by Tate GS., Ellis E. 3rd and Throckmorton G. (1994).

Wagner et al., (2002) neglected the lateral pterygoid muscle as it acts horizontally, effectively counterbalancing the left and right side of the mandible. The temporalis, masseter and medial pterygoid were still considered in the FEA with values of 329.2 N, 272 N and 174.8, respectively. Only a fraction of this muscle capacity was used based on information provided by Anderson (1956) and van Eijden (1991). Feller et al. (2003) reported similar values to Wagner et al. (2002) however, the lateral pterygoid was considered in this study. The reported values for the temporalis, masseter, medial and lateral pterygoid were 350 N, 276 N, 154 N and 130 N respectively. No information was given on muscle vectors or directions.

Al-Ahmari et al., (2015), Narra et al. (2014), Vajgel et. al (2013) and Wu, Lin, Liu and Lin (2017) resolve each force into the x, y, and z components and apply the forces over an area of attachment. Al-Ahmari et al., (2015) and Wu, Lin, Liu and Lin (2017) do not consider the lateral pterygoid. The force values and attachment sites for Al-Ahmari et al., (2015) are displayed in Figure 17 and Table 4.

Narra et al. (2014) and Vajgel et. al (2013) apply forces reported by Korioth et al. (1992). The muscle force values were calculated using the area of attachment for each muscle as well as the weight of the muscle. This was done for incisal and molar loading, respectively. The Table 5 and 6 show the values used for each simulation. Figure 18 shows the boundary conditions applied by Vajgel et al., 2013).

*Table 4: Mandible Muscle Forces (Al-Ahmari et al., 2015)*

| **Muscle Forces** | **X** | **Y** | **Z** |
|---|---|---|---|
| **Masseter** | 50 | -50 | 200 |
| **Medial Pterygoid** | 0 | -50 | 100 |
| **Temporalis** | 0 | 100 | 200 |

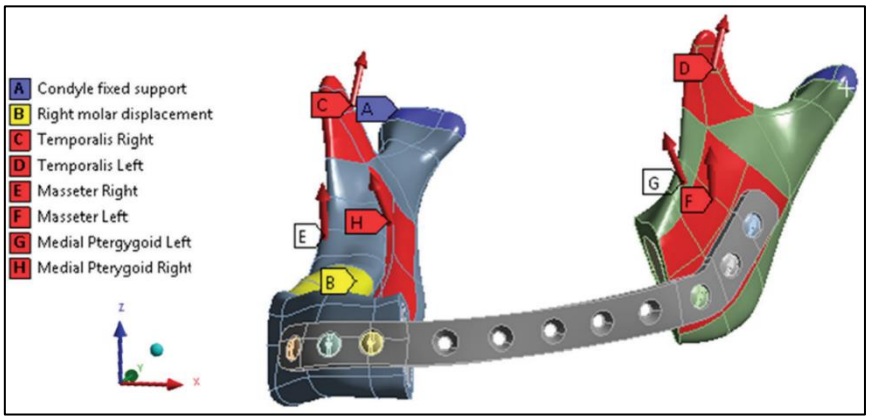


*Figure 17: FEA Boundary Conditions (Al-Ahmari et al., 2015)*

*Table 5: Incisal Loading Values (Vajgel et al., 2013)*

| | **Muscular Weight (g)** | | **Vector Components** | | |
|---|---|---|---|---|---|
| **Muscle** | Right | Left | X | Y | Z |
| **Superficial Masseter** | 22.6 | 27.1 | -0.21 | 0.42 | 0.89 |
| **Deep Masseter** | 9.7 | 11.6 | -0.55 | -0.36 | 0.76 |
| **Medial Pterygoid** | 20.7 | 29.1 | 0.49 | 0.37 | 0.79 |
| **Anterior Temporalis** | 18.1 | 22.9 | -0.15 | 0.04 | 0.99 |
| **Middle Temporalis** | 12.7 | 12.5 | -0.22 | -0.5 | 0.84 |
| **Posterior Temporalis** | 6.1 | 8.8 | -0.21 | -0.86 | 0.47 |
| **Later Pterygoid** | 8.6 | 4 | 0.63 | 0.76 | -0.17 |

*Table 6: Molar Loading Values (Vajgel et al., 2013)*

| | **Muscular Weight (g)** | | **Vector Components** | | |
|---|---|---|---|---|---|
| **Muscle** | Right | Left | X | Y | Z |
| **Superficial Masseter** | 33.3 | 33.3 | -0.21 | 0.42 | 0.89 |
| **Deep Masseter** | 9.9 | 9.9 | -0.55 | -0.36 | 0.76 |
| **Medial Pterygoid** | 60 | 60 | 0.49 | 0.37 | 0.79 |
| **Anterior Temporalis** | 5.5 | 5.5 | -0.15 | 0.04 | 0.99 |
| **Middle Temporalis** | 1.3 | 1.3 | -0.22 | -0.5 | 0.84 |
| **Posterior Temporalis** | 1.3 | 1.3 | -0.21 | -0.86 | 0.47 |
| **Later Pterygoid** | 21 | 21 | 0.63 | 0.76 | -0.17 |

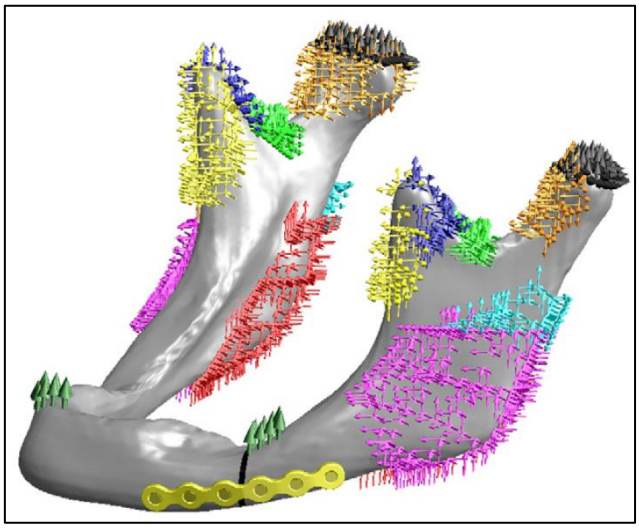

*Figure 18: FEA Boundary Conditions (Vajgel et al., 2013)*

Table 7 and Figure 19 illustrate the values and attachment sites used by the authors in this study. These force values were obtained for a lateral incisal displacement of 5 mm which causes the most displacement and tension at the condyles.

*Table 7: Mandible Boundary Condition Values (Wu, Lin, Liu and Lin, 2017)*

| **Muscle** | **Loading (N)** | | | **Reference** |
|---|---|---|---|---|
| | X | Y | Z | |
| **Deep Masseter** | 7.776 | 127.23 | 22.68 | M1, 2 |
| **Superficial Masseter** | 12.873 | 183.5 | 12.11 | M3, 4 |
| **Medial Pterygoid** | 140.38 | 237.8 | -77.3 | M5, 6 |
| **Temporalis** | 0.064 | 0.37 | -0.13 | M7, 8 |
| **Medial Temporal** | 0.97 | 5.68 | -7.44 | M9, 10 |

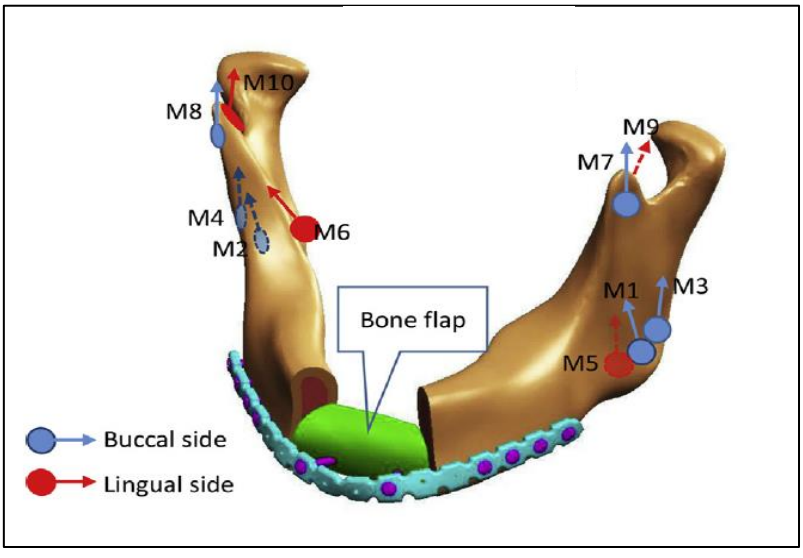


*Figure 19: Mandible Muscle Attachment Sites (Wu, Lin, Liu and Lin, 2017)*

# 3. Implant Design

The initial step in this study was to develop a CAD template of a parametric mandible reconstruction plate. Figure 20 shows the parametric MRP design process. Measurement and landmark data that was developed in a previous study (Gillingham, 2018) formed the foundation of this implant. This data was analyzed to identify the landmarks that could be used to best describe the mandible geometry. The implant was designed in Autodesk Inventor. The measurements that form the parameters of this template will plotted using points and lines in space. Where, the points represent the landmarks and the lines represent the dimensions between the landmarks. The plate profile was drawn at the left condyle point of the framework and the sketch was swept along the parametric frame. All plate components were added to the sketch. Holes for fixation to the mandible were added along the body of the plate. The holes along the ramus used a simpler technique as there was no curvature to account for. The plate corners were rounded, and fillets were applied to all the edges to protect the surrounding tissue once the plate is implanted. Finally, dimensions were adjusted to test the stability of the template.

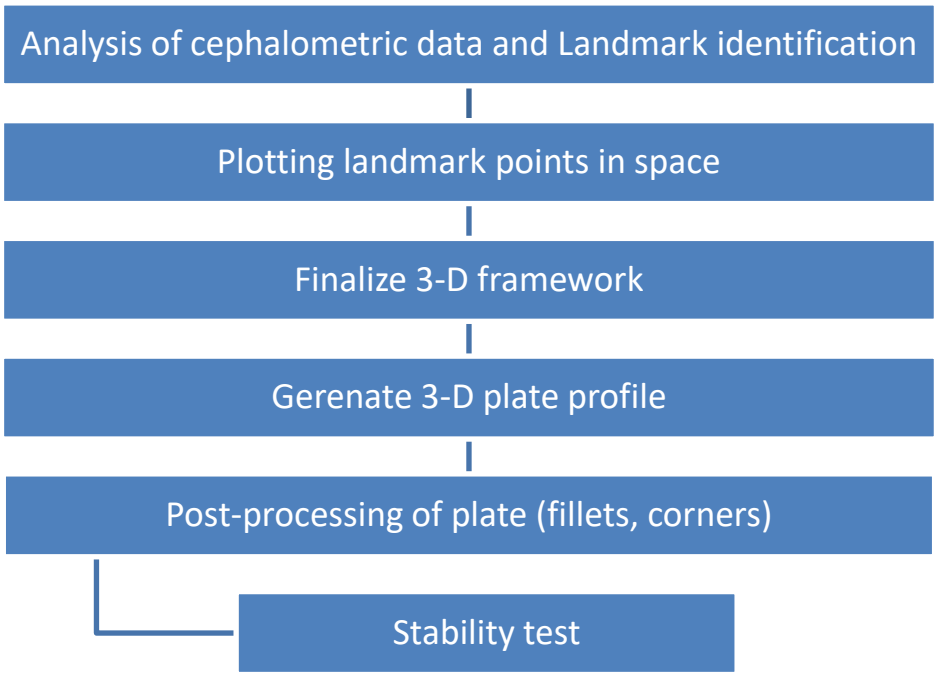


*Figure 20: Implant Design Process (Illustration: BI Giddy)*

## 3.1. Cephalometric Analysis

The first step in the implant design process was to identify the landmarks on the mandible that correspond to the region where an implant would be fixed. Figure 21 shows the typical placement for a mandible reconstruction plate. The goal in creating a parametric version is to best describe this region of the mandible.

*Figure 21: Mandible Reconstruction Plate (J&J Medical Devices, 2020)*

The landmarks used to develop the parametric implant in this study are illustrated below in Table 8 and Figure 22 . Using these landmarks, a range of parametric relationships will be established to model the shape of the reconstruction plate. The cephalometric analysis from which these landmarks were taken was conducted in a previous study. This study consisted of 40 male and 40 female scans. These samples were obtained from Tygerberg Hospital Picture Archiving and Communications System (PACS) server under ethical clearance from Stellenbosch University.

*Table 8: Parametric Plate Landmarks*

| Landmarks | Symbol | Description |
|---|---|---|
| **Condyle** | Co | The most posterior point found on the condyle |
| **Gonion** | Go | The most inferior and posterior point found on the angle |
| **Menton** | Me | The most inferior point on the chin, found along the sagittal plane |

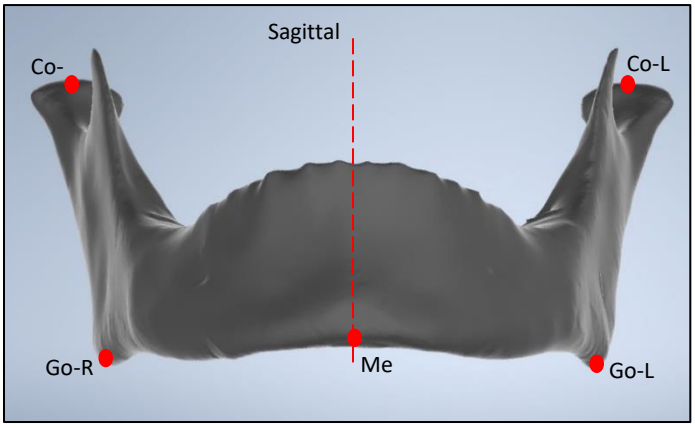


*Figure 22: Mandible Landmarks (Illustration: BI Giddy)*

## 3.2. Parametric Plate Design

The parametric plate was generated in *Autodesk Inventor Professional 2020 (*Autodesk, California, San Rafael, USA). The parameter functionality in Inventor is used to create the framework of the reconstruction plate as measurements and dimensions are saved to a parametric table. From this table the shape can be adjusted without the need to edit specific components in the component tree. The measurements in Table 9 were used as the starting point for the construction of the parametric MRP as no mandible model had yet been generated. They represent the mean mandible shape in the SSM mandible population and are in no way used as surgical guidelines.

*Table 9: Mean Cephalometric Measurements (Gillingham, 2018)*

| | **Male** | **Female** | **Units** |
|---|---|---|---|
| **Me-Co-Go-R** | 115.41 | 115.42 | ° |
| **Me-Co-Go-L** | 115.87 | 115.42 | ° |
| **Go-Sagittal-R** | 46.65 | 44.46 | mm |
| **Go-Sagittal-L** | 45.62 | 43.37 | mm |
| **Co-Sagittal-R** | 50.72 | 47.08 | mm |
| **Co-Sagittal-L** | 50.04 | 47.1 | mm |
| **Co-Go-R** | 58.52 | 54.1 | mm |
| **Co-Go-L** | 57.69 | 5308 | mm |
| **Go-Me-R** | 89.2 | 84.83 | mm |
| **Go-Me-L** | 89.44 | 84.93 | mm |

The plate was generated using a wireframe which itself was constructed in stages. Initially, in the mandibular plane, the Me landmark was plotted as well as the Go-Sagittal left and right points illustrated by Figure 23. It is important to note that Figure 23 contains only one landmark titled *Go-Me* while Table 9 contains both a left and a right measurement. The profile of the plate was created by sweeping a closed loop sketch along a trajectory selected by the designer. Two *Go-Me* points would more often than not result in, either a mismatch of the *Me* landmark or an unnaturally skew mandible as *Inventor* attempts to force a closed loop sketch for the sweep tool. Therefore, to maintain a stable CAD file and avoid unnecessary edits one *Go-Me* point is used with the average of the left and right measurements as the single point.

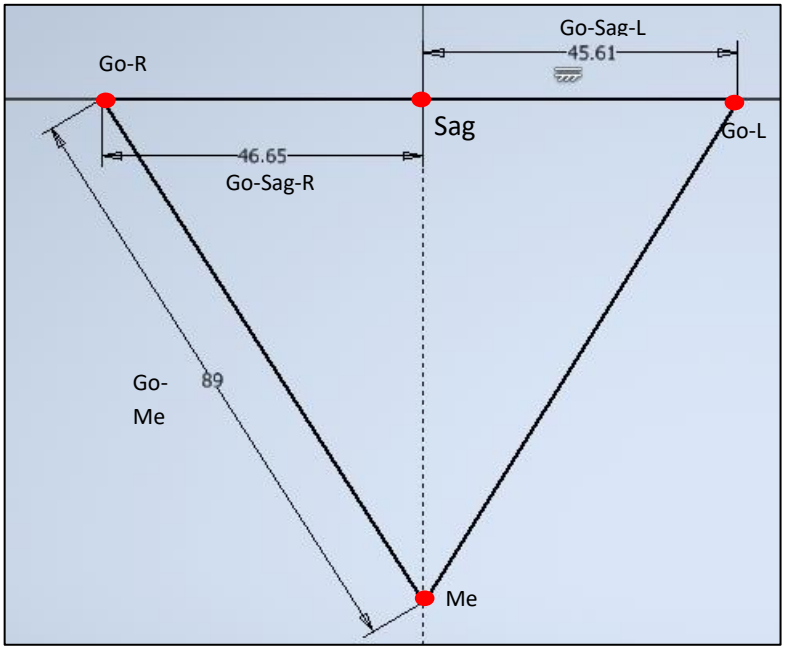


*Figure 23: 2D Parametric Skeleton (Illustration: BI Giddy)*

Next, as the mandibular condyle is not perpendicular to the occlusal plane a sagittal point is needed parallel to this plane in order to properly describe the relative positions of the condyles. The horizontal plane in Inventor was used as the occlusal plane. A simple vertical line, from the Go-L and Go-R points, was constructed. The superior point of this line was linked to the sagittal plane and the Co-Sag left and right measurements were defined. Now, the Go-Sag measurements are defined, the Co-Sag measurements are defined and the Co-Go measurements are defined. A 3D sketch was used to create the final framework of the parametric reconstruction plate. A spline was used to create the curve that passes through the Go-R, Go-Me, and Go-L points. This forms the body of the mandible. Figure 24 illustrates the final parametric framework from which the plate will be generated.

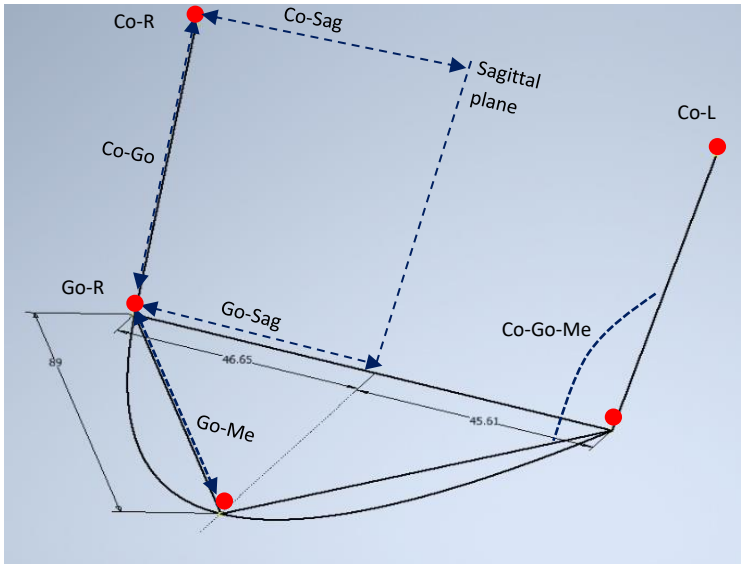


*Figure 24: Final Parametric Skeleton(Illustration: BI Giddy)*

A work plane perpendicular to the Co-Go measurement was created in order to sketch the profile of the parametric plate. The dimensions for the plate are 2.5 mm x 8 mm (Nagasao, Miyamoto, Tamaki and Kawana, 2010; Wilde et al., 2015). It is necessary to apply fillets to the edges so as to avoid damaging the tissue surrounding the plate, with emphasis on the blood vessels and nerves. A fillet radius of 0.5 mm was chosen and applied to the sketch. A sweep was performed on the sketch and the preliminary mandible reconstruction plate was generated. The plate dimensions and preliminary plate model are illustrated by Figure 25.

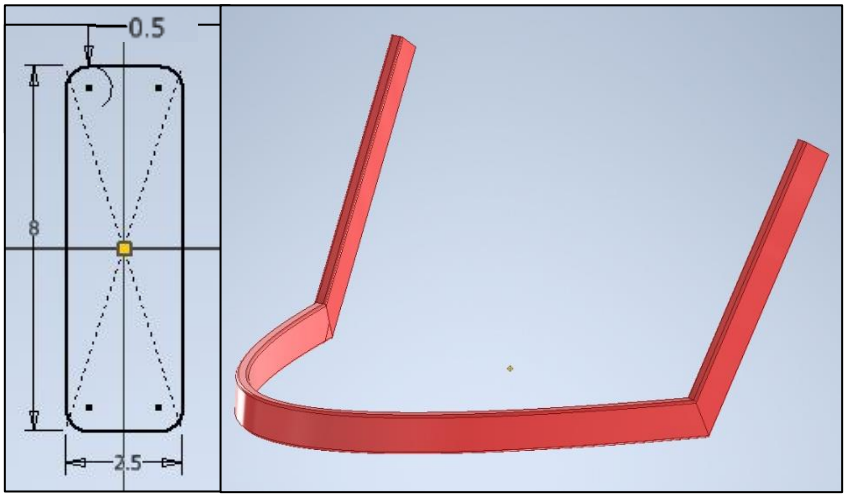


*Figure 25: Preliminary Parametric Plate (Illustration: BI Giddy)*

To finalize the parametric plate the fixation points or “screw-holes” need to be created, fillets need to be applied to the ends of the plate as well as the inner and outer segments of the angle, once again to protect surrounding tissue. The lines which would be used to define the points, show in Figure 26, were equally spaced to allow 13 total holes to be created. The angles are arbitrary and can be adjusted as needed. Using these lines, a point and sketch plane were created on the surface of the mandible reconstruction plate. Onto each plane a hole of 4 mm diameter was sketched and extruded. Figure 27 shows the respective points, planes, and sketches for the holes on the reconstruction plate. The maximum number of holes on the body region of the reconstruction plate are fixed due to the difficulty in generating each one, however, the positioning of each can be adjusted via the sketch or parameter tab and each one can be removed by suppression should the designer require different plate setups.

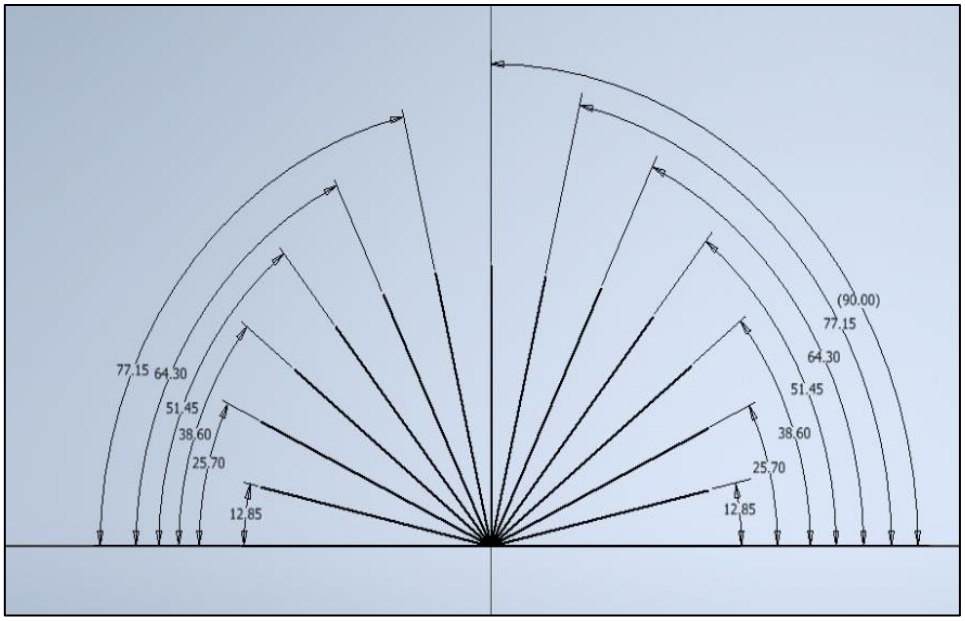


*Figure 26: Hole Spacing Illustration: BI Giddy)*

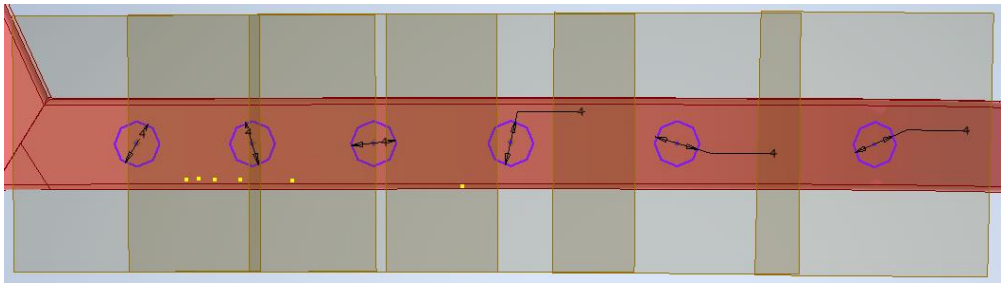

*Figure 27: Construction Planes (Illustration: BI Giddy)*

The holes on the ramus portion of the parametric plate were simpler as there was no curvature to account for. A pilot hole was created 6 mm from the edge of the plate. A rectangular pattern was created from this. The number and spacing of this pattern is manually adjusted via the parameter tab or by editing the pattern on the component tree. Figure 28 show the rectangular pattern and the plate.

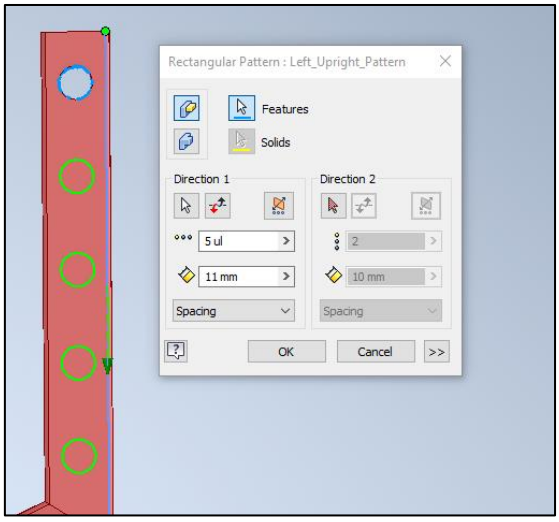


*Figure 28: Rectangular Pattern (Illustration: BI Giddy)*

The final step in the design of the parametric reconstruction plate was to add any remaining fillets and round the edges of the plate at the condylar process. Inventor updates the component tree from top to bottom therefore, it is best to add the fillets at the end as any extrusions or sketches that the fillets are related to produce errors as the dimensions are altered. Figure 29 shows the final parametric reconstruction plate.

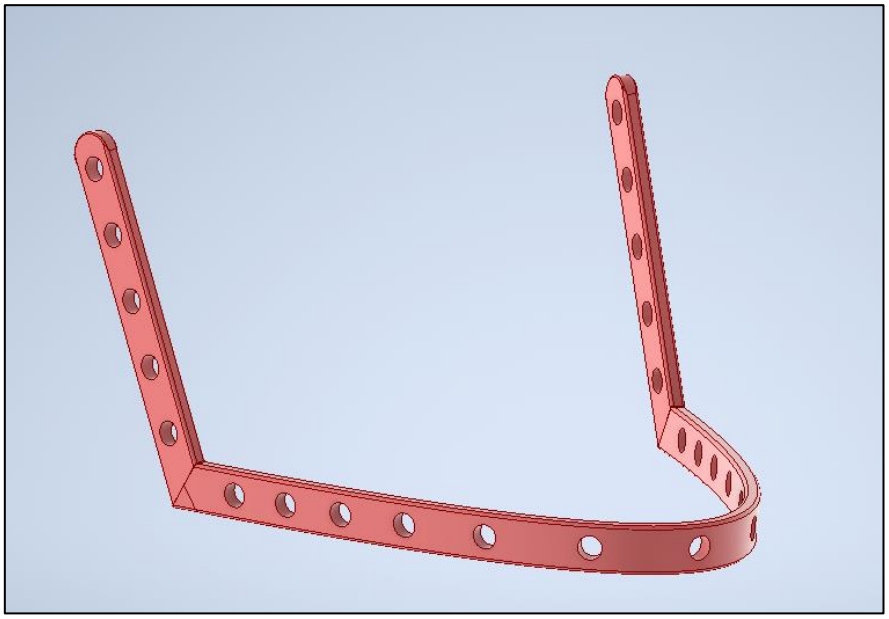

*Figure 29: Final Parametric Mandible Reconstruction Plate (Illustration: BI Giddy)*

# 4. Comparison Test

A comparison test was performed in order to determine how well the parametric reconstruction plate fits to a population of mandibles. Several male and female mandibles were generated and measured using a Statistical Shape Model developed in a previous study. The corresponding parametric mandible reconstruction plates were generated, and the models aligned in MeshLab (ISTI - CNR, Italy, Pisa). The process was separated into two steps. The initial comparison test, this was where the fit was analyzed, and dimensions were checked. Often the initial measurements did not account for various mandible irregularities that were present. Adjustments of the dimensions were necessary. When the initial fit was complete the adjusted parametric plate was divided into the respective plate configurations. Namely, the hemimandible, symphyseal and lateral short plate. Finally, the distances were calculated and recorded. Figure 30 shows the comparison process.

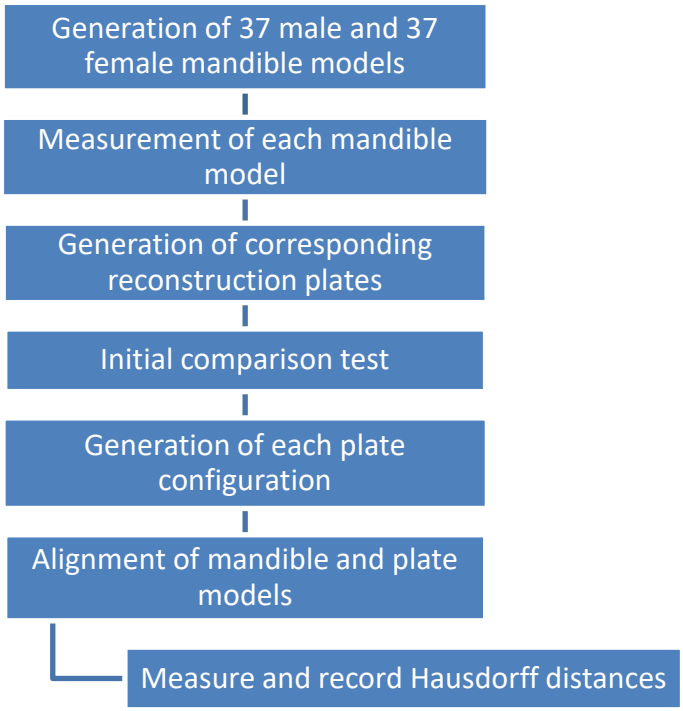


*Figure 30: Comparison Test Process (Illustration: BI Giddy)*

## 4.1. Ethical Clearance and Sample Size

The Statical Shape Model (SSM), from which all comparison information stems from, was generated using patient data collected from Tygerberg Hospital. Therefore, in order to conduct the comparison test ethical clearance was required. After receiving ethical clearance (Reference: S20/04/105), the SSM could be handled to generate the mandible population used in this study. All mandibles were randomly generated via the random function in ScalismoLab (University of Basel, Basel, Switzerland) and no effort was made to reconstruct the initial population, thereby preserving patient confidentiality.

The variables used in the calculation are as follows: Confidence Level = 95% (± 2σ), Confidence Interval = 5% and the Population Size = 40 (male and female, total = 80). Gillingham, 2018 performed a sample size calculation. This initial population of 40 male and 40 female mandibles were used to create the

SSM which represents a specific population group. The sample size of 37 male and 37 female mandibles was calculated using a sample size calculator (Surveysystem.com, 2012). Equation 1 and 2 below describe the sample size calculator method.

$$ss = \frac{Z^2 \times p \times (1-p)}{c^2} \quad (1)$$

In Equation 1, Z is the confidence level (Z-Value), p is the percentage choice (50%) and c is the confidence interval. Equation 2 represents the sample size correction formula for a finite population because the initial SSMs were generated using 40 male and 40 female mandibles. This value was used as the "population", which is the variable *pop* in Equation 2.

$$new\ ss = \frac{ss}{1+\frac{ss-1}{pop}} \quad (2)$$

## 4.2. Statistical Shape Model

There are two types of training shapes: anatomical shapes and arbitrary shapes. Arbitrary shapes are defined as the geometrical information that remains when *location*, *scale*, and *rotational* effects are filtered out, while an anatomical shape is defined as the geometrical information that remains when only *location* and *rotational* effects are filtered out. This is because in biology size and shape are often correlated. A simple example of the SSM process is as follows. Choose an arbitrary 2D shape such as a hand. Assume the shape can be characterized by length "*l*" and width "*s*". The point of the resulting SSM will be to model how these measurements vary within the family of hand shapes. It is assumed that the shape distribution can be modelled using a normal distribution. This assumption implies that it is sensible to think of a mean hand shape. It is equally likely for hands to be smaller or larger than this mean shape and it is unlikely to ever observe shapes that are much larger or smaller than the mean. Figure 31 shows an example of the SSM generation process.

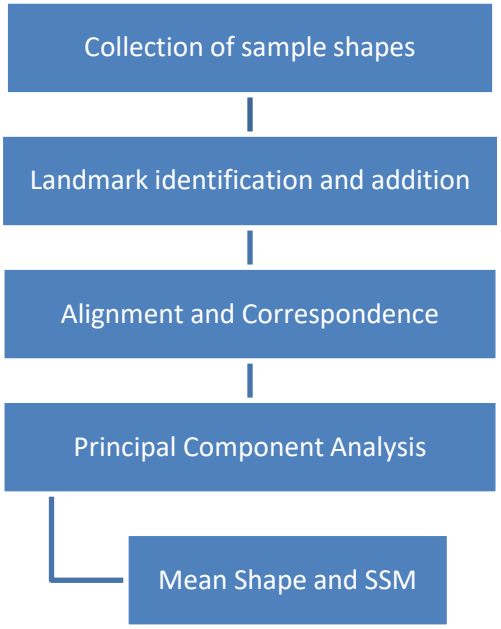


*Figure 31: SSM Generation Process (Illustration: BI Giddy)*

Any shape can be represented as a collection of data points (Cootes, Baldock and Graham, 2000). SSMs represent an average shape of many 3D objects as well as the variations that this shape can take. Correspondence mapping is required to build a shape model. This means that for every point on shape A the same point needs to be discoverable on shapes B-Z. If the correspondence between the models is established, then the variations between the shapes can be investigated. If a training set of shapes (population group) are aligned according to the same frame of reference (target shape) and are superimposed a distribution of the points making up that particular shape can be observed. Landmark points are identified, and some form of registration is performed. This involves identifying correspondence between the training data and transforming the shapes into a single coordinate system.

A common correspondence method is Procrustes Analysis. This method analyzes the distribution of a set of shapes. An arbitrary shape is chosen, and the remaining shapes are aligned via scaling, rotation or translation resulting in the shapes superimposed on one another. This is to minimize the distance known as the Procrustes distance between the point clouds that govern the shapes. Once the correspondence between the training data has been established Principal Component Analysis (PCA) is performed. PCA uses orthogonal transformations to convert the correlated values of the aligned shapes into linearly uncorrelated variables called principal components. The principal components are also known as modes. The major or first principal component accounts for the largest possible variance in the shapes. Each succeeding principal component in turn accounts for the largest possible variance in the shapes with the constraint being that it is orthogonal to the preceding component. Finally, the SSM is represented as a mean point distribution model combined with these principal modes of variation.

## 4.3. ScalismoLab Randomization

The randomization function in ScalismoLab makes use of a standard multivariate Gaussian distribution. The multivariate distribution is useful in extending the Central Limit Theorem to multiple variables. The arithmetic mean and standard deviations of a sufficiently large, random sample group are computed. The Central Limit Theorem states that the distribution of this sample group will be normally distributed. This statement is true irrespective of the original data, provided that the sample population is sufficiently large. Usually n ≥ 30 (Central Limit Theorem, 2020).

Equation 3 governs the randomization function in ScalismoLab.

$$R = BM \times (\sigma \times c) + \mu \tag{3}$$

The *Base Matrix* (variable BM) is the normalized matrix of the SSM, $\sigma$ is the standard deviation, $c$ is the coefficient drawn from the standard multivariate Gaussian distribution data and $\mu$ is the mean vector. *BM*, $\sigma$ and $\mu$ are information that is stored in ScalismoLab during the generation of the shape model. The shape model samples random models by changing the variable $c$ according to the Gaussian distribution. Currently, ScalismoLab does not allow the manual adjustment of variable $c$, meaning randomization in ScalismoLab is an automated process and cannot be directly controlled.

## 4.4. Model Generation

All mandibles were generated in ScalismoLab. Figure 32 shows the ScalismoLab interface. On the bottom left corner (red border) there is a tab labeled shape parameters. This SSM contains 39 principle components. Each slider can be adjusted manually but never to directly replicate mandible dimensions, as the principle components work with directions. The component sliders are not governed by the Central Limit Theorem, therefore, there is no guarantee that these samples will form a normal distribution, or that the samples are part of the same family of shapes. With this knowledge the models were randomly sampled from the SSM itself.

On the top left of Figure 32 (blue border) are the landmarks. These can be manually selected on the mandible, or the landmarks can be imported from a file. The latter method was used in this model as the method of manually adding the landmarks each time is subject to small deviations which, when running multiple models begins to introduce measurement errors that can complicate the alignment process. The landmarks are initially selected, and the software records the vertex indices. Then, when the model is randomly sampled, the new coordinates of the vertexes are recorded, and the landmarks are updated. In order to validate whether the randomly generated mandible models belong to the population group represented by the SSM a Bland and Altman analysis was performed. The green anatomical landmarks were measured for the purpose of the Bland and Altman plots and the red parametric reconstruction plate landmarks were measured for the construction of the corresponding reconstruction plates.

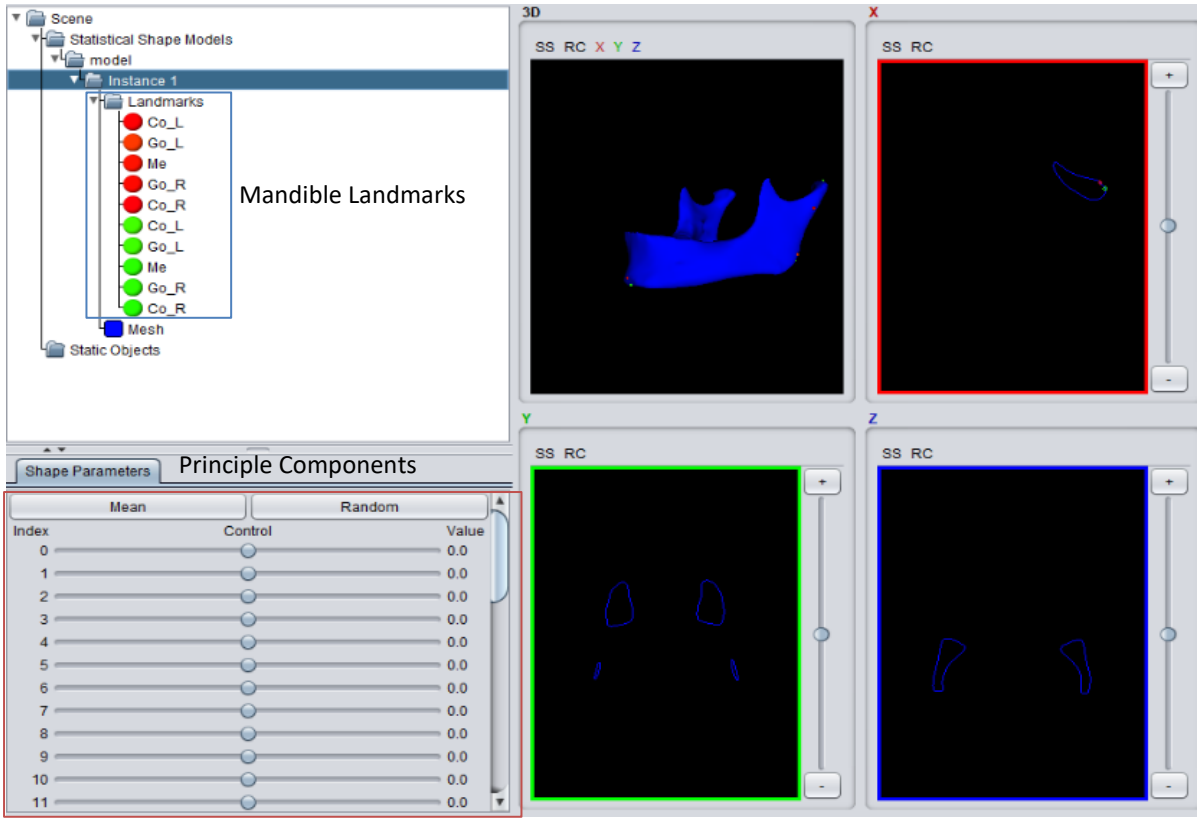


*Figure 32: ScalismoLab SSM Interface (Illustration: BI Giddy)*

Each landmark consists of an x, y and z coordinate that can be accessed by clicking on the landmark and opening the positioning tab. These coordinates were recorded and serve as the input to a MATLAB (MathWorks, Natick, Massachusetts, USA) script that outputs the various mandible measurements. The mandible measurements can be seen in Appendix A. The parametric landmarks were labelled the same for simplicity however, these landmarks were shifted to the locations where a mandible reconstruction plate would be placed. Table 10 provides a short description of the parametric measurements. Figure 33 shows the reconstruction plate landmarks on the mean mandible. The mandibles were saved as .STL files.

*Table 10: Mandible Landmark Description*

| **Abbreviation** | **Description** |
|---|---|
| **Angular Measurement** | |
| **Me-Co-Go-R** | Right angle. Measured between the Menton, Right Condyle and Right Gonion |
| **Me-Co-Go-L** | Left angle. Measured between the Menton, Left Condyle and Left Gonion |
| **Linear Measurement** | |
| **Go-Sagittal-R** | Measured between the Right Gonion and the Sagittal Plane |
| **Go-Sagittal-L** | Measured between the Left Gonion and the Sagittal Plane |
| **Co-Sagittal-R** | Measured between the Right Condyle and the Sagittal Plane |
| **Co-Sagittal-L** | Measured between the Left Condyle and the Sagittal Plane |
| **Co-Go-R** | Measured between the Right Condyle and the Right Gonion |
| **Co-Go-L** | Measured between the Left Condyle and the Left Gonion |
| **Go-Me** | Measured between the Gonion and the Menton |

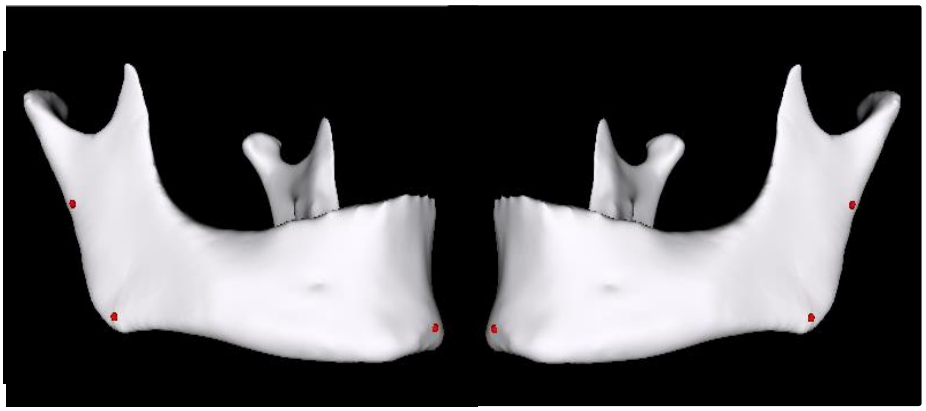

*Figure 33: Parametric Reconstruction Plate Landmarks (Illustration: BI Giddy)*

Comparison Test

Before the parametric plates were constructed it was important to determine whether the sampled mandibles were a correct representation of the SSM population. The Bland Altman (B&A) plot analysis is an effective way to evaluate bias between two measurements and also to estimate an agreement interval (Giavarina, 2015). The B&A plot is also useful to determine whether the sampling procedure in *ScalismoLab* is accurate. The B&A plot is used to quantify agreement between two quantitative measurements by constructing limits of agreement. These limits are constructed using the mean and standard deviation (σ) of the measurements. The resulting scatter plot has the difference between two paired measurements ,(A-B), on the y axis and the average of the measurements, ((A+B)/2), on the x axis. B&A recommend that 95% of the data lies within ± 2 standard deviations of the mean difference.

A modified B&A plot was proposed for this study as there was only one set of landmark measurements to plot. The mean and standard deviation from the original study, for each mandible measurement, were plotted against the data measured from the new set of mandibles. Figure 34 shows an example of a B&A plot. The measured data points (blue), ±2 standard deviations (green and purple, respectively), and the mean (red). It is clear most of the data is centered around the mean with the 28$^{th}$ data point slightly outside the boundary. This is acceptable as 95% of 37 measurements leaves 2 possible outliers. The remaining B&A plots can be seen in Appendix B.

The parametric measurements obtained from MATLAB were used to create the corresponding 37 male and 37 female reconstruction plates in *Autodesk Inventor*. The reconstruction plates were exported from *Autodesk Inventor* as .STL files.

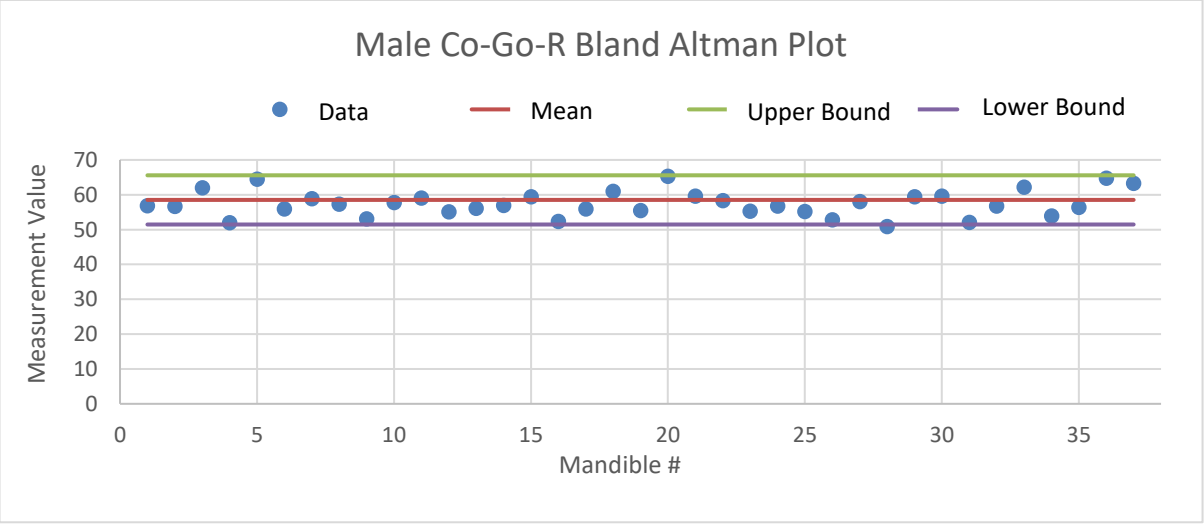


*Figure 34: Male Co-Go-R Bland Altman Plot (Illustration: BI Giddy)*

## 4.5. Comparison Test

As previously stated, the quality of the implant fit is affected by the surgeon's experience, mandible geometry, defect length, bone structure and bone strength. A comparison or fit test between the mandible models and their corresponding reconstruction plates was performed in order to mathematically measure this fit.

### 4.5.1. Hausdorff Distance

The Hausdorff distance is the measure of how far two subsets of a metric space are from each other. When comparing two meshes such as the mandible reconstruction plate and the mandible itself, the Hausdorff distance is the greatest distance from one point on data set A to the closest point on data set B. The Hausdorff distance is shown in Equation 4.

$$h\,(A,B) = \underset{a \in A}{\boldsymbol{max}} \{ \underset{b \in B}{\boldsymbol{max}} \{ \; d(a,b) \; \} \} \tag{4}$$

In Equation 4, a and b are points on set A and B respectively, and d(a, b) is any metric between these points. However, this Hausdorff distance equation format measures the distance *from* A *to* B. Equation 4 would be used when the user is working with 2- or 3-D points in space. If the data sets A and B now contain lines or various shapes such as circles, squares or in the case of this study a mandible and reconstruction plate, Equation 4 cannot be applied as there are an infinite number of points that can be used to describe the data.

The more general form of the Hausdorff distance is used to describe this situation, shown in Equation 5.

$$H\,(A,B) = max\,\{\,h\,(A,B), h\,(B,A)\} \tag{5}$$

This is sometimes referred to as the forward and backward Hausdorff distance of the sets A and B. H(A, B) now applies to all defining points in the respective data sets and not to the vertices of the shapes or a finite number of points. As per Equation 5 it is clear that the measurement from A to B will not be the same as from B to A. The sampled and target meshes need to be carefully selected and kept constant throughout the comparison test as the incorrect mesh selection will produce inaccurate results. If one considers the mandible model as the sampled mesh and the parametric reconstruction plate as the target mesh the Hausdorff distance filter will sample a certain number of points on the mandible and the distance between these points and the closest point on the parametric reconstruction plate will be measured, due to the size difference the maximum, minimum, average and root-mean-square (RMS) values will be grossly inflated. Therefore, the parametric mandible reconstruction plate was set as the Sampled Mesh and the mandible model was set as the Target Mesh. This setup will sample points on the plate mesh, search for and measure the nearest point on the mandible mesh but only in the region where the plate and the mandible coincide, not across the entire mandible. Figure 35 shows the sampled points.

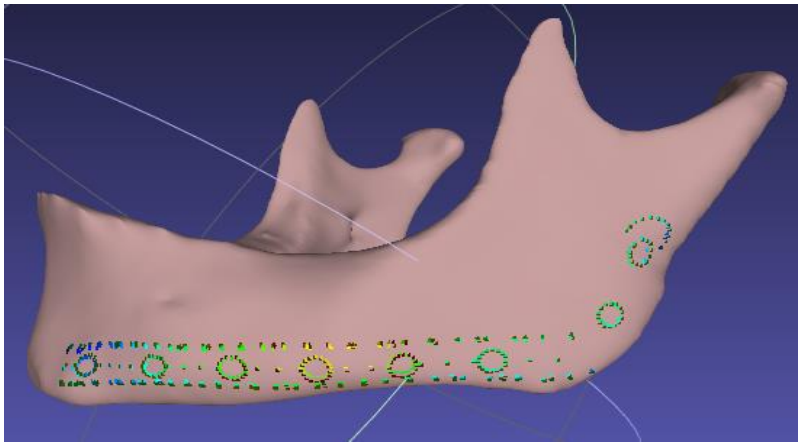

*Figure 35: Sampled Points (Illustration: BI Giddy)*

### 4.5.2. Initial Comparison

An initial comparison of the mandible and reconstruction plate was performed. This test was used to analyze the fit of the plate as often the measurements did not account for protrusions and on the mandible, particularly around the molar region. During this test it was discovered that the full parametric plate did not fit the mandible because of the protrusions mentioned. However, once the plate configurations had been generated the dimensions could easily be adjusted and the fit was improved. Figure 36 shows an example of the initial comparison test. From the image it is clear that there is significant interference between the molar and lateral incisor region on the mandible.

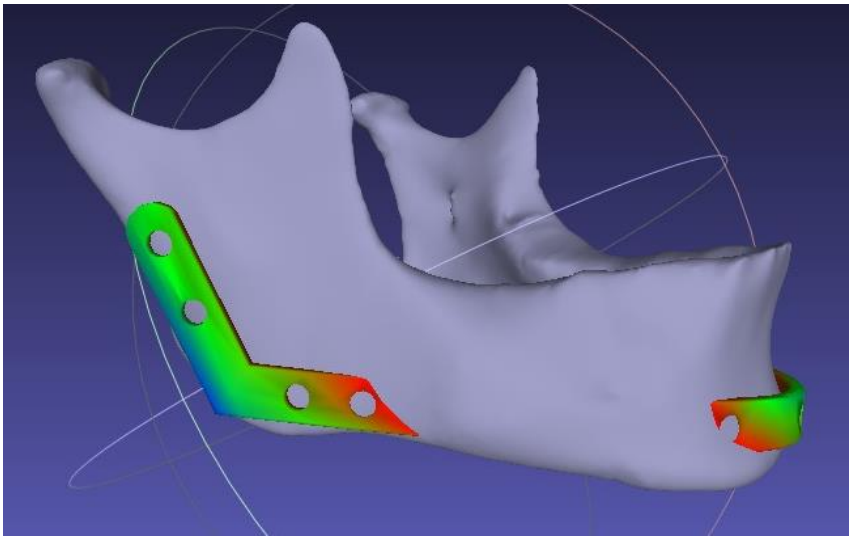

*Figure 36: Initial Comparison Test (Illustration: BI Giddy)*

After several literature sources were examined, three common plate configurations appeared. The hemimandible plate, a half plate that extends from the Me landmark to just below the mandibular condyle. The symphyseal plate, a plate extends from the left canine to the right canine. Finally, the lateral short plate, this plate length can vary but is usually used for smaller defects, resections or fractures on the body of the mandible between the molar and the canine. With this information it was

decided that the reconstruction plate will be split into each of these configurations with a comparison test performed on each.

As the initial comparison test had been performed the dimensions were edited to improve the fit and the respective plate configurations were generated in the CAD template. The mandible models and plates were imported into MeshLab. The alignment was performed using point-based glueing. The mandible mesh was fixed in space, the alignment points were selected, and the alignment was performed. Distinction should be made between the *reconstruction landmarks* and *alignment points*. The reconstruction landmarks are the landmarks on the mandible that were measured to define the plate landmarks in space and relate these points to each other.

The alignment points are corresponding landmarks on the mandible and plate that the user selects for the alignment process that MeshLab will use to perform the alignment. These alignment landmarks can be the same as the reconstruction landmarks or arbitrary points on the respective models. The alignment landmarks will vary as the plate configurations change. Once the Hausdorff distances were measured a color filter was applied to the plate as a visual description of the distance. Blue is approximately 2 mm or more, green is a fit of between 0 and 2 mm and red indicates interference. It should be noted that none of the plates were edited (fillets, rounding of corners or adjustment of the holes) as these edits protect the surrounding tissue and assist in fixation to the bone, they do not affect the comparison results.

### 4.5.3. Lateral Short Plate Comparison

The male and female plates were approximately 45 mm long and 38 mm long, respectively. This is due to the size difference between the male and female mandibles. Lateral short plates are generally used for short resections and mandible fractures. Their location will vary depending on the resection or fracture site. In order to keep the comparison tests consistent, the lateral short plates were aligned between the canine and 2nd molar. Figure 37 shows the comparison process.

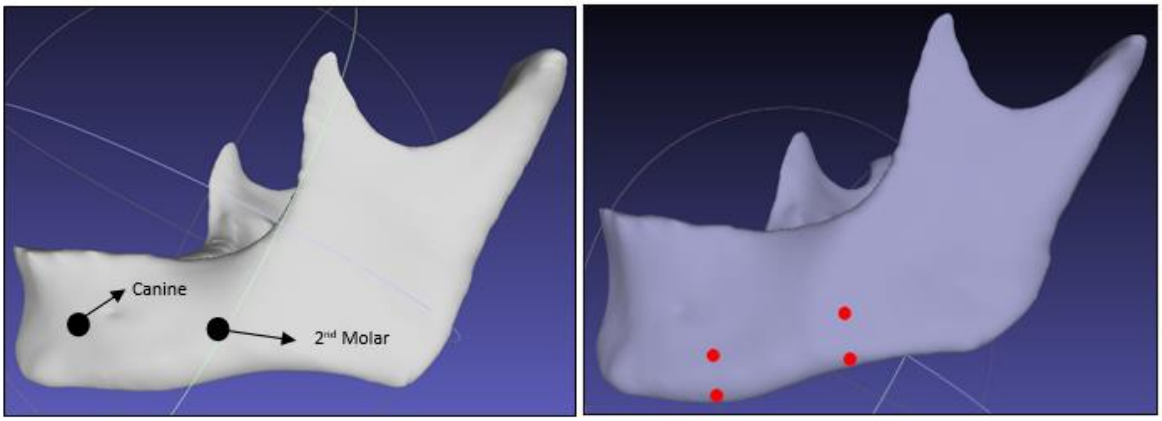


*a) Alignment Landmarks* *b) Mandible Alignment Points*

*c) Plate Alignment Points*

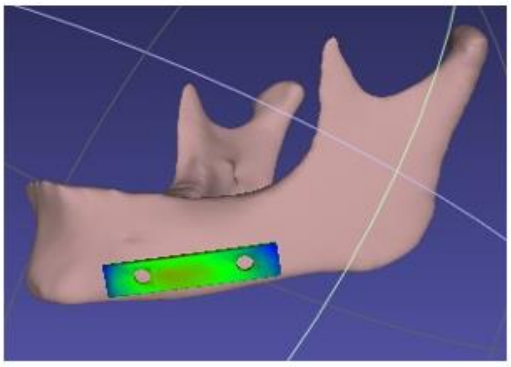

*d) Final Alignment*

*Figure 37: Lateral Short Plate Comparison Process (Illustration: BI Giddy)*

### 4.5.4. Symphyseal Plate Comparison

Figure 38 shows the symphyseal plate comparison process. The male and female plates were, on average, 72 mm, and 62 mm long, respectively. The symphyseal plates extend between the mandibular foramen on the left and right side of the mandible. The symphyseal plate, like the lateral short plate, varies in literature as the overall length will be affected by the size of the mandible resection and the number of holes required for proper fixation.

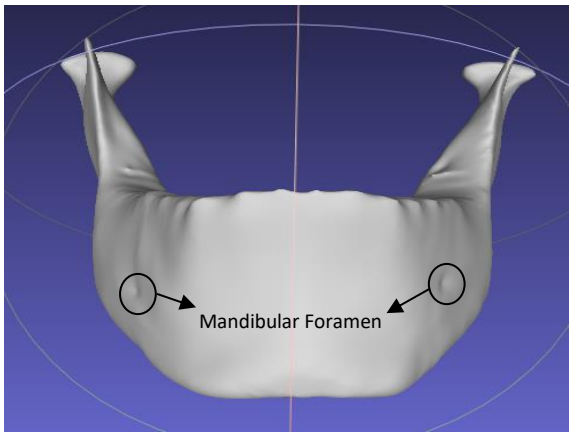


*a) Alignment Landmarks*

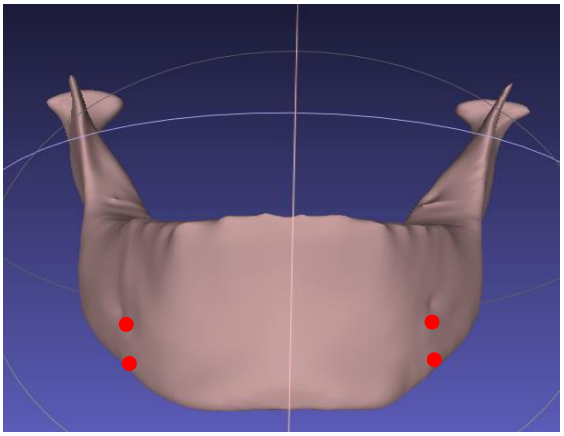

*b) Mandible Alignment Points*

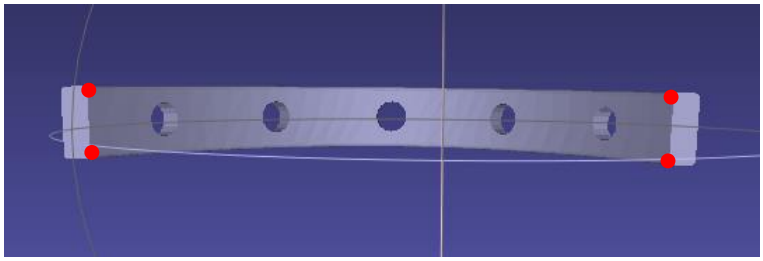

*c) Plate Alignment Points*

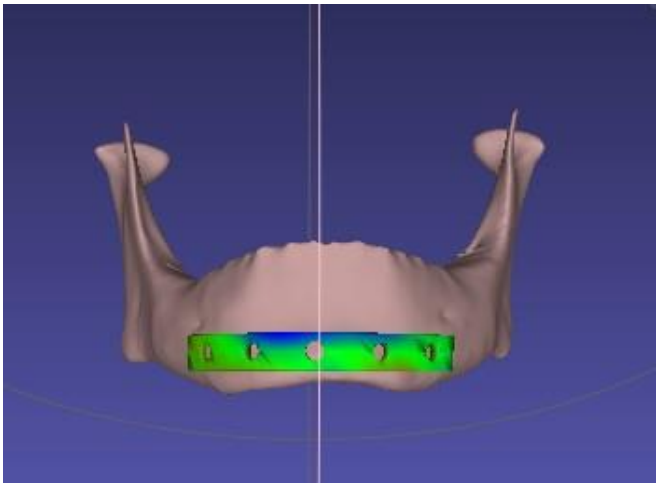

*d) Final Alignment*

*Figure 38: Symphyseal Plate Comparison Process (Illustration: BI Giddy)*

### 4.5.5. Hemimandible Plate Comparison

Figure 39 shows the hemimandible plate comparison process. The curvature length of the male and female plates were, on average, 80 mm, and 66 mm long, respectively. The ramus portion of the male and female plates varied greatly due to the different Co-Go measurements but were, on average, 30 mm, and 26 mm long for the male and female plates, respectively. The overall length varies in literature, in some cases the plate extends up to the mandibular foramen, in others up to the Me landmark and in others it may extend further. The hemimandible plates in this comparison test extend from the Me landmark to below the mandibular Condyle.

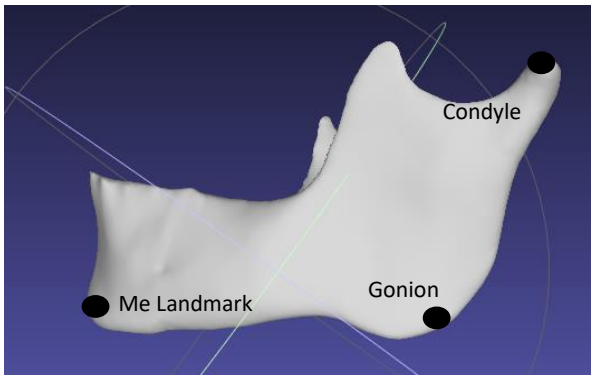


*a) Alignment Landmarks*

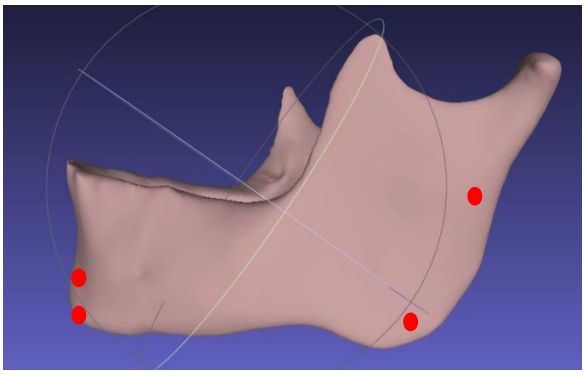

*b) Mandible Alignment Points*

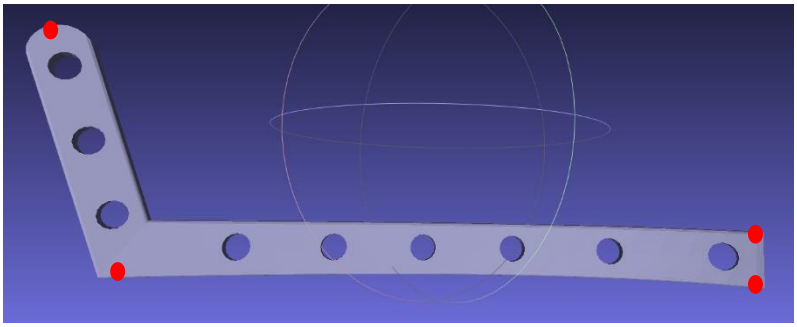

*c) Plate Alignment Points*

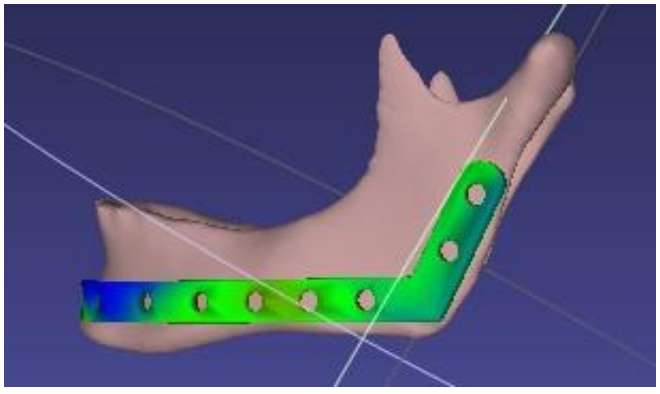

*d) Final Alignment*

*Figure 39: Hemimandible Plate Comparison Process (Illustration: BI Giddy)*

### 4.5.6. Results

The following section offers the Hausdorff distance values obtained from the comparison test of the male/female mandibles with the respective plate configurations. The measurement tables can be found in Appendix B. Tables 11, 12 and 13 list the average Hausdorff distances for the respective plate configurations.

*Table 11: Lateral Short Comparison Results*

| | **M Short** | **Fe Short** |
|---|---|---|
| **Minimum** | 0.027 | 0.008 |
| **Maximum** | 4.628 | 4.06 |
| **Mean ± σ** | 1.824 ± 0.3 | 1.661 ± 0.225 |
| **Root Mean Square** | 2.160 | 2.023 |

*Table 12: Symphyseal Comparison Results*

| | **M Symph** | **Fe Symph** |
|---|---|---|
| **Minimum** | 0.003 | 0.003 |
| **Maximum** | 4.701 | 4.233 |
| **Mean ± σ** | 1.951 ± 0.312 | 1.951 ± 0.265 |
| **Root Mean Square** | 2.309 | 2.164 |

*Table 13: Hemimandible Comparison Results*

| | **M Hemi** | **Fe Hemi** |
|---|---|---|
| **Minimum** | 0.03 | 0.012 |
| **Maximum** | 6.496 | 5.784 |
| **Mean ± σ** | 2.554 ± 0.34 | 2.357 ± 0.42 |
| **Root Mean Square** | 3.069 | 2.739 |

## 4.6. Discussion

The generic or commercial straight reconstruction plate begins as a straight piece of titanium. There is no guarantee that the CS plate will fit, and as stated in the Chapter 1 the failure rates of these plates are relatively high. From the Hausdorff distance data it is clear that each parametric plate configuration provides a good approximation. It should be noted that there was some minor interference between parts. As regions on the mandible would be missing during surgical reconstruction, due to resection, and surgeons would simply adjust the plate to account for any interference it was deemed inconsequential for the purpose of the comparison test. It is beneficial to analyze the RMS values. The maximum mean value is 2.554 ± 0.34 mm, found on the male hemimandible plate, and the minimum mean value is 1.661 ± 0.225 mm, found of the female lateral short plate. Schepers et al. (2015) indicate a mean deviation of 3.3 ± 1.3 mm. The authors analyzed the accuracy of patient-specific CAD implants. Yang et al. (2018) indicate a mean deviation of 1.4 ± 0.63 mm. The authors analyzed the accuracy of 10 reconstructive procedures using 3d printed patient-specific plates. It is clear that the comparison test values for the parametric design method are within those reported by literature.

These measurement results are preliminary and physical tests are advised to determine any difficulties associated with shaping the parametric reconstruction plates. Katsuragi et al., 2010 made use of calcium-sulphate (Plaster of Paris) 3D mandible models to shape the reconstruction plates. These mandible models were created from CT scans and served as initial bending and shaping guides for the surgeon. Future work could include physical testing using similar models. As 3D printing titanium is time consuming and expensive, a cost-efficient alternative may be to make use of Poly Lactic Acid (PLA) reconstruction plates. This a low cost, common 3D printing material that can be used as an initial alignment test before comparison tests involving titanium plates and mandibles cadavers are performed.

The mandible is especially thick between the angle and second premolar. Oversizing of the reconstruction plate is advised. This will increase the amount of bending required which is not optimal. Another solution would be to improve the Go-Me measurement. If a landmark is placed on the sagittal plane and a measurement was taken from the Me landmark this could create a reconstruction plate that, not only accounts for the protruded region but maintains the curvature approximation of the mandible. Another potentially new landmark could make use of the mandibular foramen to improve the plate fit. Figure 40 illustrates the proposed landmark as well as the protruded regions, circled in red.

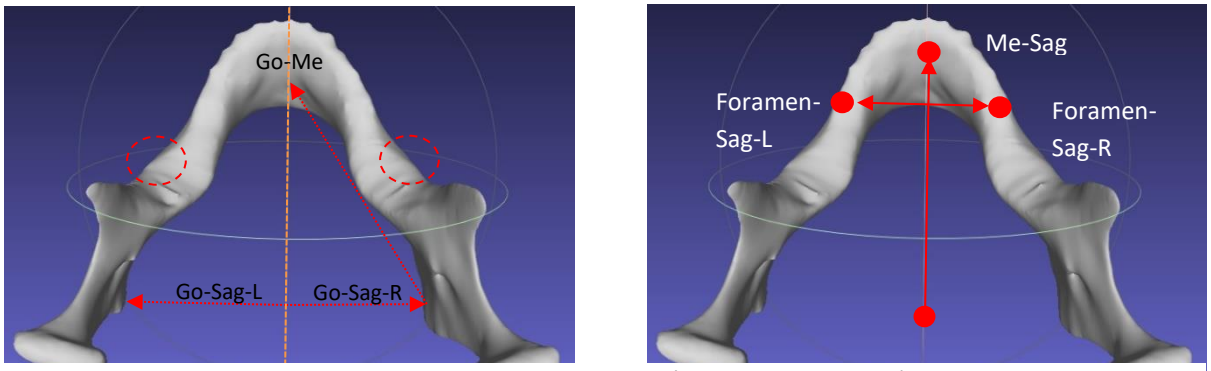


*Figure 40: Alternative Landmarks (Illustration: BI Giddy)*

# 5. Finite Element Analysis

Initially, 4 mean mandible/plate models were constructed as a test for the final FEA setup, 2 male and 2 female. The mean population mandible was generated from the SSM and the parametric and CS plates were created from the CAD template. Material assignments were created and allocated to the appropriate geometry. The remaining boundary conditions such as the mandible muscle forces, supports and meshes were applied based on relevant literature. The mean models were able to offer an estimate of the structural behavior and performance of the reconstruction plates under loading. Afterwards, the male and female mandible with the most curvature were chosen as the FEA models. The corresponding plate configurations (hemimandible, symphyseal and lateral short) were created for each mandible. Each FEA setup was identical, and the equivalent Von-mises stresses were analyzed in order to determine the structural performance of the parametric reconstruction plate vs. the CS reconstruction plate. The software used to conduct this FEA was ANSYS 2019 R3 – Student License (ANSYS, Pennsylvania, Canonsburg). It is important to note that the student license of ANSYS has a maximum facet count of 300 and maximum mesh nodal count of 32 000.

## 5.1. Mandible Model Preparation

The SSM exports the mandible model in .STL format with ± 90 000 faces. A large number of faces such as this will exceed the maximum facet count in ANSYS. In order to edit this model, the mandible file was imported into Fusion360 (Autodesk, California, San Rafael, USA). Figure 41 displays the meshing panel with the original mean mandible model.

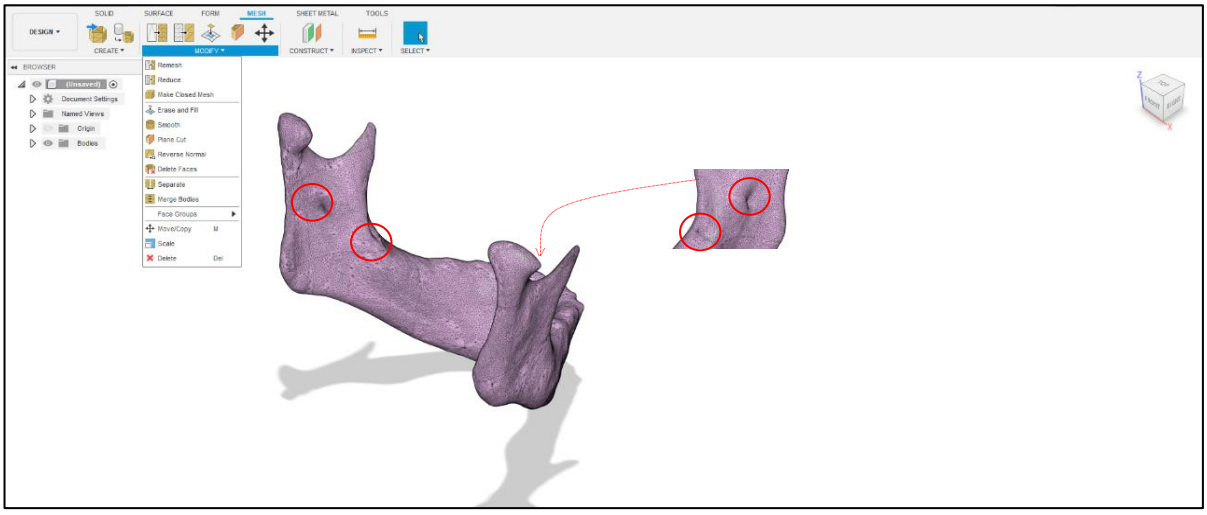


*Figure 41: Mean Mandible Model in Fusion360 Mesh Editor (Illustration: BI Giddy)*

When reducing such a large face count to a significantly smaller count, intersection of the mesh can occur creating regions that produce errors in later FEA studies. There are several regions that need to be repaired on this model, circled in Figure 41. The region around the mandibular foramen on the left and right ramus regions as well as the superior portion of the angle on the left and right side of the mandible. The affected mandible regions were erased and filled with a uniform face mesh. This deletes the defective region on the mesh and replaces the facets. The uniform mesh fills the selected region with regular-shaped triangular elements.

Once the problematic areas on the mesh have been repaired the face count can be lowered and the mesh can be converted into a solid body. The mesh was reduced according to a density value. The density value chosen for the mandible model was ρ = 0.0027. This reduced the face count to 250 faces. The model must now be converted to a base feature or a solid body in order to provide a workable model. The reduced mandible model was saved as an .stl file and imported into *Autodesk Inventor*. On the navigation tree, the model was highlighted converted to a base feature. This rendered a solid body that was manipulated in the design space.

## 5.2. Model Setup

Similar to the comparison test, the FEA was performed on the same three plate configurations. The mandibles were considered as parabolic curves with the turning point the Go-Me landmark coordinate and the x-intercepts as the Go-R and Go-L coordinates. A curvature plot of the male and female mandibles was generated. The male and female mandible with the most curvature were selected as the "worst-case" models. Each plate configuration had already been generated for the comparison test in Chapter 4. Before alignment, fillets, adjustment of the holes and the rounding of sharp corners were applied to each male and female plate configuration.

The lateral short defect was simulated between the first molar and first premolar, approximately 15 mm long. The symphyseal defect was simulated between the left and right canines, approximately 20 mm long. The hemimandible defect was simulated between the angle and the canine, approximately 35 mm long. The corresponding reconstruction plates were generated, the holes were edited to correspond with trends in literature and the final edits were added.

The number of screws on either side of the defect as well as the spacing is not well documented but some conclusions can be drawn from literature. Smaller defects such as fractures and short resections have two fixation points on either side of the defect. (Aquilina et al., 2013; Arbag, Korkmaz, Ozturk and Uyar, 2008; Oguz et al., 2009). While larger defects that may extend from the menton to the just below the sigmoid notch have upwards of three fixation points on either side of the defect (Al-Ahmari et al., 2015; Gutwald, Jaeger and Lambers, 2016; Knoll, Gaida and Maurer, 2006; Narra et al., 2014; Wu, Lin, Liu and Lin, 2017). Therefore, the lateral short plate and symphyseal plates have two screws on either side of the defect and the hemimandible plate has 3 screws on either side of the defect.

A major disadvantage of CS plate designs is that they are required to fit the underlying bone of the mandible perfectly in order to avoid alignment alterations, which place severe stress on the underlying mandible (Guruprasad, Shetty, Prabhakar and Hemavathy, 2011). The locking plate system is a mandible reconstruction plate that accepts screws that lock to the plate by way of a secondary thread under the head of the screw. These plates achieve stability by locking the screw to the plate (Gutwald, Alpert and Schmelzeisen, 2003). A major advantage of the locking plate system is that plate-to-bone contact becomes unnecessary, this reduces the risk of alignment alterations, it reduces mandible wear and plate adaption becomes easier as the plate no longer needs to perfectly match the underlying bone geometry (Collins, Pirinjian-Leonard, Tolas and Alcalde, 2004).

Using the principle of the locking plate system, each mandible and the corresponding reconstruction plate were aligned in Autodesk Inventor. The reconstruction plate was spaced 1 mm from the face of the mandible. The file was exported from Autodesk Inventor Professional in the Parasolid Binary

format (.x_b). The screws were simulated in Ansys Spaceclaim as cylinders with a diameter of 4 mm (Knoll, Gaida and Maurer, 2006). The Boolean operation *join* is used to create the screws. The result is a bigger solid which consists of all volume enclosed by the newly formed sketch. This mimics the locking interface between the plate/screw and the mandible/screw. Figure 42 shows the final FEA setups in Autodesk Inventor.

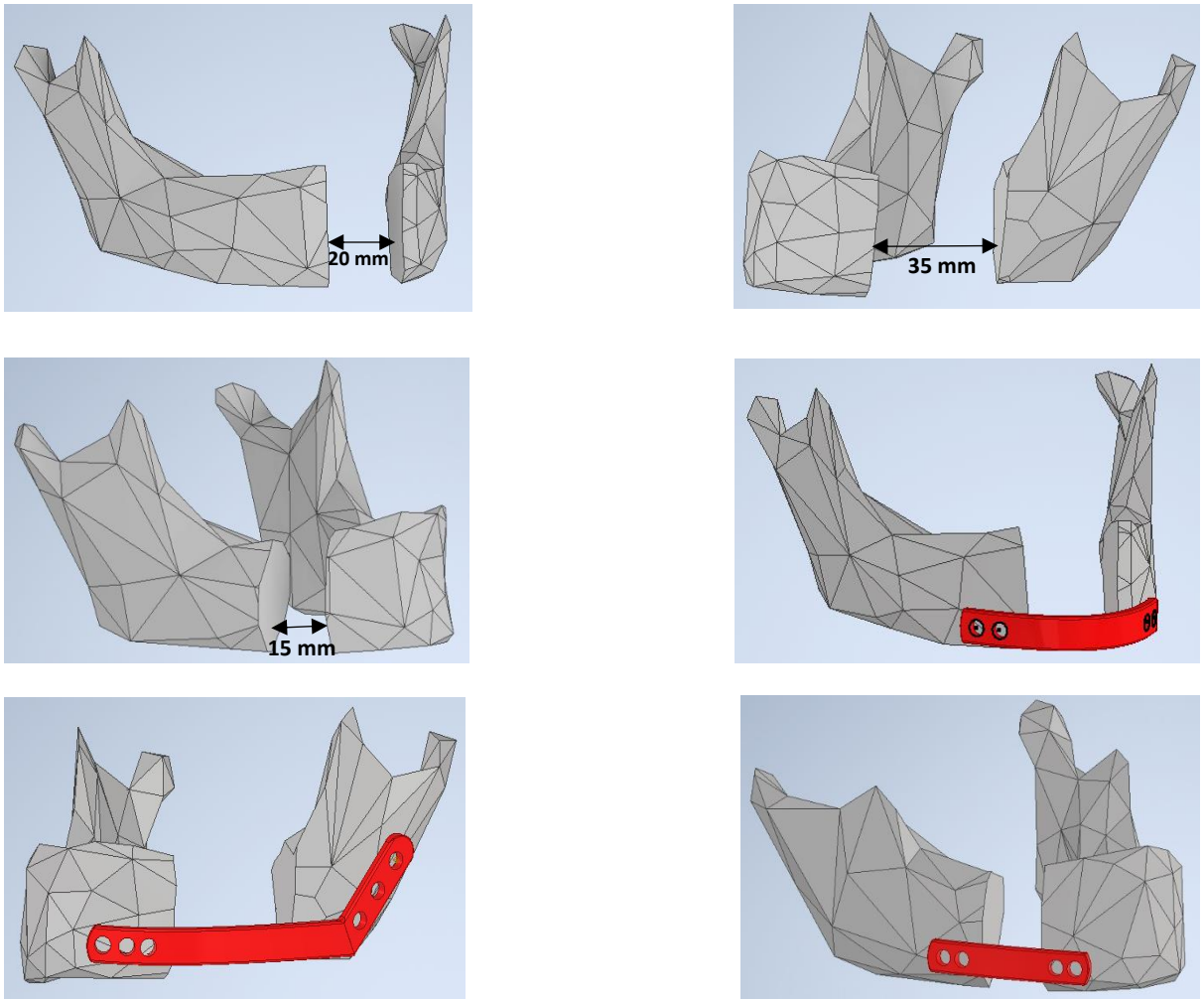


*Figure 42: Final Analysis Setup (Illustration: BI Giddy)*

## 5.3. Material Assignment

The material properties of a finite element study are fundamentally important in recreating an accurate simulation. Different materials have varying material properties and therefore have different mechanical behavior. An important assumption is the mechanical properties of mandible bone.

As discussed in Chapter 2 there are numerous factors that can affect the material properties of mandible specimens. Treatment factors due to benign and malignant tumors have a direct effect on bone health (Understanding the Effects of Cancer Treatment on Bone Health, 2020). Radiation and Chemotherapy as well as steroids, which are usually prescribed to prevent chemotherapy induced nausea, may impact bone health. Other factors that affect the material properties of mandible bone include the sex of the mandible, the region the mandible bone was sampled from, the mechanical

testing methods, the sample size, cadaver age, bone dehydration, test and storage temperature, specimen age, bone porosity, and imagining techniques.

The final point to consider in the material assignment step is the volume or percentage of cortical to trabecular bone, which is unreported in literature. This ratio will vary greatly due to the factors listed above. A material simplification is needed in order to produce an accurate FEA result.

Andersen, Pedersen and Melsen (1991) state that results are minimally affected when a distinction is not made between cortical and cancellous bone, this allows the simplification of the model to a single type of alveolar bone. Therefore, it is assumed that the mandible is homogenous and isotropic. The material *Cortical Iso* was created in ANSYS Workbench.

The material properties for mandible bone and Ti-6Al-4V are displayed in Table 14.

*Table 14: Material Properties of Titanium Alloy and Cortical Bone*

| **Material** | **Temperature (˚C)** | **Young's Modulus (Pa)** | **Poisson's Ratio** | **Bulk Modulus (Pa)** | **Shear Modulus (Pa)** |
|---|---|---|---|---|---|
| **Cortical Bone** | 20 | 1.37E+10 | 0.3 | 1.147E+10 | 5.26E+09 |
| **Ti-6Al-4V** | 20 | 1.01E+09 | 0.323 | 1.0075E+11 | 4.40E+10 |

## 5.4. Boundary Conditions

A boundary condition is a place on a structure where the external force or displacement are known at the beginning of the FEA. The boundary conditions are the manner in which the interaction between the structure and the environment is modelled. For an FEA to be solvable every point on the boundary layer of the structure must have a known displacement or force condition.

The mandible supports, aside from the muscles, are an important aspect of the FEA. Without the supports the object is essentially floating in space. During biting the mandibular condyle is firmly secured in the TMJ. The top of the condyles were constrained in all directions via fixed supports to simulate this. As previously stated, the lateral incisors were constrained in the vertical direction. It is not sufficient to purely use a bite force and ignore muscle loading or to use muscle loading and ignore the contact forces on the teeth. Based on our understanding of the biomechanics of the mandible, the values outlined by Wu, Lin, Liu and Lin (2017) in Chapter 2 were used in this FEA. Figure 43 shows the mandible muscle attachment sites, their locations and the constraints.

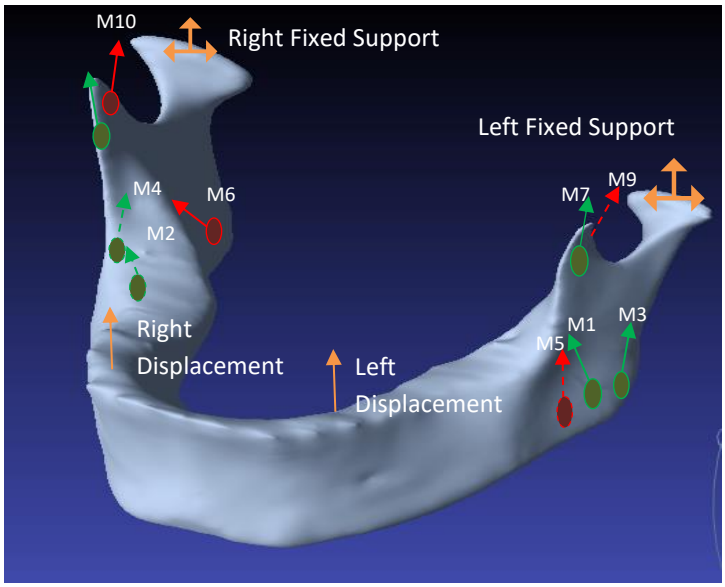


*Figure 43: Boundary Conditions and Supports (Illustration: BI Giddy)*

### 5.4.1. Thermal Load

In order for the CS reconstruction plate to retain the bent shape it must undergo plastic deformation. This introduces residual stress, cracks and weak points into the plate. The bending site is often the region of failure on the implant. When performing a FEA on the CS reconstruction plate it is important to model this effect. O'Toole, Karpanan and Feghhi (2006) and Murugan, Kurian, Jayaprakash and Sreedharapanickar, (2015) describe several methods for pre-loading bolts and flanged joints. A method used is the thermal load, which is governed by the Equation 6, below.

$$\sigma = E \times \alpha \times \Delta T \tag{6}$$

Where σ* is the thermal stress, E is Young's Modulus of Elasticity, α is the thermal expansion coefficient and ΔT is the change in temperature. The thermal load is applied to the CS reconstruction plate to model the effects of plastic deformation on the stress distribution during loading.

The residual stress value in the plate is arbitrary. The value will vary due to a variety of factors such as bending, initial temperature of the plate, plate length, plate thickness and the number of screws etc. These factors are in turn affected by biomechanical factors such as post-operation muscle strength, material properties of the patient's bone, defect region, defect size, mandible geometry, age and sex of the patient. Due to the range of variables it is clear that for each CS plate the residual stress value will vary. It is more important that a distinction be made between the CS and parametric plates. Therefore, in order to create a consistent FEA setup an assumption of 150 ˚C was chosen for the thermal load. With an initial temperature of 20 ˚ C, this will apply a stress of 105 MPa to the CS reconstruction plate.

## 5.5. Mesh Independence Study

Prior to performing FEA simulations a mesh independence study was performed. When performing the mesh independence study, it is important to ensure two things: That the values of interest have reached a steady state solution and these values have imbalances of less than 10 %. A mesh sizing operator was assigned to the parametric plate. An initial mesh element size of 10.252 mm was used as the initial point, generating a coarse mesh. Mesh refinements were added, and the nodal count and maximum stresses were recorded and plotted. The finest mesh varied from plate to plate as the larger plates naturally contain more elements, but the element count was increased until solver failure due to the numerical limits on the ANSYS student license. Mesh independence was performed on the parametric reconstruction plate only, as solution convergence was achieved at approximately the same number of mesh elements on the parametric and CS reconstruction plates .

The mean mandible was generated from the SSM and the corresponding parametric and CS reconstruction plates were aligned, imported, and processed. This FEA and mesh independence study was used as the control group. Figure 44 illustrates the initial plate and mandible setup. A simple shortened plate with two screw points was used. Figures 45 and 46 show the mesh independence study for the mean parametric and mean CS plates, respectively. It is clear that as the mesh gets finer and the number of elements increase the study reaches a steady state solution at ± 9 000 elements. Therefore, future FEA on this mandible-plate setup will produce accurate results from 9 000, or more, elements. The male and female mesh independence studies converged at an average of 8600 nodes and 7 000 nodes, respectively.

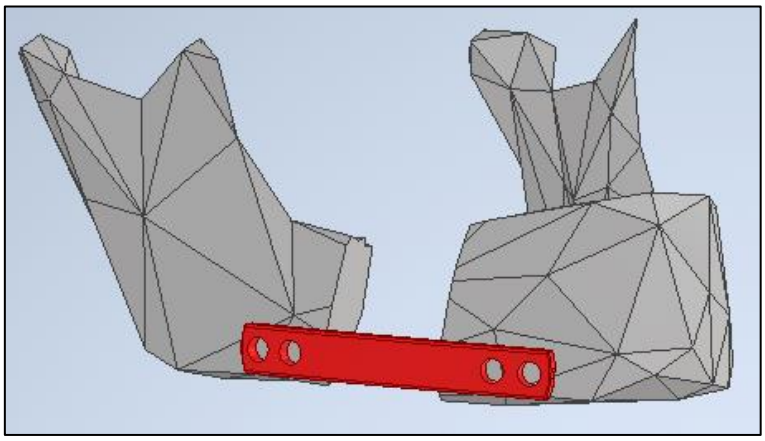

*Figure 44: Initial Test Setup (Illustration: BI Giddy)*

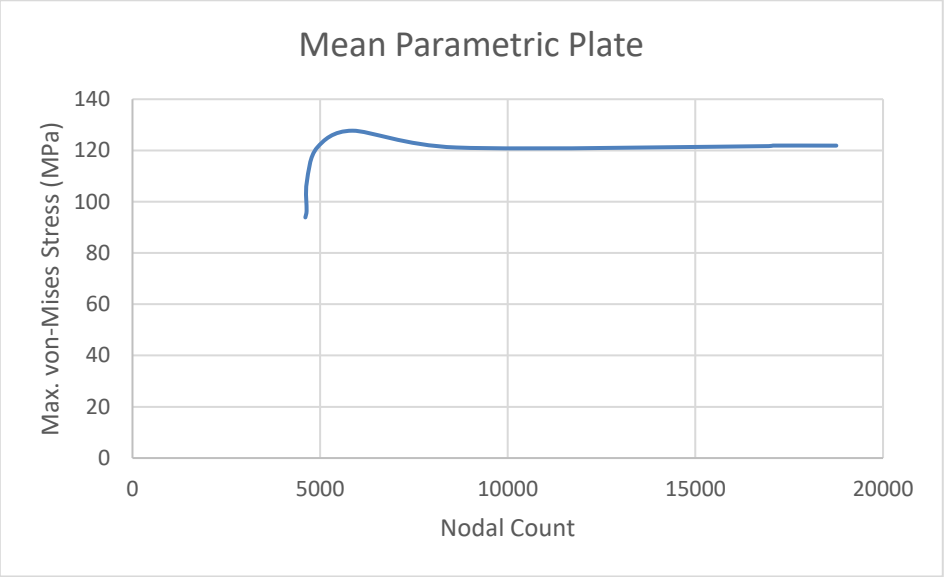


*Figure 45: Mean Parametric Mesh Independence Study (Illustration: BI Giddy)*

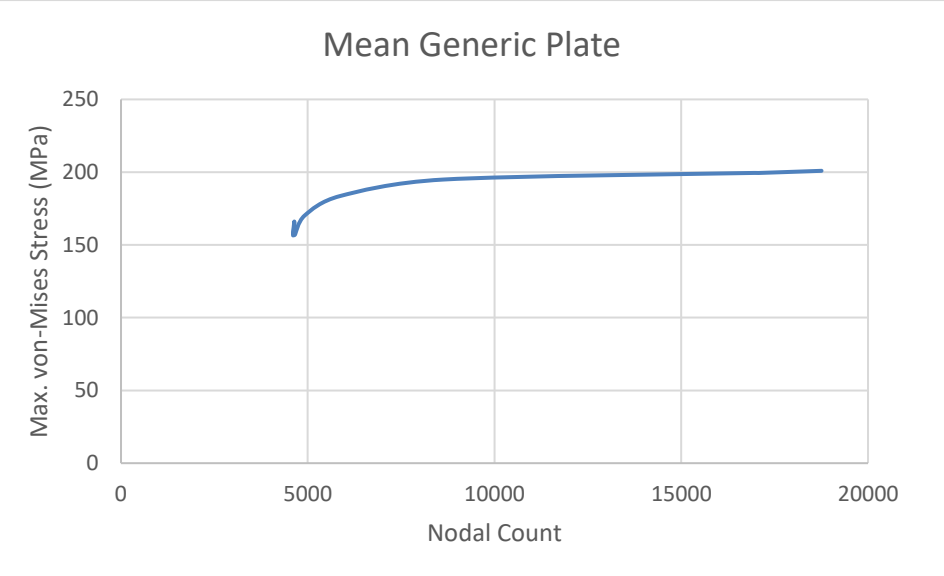


*Figure 46: Mean Generic Mesh Independence Study (Illustration: BI Giddy)*

## 5.6. Results

The evaluation of the FEA results was performed by analyzing the maximum von-Mises stress in the mandible reconstruction plates. Hand calculations were performed as a means of validation, and literature results were compared.

### 5.6.1. Lateral Short Plate

Figures 47-a and -b illustrate the von-Mises stress distributions in the lateral short plates aligned with the 27$^{th}$ male mandible. The FEA indicates that the maximum von-Mises stress in the parametric reconstruction plate and the CS reconstruction plate were 132.63 MPa and 224.91 MPa respectively. Both stress were less than the ultimate tensile strength of 900 MPa. However, the maximum von-Mises stress in the CS model was 1.7 times greater than the parametric model.

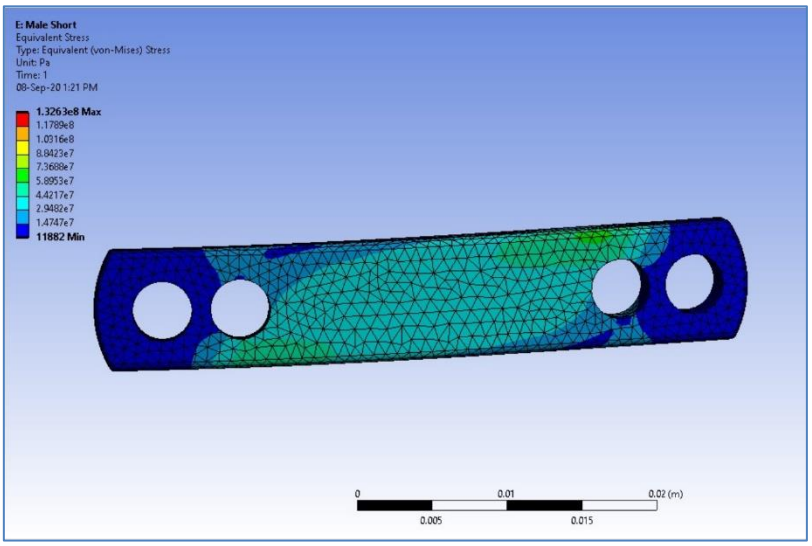


*a) Parametric Reconstruction Plate*

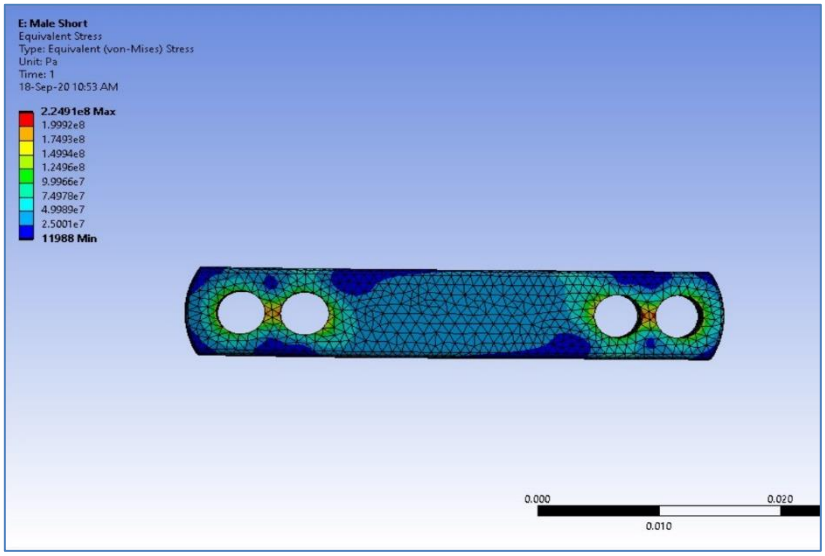


*b) CS Reconstruction Plate*

*Figure 39: Male Lateral Short FEA Results (Illustration: BI Giddy)*

Figures 48-a and -b illustrate the von-Mises stress distributions in the lateral short plates aligned with the 35$^{th}$ female mandible. The FEA indicates that the maximum von-Mises stress in the parametric reconstruction plate and the CS reconstruction plate were 222.9 MPa and 262.58 MPa respectively. Both stress were less than the ultimate tensile strength of 900 MPa. However, the maximum von-Mises stress in the CS model was 1.2 times greater than the parametric model.

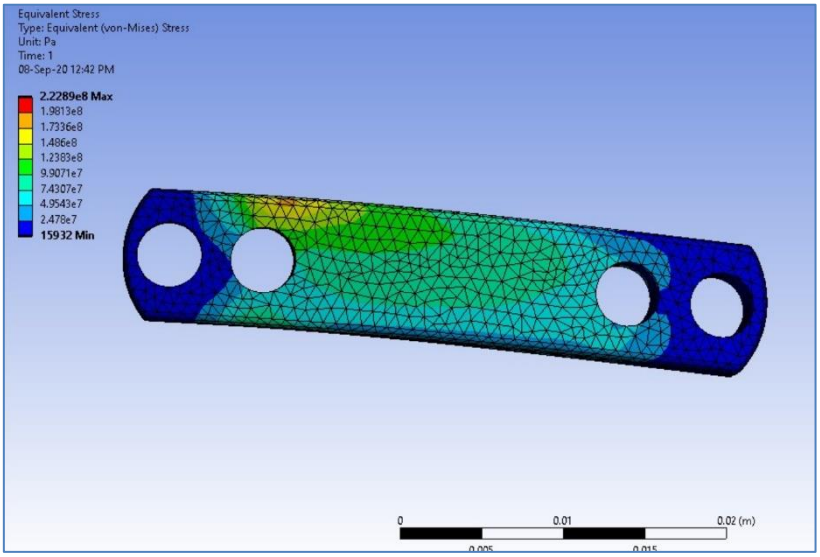


*a) Parametric Reconstruction Plate*

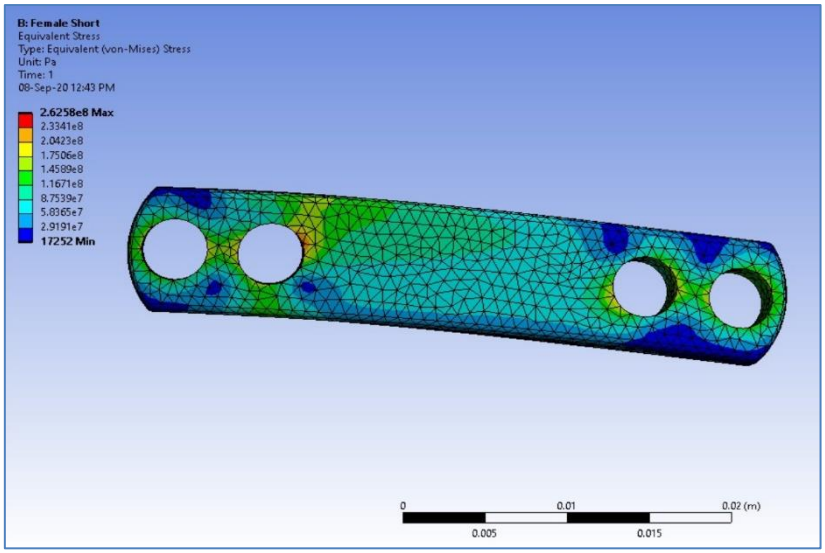


*b) CS Reconstruction*

*Figure 40: Female Lateral Short Plate FEA Results (Illustration: BI Giddy)*

## 5.6.2. Symphyseal Plate

Figures 49-a and -b illustrate the von-Mises stress distributions in the symphyseal plates aligned with the 27$^{th}$ male mandible. The FEA indicates that the maximum von-Mises stress in the parametric reconstruction plate and the CS reconstruction plate were 102.31 MPa and 223.09 MPa respectively. Both stress were less than the ultimate tensile strength of 900 MPa. However, the maximum von-Mises stress in the CS model was 2.2 times greater than the parametric model.

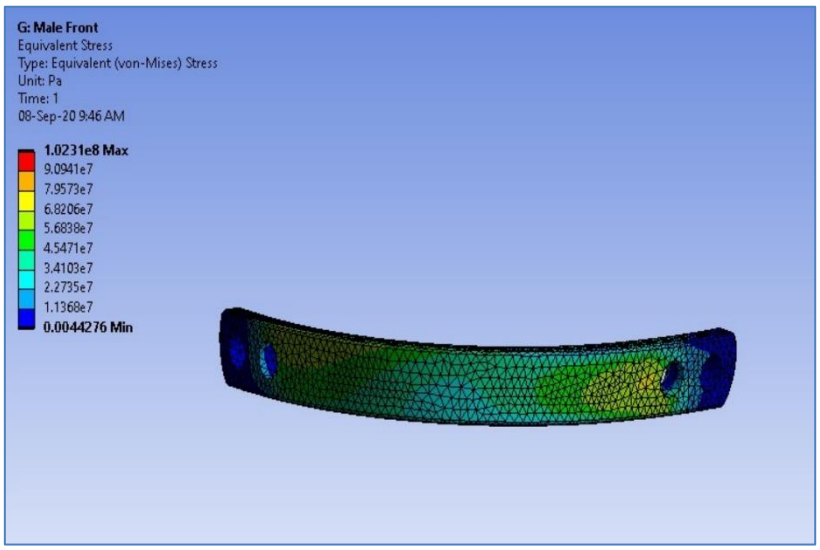


*a) Parametric Reconstruction Plate*

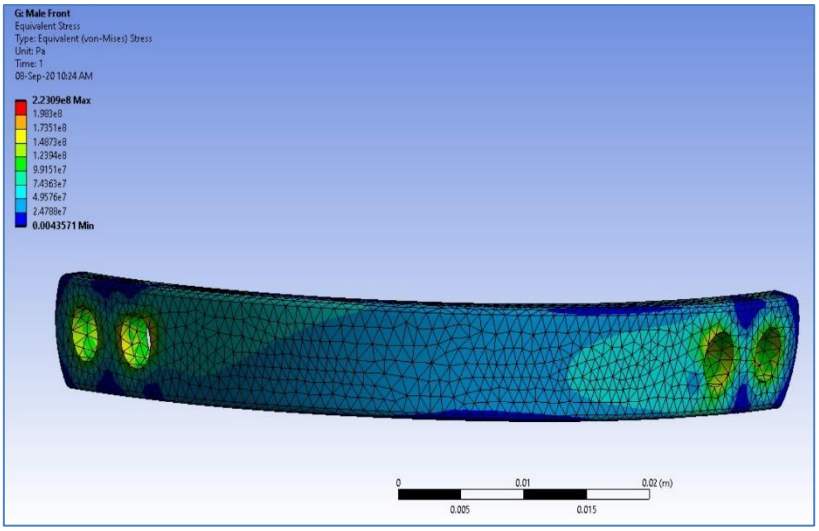


*b) CS Reconstruction Plate*

*Figure 49: Male Symphyseal FEA Results (Giddy, 2020)*

Figures 50-a and -b illustrate the von-Mises stress distributions in the symphyseal plates aligned with the 35$^{th}$ female mandible. The FEA indicates that the maximum von-Mises stress in the parametric reconstruction plate and the CS reconstruction plate were 123.8 MPa and 227.01 MPa respectively. The maximum von-Mises stress in the CS model was 1.84 times greater than the parametric model.

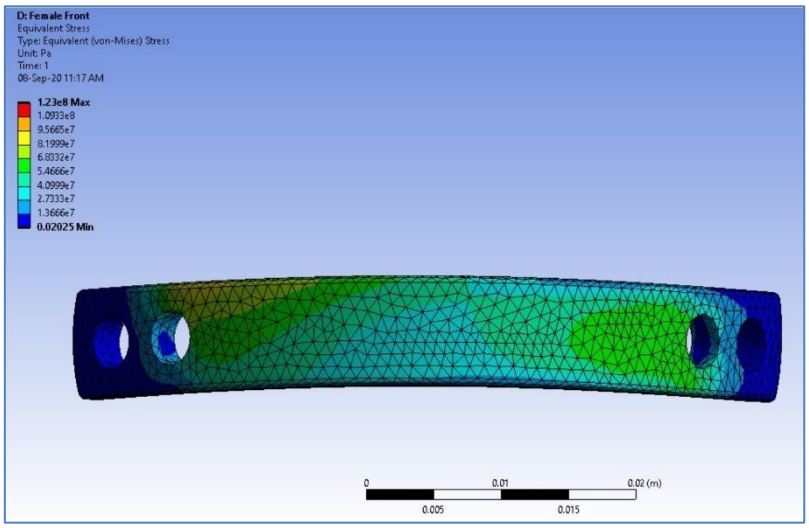


*a) Parametric Reconstruction Plate*

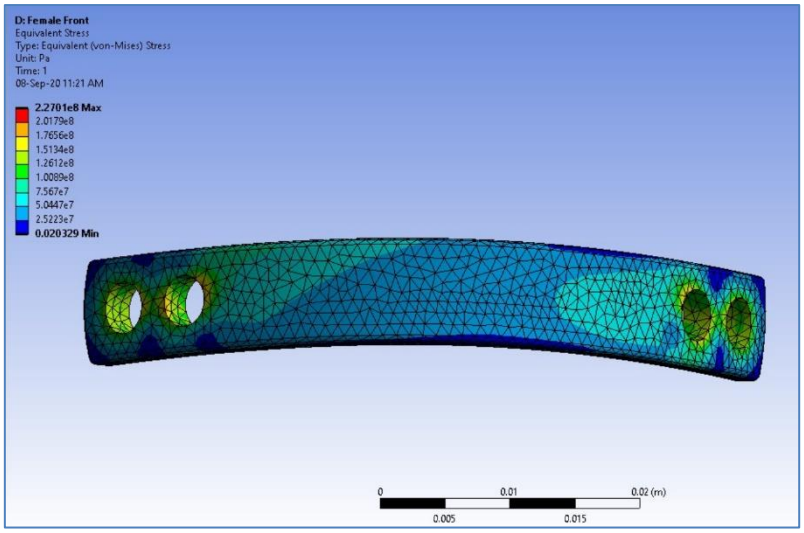


*b) CS Reconstruction Plate*

*Figure 41: Female Symphyseal FEA Results (Giddy, 2020)*

### 5.6.3. Hemimandible Plate

Figures 51-a and -b illustrate the von-Mises stress distributions in the hemimandible plates aligned with the 27$^{th}$ male mandible. The FEA indicates that the maximum von-Mises stress in the parametric reconstruction plate and the CS reconstruction plate were 426.16 MPa and 474.5 MPa respectively.

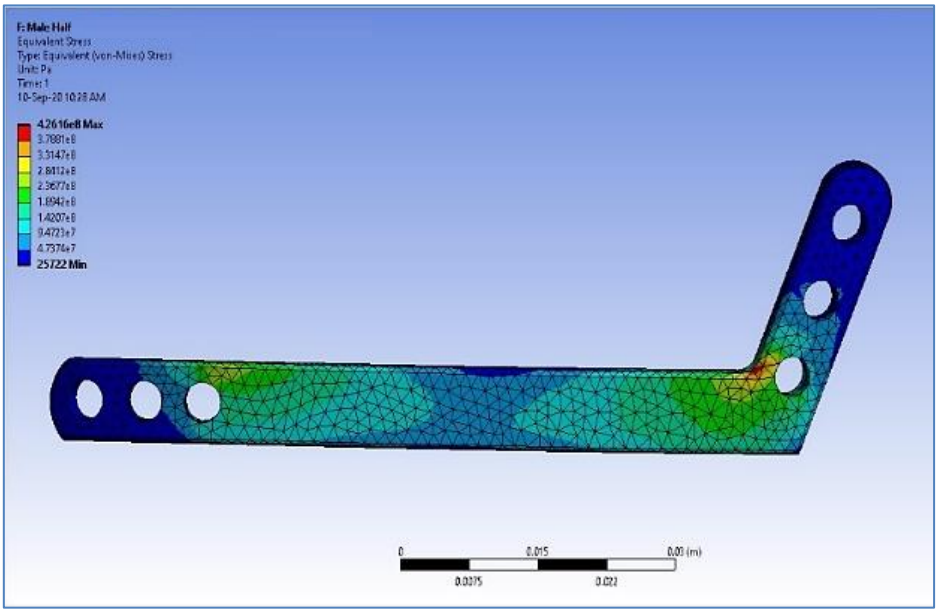


*a) Parametric Reconstruction Plate*

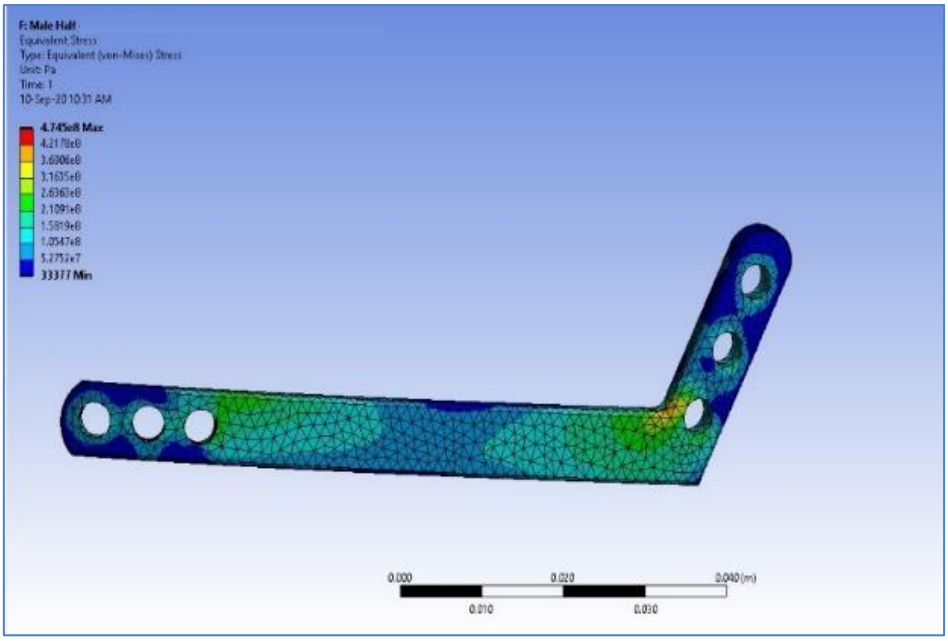


*b) CS Reconstruction Plate*

*Figure 51: Male Hemimandible FEA Results (Illustration: BI Giddy)*

Figures 52-a and -b illustrate the von-Mises stress distributions in the hemimandible plates aligned with the 35$^{th}$ female mandible. The FEA indicates that the maximum von-Mises stress in the parametric reconstruction plate and the CS reconstruction plate were 623.38 MPa and 652.25 MPa respectively.

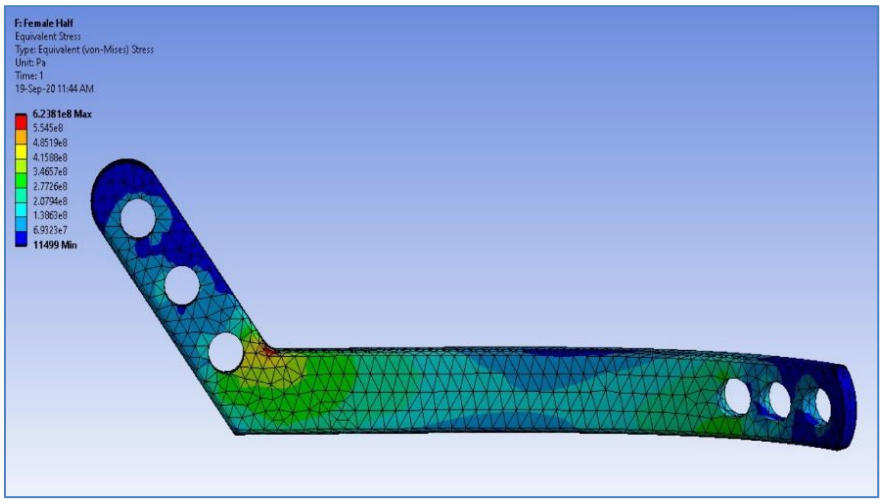


*a) Parametric Reconstruction Plate*

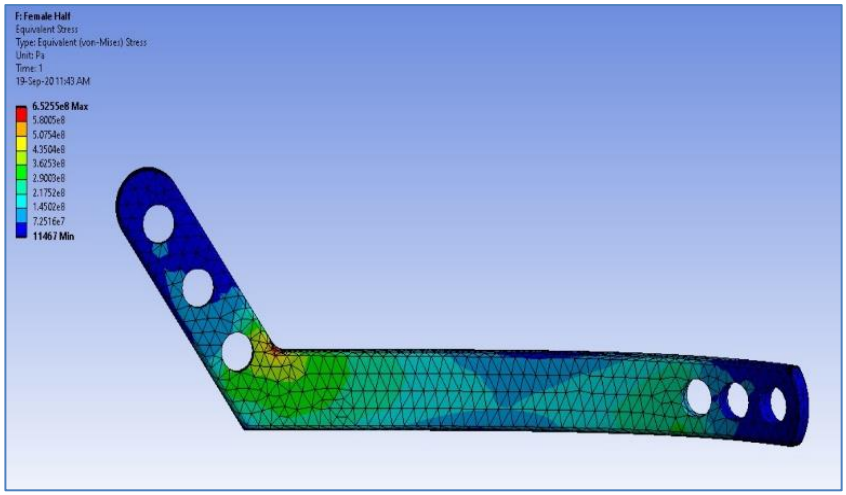


*b) CS Reconstruction Plate*

*Figure 52: Female Hemimandible FEA Results (Illustration: BI Giddy)*

In all cases, both male and female, the stresses were less than the ultimate tensile strength of 900 MPa. However, there was concern of a stress concentration at the angle. Stress concentrations appear at sharp corners. As the corner angle cannot be altered due to the fact that the measurement is directly related to the mandible geometry, a solution must be found.

In general, FEA cases it is common for the stress concentration peak to be unknown, and there is no alternative to doing a mesh convergence study (Abbey, 2017). A method used to obtain an accurate result from the affected region, is to apply mesh refinement to the area and average the values of the surrounding elements. Alternatively, it can be assumed that the localized peak stress regions would yield and relieve (Abbey, 2017). Comparing FEA values to hand calculations, the localized stress can be ignored and the nominal stresses (stresses calculated on the cross section of a specimen) can be dealt with.

## 5.7. Model Validation

### 5.7.1. Hand Calculations

The FEA models for each mandible/plate combination are statically indeterminate. When analyzing the force and moment reactions at the fixed supports, the condyles, assumptions need to be made in order to solve for the unknowns. An equal loading assumption will mean that the forces on the left and right condyle are the same. As the mandible resections shift and get larger these reactions will naturally change, becoming larger or smaller and venturing further from the equal loading assumption. The reaction forces at the condyles for each FEA model were measured in ANSYS and the values confirm that the loading is not equal. However, the lateral short plate reaction values for the male and female mandibles are within ±10 % of the equal loading assumption. With this information it was decided that hand calculations would only be performed on the lateral short models.

Secondly, due to the complexity of the boundary conditions the model needs to be simplified. For the calculations only one fixed support was present at a time, which allowed for the forces and moments to be solved. These values were compared with the force and moment reaction values in Ansys. The

positional vectors of the muscles, muscle vectors and the positional vectors of the fixed supports at the left and right condyle were recorded. The positional vectors between each muscle and the respective support were calculated. Using these vectors and the muscle forces the moment reactions were calculated. Figure 43 show the free-body diagram model that was used in the hand calculations. All forces were calculated using the equations of equilibrium. The moments were calculated by taking the sum of the moments created by the forces about the left and right condyle, respectively. The following tables show the Ansys reaction values and the calculated values. An error of ± 10 % was used. All vector tables can be found in Appendix C.

Table 15 shows the force reactions for the male lateral short model assuming equal loading as well as the upper and lower bounds.

*Table 15: Calculated Male Force Reactions*

| | X (N) | Y (N) | Z (N) | Mag (N.m) |
|---|---|---|---|---|
| **Upper Bound @ 10%** | -178.272 | 55.088 | -610.005 | 6.38E+02 |
| **Force Reaction** | -162.065 | 50.08 | -554.55 | 5.80E+02 |
| **Lower Bound @ 10%** | -145.859 | 45.072 | -499.095 | 5.22E+02 |

Table 16 shows the *Ansys* reaction forces for the male lateral short model.

*Table 16: Measured Male Force Reactions*

| | X (N) | Y (N) | Z (N) | Mag (N.m) |
|---|---|---|---|---|
| **Force Reaction Right** | -177.64 | 54.685 | -609 | 636.7318 |
| **Force Reaction Left** | -145.9 | 45.475 | -499.1 | 521.9728 |

Table 17 shows the calculated moment reactions at the right fixed support (left is suppressed) for the male lateral short plate.

*Table 17: Calculated Moment Reactions at the Right Fixed Support - Male*

| | X | Y | Z | Mag | Units |
|---|---|---|---|---|---|
| **Upper Bound @ 10%** | 7.26055 | 81.39252 | 4.06241 | 81.81663 | N.m |
| **Calculated Moment Reaction** | 6.6005 | 73.9932 | 3.6931 | 74.37876 | N.m |
| **Lower Bound @ 10%** | 5.94045 | 66.59388 | 3.32379 | 66.94088 | N.m |

Table 18 shows the Ansys force and moment reactions at the right fixed support (left is suppressed) for the male lateral short plate.

*Table 18: Measured Force and Moment Reactions at the Right Fixed Support - Male*

| | X | Y | Z | Mag | Units |
|---|---|---|---|---|---|
| **Force Reaction Right** | -324.13 | 100.16 | -1109.1 | 1159.8 | N |
| **Moment Reaction Right** | 6.6427 | 70.326 | 3.9665 | 70.75 | N.m |

Table 19 shows the calculated moment reactions at the left fixed support (right is suppressed) for the male lateral short plate.

*Table 19: Calculated Moment Reactions at the Left Fixed Support - Male*

| | X | Y | Z | Mag | Units |
|---|---|---|---|---|---|
| **Upper Bound @ 10%** | 4.21553 | -43.5224 | -5.33478 | 44.05029 | N.m |
| **Calculated Moment Reaction** | 3.8323 | -39.5658 | -4.8498 | 40.04572 | N.m |
| **Lower Bound @ 10%** | 3.44907 | -35.6092 | -4.36482 | 36.04115 | N.m |

Table 20 shows the Ansys force and moment reactions at the left fixed support (right is suppressed) for the male lateral short plate.

*Table 20: Measured Force and Moment Reactions at the Left Fixed Support - Male*

| | X | Y | Z | Mag | Units |
|---|---|---|---|---|---|
| **Force Reaction Left** | -324.13 | 100.16 | -1109.1 | 1159.8 | N |
| **Moment Reaction Left** | 3.5396 | -39.313 | -5.2851 | 39.824 | N.m |

Table 21 shows the calculated moment reactions at the right fixed support (left is suppressed) for the female lateral short plate.

*Table 21: Calculated Moment Reactions at the Right Fixed Support - Female*

| | X | Y | Z | Mag | Units |
|---|---|---|---|---|---|
| **Upper Bound @ 10%** | -18.9244 | 55.06534 | 4.73946 | 58.41906 | N.m |
| **My Moment Reaction** | -17.204 | 50.0594 | 4.3086 | 53.10824 | N.m |
| **Lower Bound @ 10%** | -15.4836 | 45.05346 | 3.87774 | 47.79742 | N.m |

Table 22 shows the Ansys force and moment reactions at the right fixed support (left is suppressed) for the female lateral short plate.

*Table 22: Measured Force Moment Reactions at the Right Fixed Support - Female*

| | X | Y | Z | Mag | Units |
|---|---|---|---|---|---|
| **Force Reaction Right** | -324.13 | 100.16 | -1109.1 | 1159.8 | N |
| **Moment Reaction Right** | -18.604 | 46.494 | 3.8797 | 50.206 | N.m |

Table 23 shows calculated moment reactions at the left fixed support (right is suppressed) for the female lateral short plate.

*Table 23: Calculated Moment Reactions at the Left Fixed Support - Female*

| | X | Y | Z | Mag | Units |
|---|---|---|---|---|---|
| **Upper Bound @ 10%** | -19.68406 | -60.40408 | 13.24246 | 64.8959 | N.m |
| **My Moment Reaction** | -17.8946 | -54.9128 | 12.0386 | 58.99627 | N.m |
| **Lower Bound @ 10%** | -16.10514 | -49.42152 | 10.83474 | 53.09665 | N.m |

Table 24 shows the Ansys force and moment reactions at the left fixed support (right is suppressed) for the female lateral short plate.

*Table 24: Measured Force and Moment Reactions at the Left Fixed Support - Female*

| | X | Y | Z | Mag | Units |
|---|---|---|---|---|---|
| **Force Reaction Left** | -324.13 | 100.16 | -1109.1 | 1159.8 | N |
| **Moment Reaction Left** | -17.515 | 57.298 | 12.655 | 61.237 | N.m |

From these tables it is clear that the hand calculations and measured Ansys values agree based on an error of ± 10 %.

### 5.7.2. Literature Comparison

This section will discuss various mandible FEA literature and report the maximum stress values measured in the respective plate configurations, the presence and setup of physical testing, result validation, mandible gender and the modelling procedure for the CS (if there was a comparison in the study).

Ackland et al., (2017) performed FEA on a condyle replacement implant. A maximum stress of 284.22 MPa was reported, no information on physical testing, theoretical result validation and mandible gender information was given. Arbag et al., (2008) performed FEA on 14 different short plate configurations. The lowest maximum stress value was 200 MPa and the highest maximum stress present in the configurations was 460 MPa. No information on physical testing, theoretical result validation, mandible gender information or CS modelling procedure was given. Feller et al., (2003) performed a FEA on a short plate configuration and analyzed the data of 277 mandible reconstruction patients. The maximum stress in the authors FEA study was 700 MPa. No numerical comparisons between the stress values in the simulation and the patients were made. Mandible gender information and modelling of the implant bending was unreported. Vajgel et al., (2013) performed FEA on short plates of varying thickness (1.0, 1.5, 2.0, and 2.5 mm). the lowest maximum stress was 113 MPa and the maximum recorder stress across the varying plates was 274 MPa. No information on physical testing, theoretical result validation, mandible gender and CS modelling procedure was provided.

Gutwald, Jaeger and Lambers. (2017) performed FEA on a hemimandible plate. A maximum stress of 509 MPa was recorded in the standard plates. No information on theoretical result validation, CS modelling procedure or mandible gender information was given. Fatigue testing was performed on the standard and custom plates, but no experimental results were compared to the FEA simulation. Knoll, Gaida and Maurer, (2006) performed a FEA on a various hemimandible plate configurations. The maximum stress was 1363 MPa when 2.7 mm diameter screws were used and 525 MPa when 4 mm screws were used. No physical testing or theoretical result validation was performed. CS modelling procedure and mandible gender were unreported. Narra et al., (2014) performed FEA on two hemimandible plates. Plate 1 extended to the mandibular condyle and Plate 2 stopped at the angle. The maximum stresses in the plates were 109 MPa and 63 MPa, respectively. There are inconsistencies in this paper as physical testing was performed but a load of more than 65 N could not be applied to Plate 1 as the testing apparatus continued to fail, while exceedingly high forces were applied to plate 2 in order to observe any significant deflection. Rupture in plate 2 occurred at forces greater than 950 N. Muscle forces were applied similar to Vajgel et. al (2013) except these authors do not provides values. They detail muscle weight and vectors, allowing other researchers to calculate muscle values based on area of attachment. Narra et al. (2014) did not provide muscle area of

attachment information, leaving the connection between the theoretical results and physical tests unclear.

Wu, Lin, Liu and Lin, (2017) performed a FEA on a CS symphyseal plate as well as a Novel-Hybrid (NH) model of the author's own design. The maximum stress in the CS plate was 546 MPa and in the NH plate was 121 MPa. No information on theoretical results validation, the modelling of the CS plate and mandible gender was provided. Fracture testing was performed but no comparisons to theoretical results were made. Li et al., (2014) performed a FEA on a customized symphyseal plate. The maximum reported stress was 616.43 MPa and no physical testing, theoretical result validation and mandible gender information was provided.

There is no consensus that can be drawn from literature at this time, due to the range of values that similar plate configurations exhibit and the numerous variables that will affect FEA results.

## 5.8. Discussion

The FEA results from literature as well as the simulation indicate that customized mandible reconstruction plates free of residual stress due to plastic deformation have lower maximum stresses and are therefore less likely to fail compared to CS reconstruction plates. The female FEA results are noticeably higher than the male FEA results. This could be due to the mandible with the smaller surface area experiencing higher stresses. The force and moment reactions recorded by Ansys are within the 10 % limit specified by the hand calculations. Before the implant is used in a medical setting physical testing is advised to confirm the FEA results.

There are some limitations to the FEA study. Firstly, the mandible was assumed homogenous and isotropic. Although this assumption was based on relevant literature, bone is made up of two different material types with varying material properties. There will naturally be difference in results no matter how small. Secondly, the residual stress in the CS plate was modelled using a thermal load. The literature method for modelling CS plates is not clear and the thermal load may not accurately express the effect of the plastic deformation on the plate. However, it is valid because it introduces an external stress to the CS reconstruction plate and makes a clear distinction between the two plates. Finally, FEA results should be confirmed with physical tests before proceeding with implantation.

The inconsistencies between simulations in literature need to be discussed. Plate length is a variable that is not routinely reported. Naturally, this value would vary depending on resection length, surgical factors and resection region. However, no trends across FEA literature can be recorded as plate length vs. resection length is not discussed. Resection length is another variable that is absent. Larger tumors, cysts and lesions or more severe mandible trauma will require larger mandible resections, but this value is not reported and thus it is difficult to simulate defects as the values are merely estimations for the purpose of reporting theoretical results.

Another variable is the type and number of screws. Some authors make use of locking screws, which as previously discussed, allow for better mandible/plate alignment and other authors do not make use of locking screws, complicating the mandible adaption process. Screw types are also characterized by bi-cortical (secured through two cortical layers – front and back of the mandible) and mono-critical (secured through a single cortical layer at the front of the mandible). The number varies from 2 to 6

for the smaller plates such as the short plates and symphyseal plates, and 3 or more for larger plates such as the hemimandible.

The method of application for muscle forces, muscle force values, and the worst-case scenario for the mandible varies. Knoll, Gaida and Maurer (2006) apply vertical forces, only, as well as a bite force of 135 N. This bite force of 135 N is the maximum value measured in reconstruction patients who underwent mandible resection (Maurer, Pistner and Schubert, 2005). El-Anwar and Mohammed (2014) and Arbag, Korkmaz, Ozturk and Uyar, (2008) applied vertical loads of 150 N and 62.8 N, respectively. The former conducted two FEA studies where the force was applied at the lower incisors and the lower canines while the latter applied the force at the lower incisors. Wagner et al., (2002) and Feller et al. (2003) applied the forces as point loads. No information pertaining to the muscle directional vectors was provided. Both authors reported the forces at a percentage of the maximum values. The former did not consider the lateral pterygoid muscle. Al-Ahmari et al., (2015), Narra et al. (2014), Vajgel et. al (2013) and Wu, Lin, Liu and Lin (2017) apply the forces over an area of attachment, as well as providing the muscle force values in vector format. Wu, Lin, Liu and Lin, (2017) indicate that an incisal displacement of 5 mm causes the most tension at the mandibular condyles. No information about the area of attachment for each of the respective mandible muscles was provided.

Mandible bone material properties can change due to a wide variety of factors. The Young's modulus of cortical bone varies from 10 – 20 GPa and Young's modulus of trabecular bone varies from 0.76 – 20 GPa. Rho, Ashman and Turner (1993) tested several trabecular and cortical mandible samples using ultrasonic and microtensile testing. The Young's modulus values for ultrasonic testing of cortical and trabecular bone were different to those that underwent microtensile. Clearly indicating that testing methods affect material properties.

In mandible FEA literature the material properties vary significantly. Narra et al. (2014) and Vajgel et al. (2013) considered cortical bone as orthotropic and trabecular bone as isotropic. No information related to cortical bone volume/thickness vs. trabecular bone volume/thickness was reported, nor was any information provided that described the material properties at each data point on the mandible. Al-Ahmari et al. (2015), El-Anwar and Mohammed (2014) and Knoll, Gaida and Maurer (2006) considered both, trabecular and cortical bone to be isotropic. Cortical bone volume/thickness vs trabecular bone volume/thickness was not reported. Al-Ahmari et al. (2015) and El-Anwar and Mohammed (2014) reported Young's modulus for cortical bone as 13 700 MPa and 1 370 MPa for trabecular bone. Knoll, Gaida and Maurer (2006) reported Young's modulus of cortical bone as 8 700 MPa and 100 MPa for trabecular bone. Arbag et al. (2013) and Gutwald, Jaeger and Lambers (2016) assumed the mandible to be homogenous and isotropic.

FEA results for similar plate configurations differ due to the inconsistencies with boundary conditions, material properties, plate dimensions and mandible dimensions. There is also a lack of FEA result validation with hand calculations or physical testing, few (if any) references are made to mandible gender (M/F) in FEA. Another important part of mandible FEA is the modelling process for the CS reconstruction plate. As previously discussed, the CS plate is plasticly deformed causing cracks, weak points, and residual stress. Very little information is provided on the modelling of CS plates when compared to patient-specific plates. Physical testing of the implants does occur, but this is fracture and fatigue testing and few correlations to theoretical results are made. The FEA results shown in this study fall within the range of values reported in literature, despite the variability present therein.

# 6. Conclusions

Three project objectives were set at the beginning of this study. A parametric mandible reconstruction plate was developed using patient data, remaining stable for a range of mandible dimensions. This CAD model was used to generate three common plate configurations: hemimandible, symphyseal and lateral short plate. 74 total mandibles (37 male and 37 female) were measured and the corresponding plates generated and aligned. A total of 222 comparison tests were performed. Finally, an FEA study was performed on the male and female mandibles which exhibited the most curvature as a worst-case scenario. This chapter offers conclusions on the extent to which the initial project objectives have been fulfilled, recommendations to potentially refine the study and suggestions for future work are given.

- Create a stable, CAD parametric mandible reconstruction plate model. This template should use mandible measurements as parameters. This CAD model should be stable for a wide range of mandible measurements and features on the plate such as the number of holes and their positions should be easily adjustable.

- Investigate and refine the fit of the parametric reconstruction plate compared to a sample population of mandibles. These mandibles were generated using a SSM developed and validated in a previous study and the plates were generated using the CAD model.

- Investigate the structural strength of a pre-formed MRP in comparison with CS straight reconstruction plates. Identify common plate configurations present in literature, generate each configuration for the respective mandibles and attempt to compare the results to those in literature.

The extent to which these objectives were achieved is discussed in the following subsections.

## 6.1. Implant Design

The parametric mandible reconstruction plate was built in Autodesk Inventor. The template was constructed using cephalometric norms and data. This data describes the shape of the mandible using cephalometric landmarks, which are easily identifiable points on the mandible and skull. This parametric plate was generated with 15 holes on the body region, and 5 holes on each ramus region. Each hole can be removed or shifted depending on the surgical requirements. The holes on the ramus region belong to a rectangular patter and the number, as well as the spacing can be adjusted. This template was used to create every reconstruction plate used in this study, indicating that it is stable for a wide range of reasonable dimensions. It was deemed that this objective was satisfied. There are a number of advantages parametric mandible reconstruction plates have over individually customized plates. The parametric plate can be generated with 8 mandible measurements while the individually customized plate will require a much more in-depth design process. Due to the nature of the parametric plate all dimensions and accessories (fillets, screws) can be edited. This means that mandible anatomy such as nerves and the roots of the teeth can be accounted for by adjusting the holes accordingly.

## 6.2. Comparison Test

A comparison test to determine the parametric reconstruction plate fit was performed. 37 male and 37 random mandibles were generated using a SSM developed in a previous study. The corresponding parametric plate configurations (hemimandible, symphyseal and lateral short) were generated and exported in .STL format. The mandibles and plates were imported into *MeshLab* and aligned using the point-based glueing method. Hausdorff distances were measured between the plate and the mandible. The minimum, maximum, mean and RMS distances were recorded for each plate configuration/mandible pair. Certain regions on the mandible create interference that needs to be accounted for. In future these regions needs to be carefully considered when measuring the mandibles. However, the results indicate adequate mandible geometry approximation and this objective was satisfied.

## 6.3. FEA Study

A FEA study was performed on the male and female mandible that had the most curvature. These models were chosen as the worst-case scenario due to the fact that the corresponding plates would undergo more bending, creating higher residual stresses. The hemimandible, symphyseal and lateral short plate configurations were edited in Autodesk Inventor. The holes were removed and shifted, corners were rounded, and fillets were added so that surrounding tissue would not be damaged. The plates were aligned and imported into ANSYS. The screws were simulated as 4 mm cylinders. Boundary conditions were applied, and a mesh independence study was performed on each configuration to determine if the solution converges, as incorrectly applied boundary conditions or meshes will not converge to a single value. The moment and force reaction results measured in ANSYS were validated with hand calculations. The results agree with the observable trends in literature and thus, this objective was satisfied.

## 6.4. Recommendations and Future Work

The results show in this study are promising, however, some recommendations are necessary to further improve the quality of the parametric implant and its performance.

1. **Spline Improvement:** As stated in Chapter 3, improvement of the spline construction in the CAD template could alleviate the interference near the mandibular angle. Another landmark could create a curve that more closely matches the mandible geometry. This could ease the plate generation process, removing unnecessary edits.
2. **Increase Sample Size:** The comparison results are promising but before physical testing should occur an increase in comparison sample size could provide more information on the plate fit. Especially if this comparison test is undertaken after the CAD template has been improved with alternative landmarks.
3. **Physical Testing :** Before this implant can be used in a medical setting the comparison and FEA results will need to be confirmed with physical testing. Calcium Sulphate mandible models and PLA parametric plates can be printed and serve as the initial, cost efficient comparison test. The final step would be to obtain mandible cadavers under ethical clearance and attempt

to fit titanium plates. Once fitted, these models should undergo loading, using the same setup as the FEA study, in order to confirm the FEA results.

Future work should not be to develop more efficient, accurate implants but the focus should be on the development of a widely accepted, one-size-fits-all mandible FEA modelling procedure. Physical testing, theoretical result validation by hand calculations or literature comparison is essential to confirm the results. All boundary condition values should be provided, especially mandible material properties and serious emphasis should be placed on the modelling procedure of the plastic deformation and bending process of commercial straight reconstruction plates. Correlations between plate thickness vs. resection length, plate length vs. resection length and number of holes vs. resection length should be investigated and established as these values are also inconsistent across literature. The variability of mandible FEA modelling should be investigated, and a standard simulation procedure developed.

The objective of this study was to develop a novel, mandible reconstruction plate that accepts patient parameters as input data and produces an accurate, acceptable approximation of the required implant and mandible shape. A FEA study was performed to determine if the pre-formed implant experiences lower stress values than the CS implant. The Hausdorff distance results were acceptable, and it is concluded that this novel reconstruction plate provides a suitable approximation of mandible geometry, while reducing the bending that is common in commercial straight reconstruction plates. FEA results indicate that the parametric reconstruction plate experiences lower stress values when compared with the commercial straight plates throughout all the plate configurations and mandible genders. It is therefore concluded that this novel mandible implant successfully accounts for the limitations which exist in commercial straight implants.

# List of References

Abbey, T. (2017). *Dealing with Stress Concentration and Singularities*. [online] Digital Engineering. Available at: https://www.digitalengineering247.com/article/dealing-stress-concentrations-singularities [Accessed 20 Oct. 2020].

Abdolali, F., Zoroofi, R.A., Abdolali, M., Yokota, F., Otake, Y. and Sato, Y. (2017). Automatic segmentation of mandibular canal in cone beam CT images using conditional statistical shape model and fast marching. *International journal of computer assisted radiology and surgery*, vol. 12, no. 4, pp. 581–593.

(ACR), R. (2019). *Nuclear Medicine, General*. [online] Radiologyinfo.org. Available at: https://www.radiologyinfo.org/en/info.cfm?pg=gennuclear [Accessed 10 Jun. 2019].

Ackland, D., Robinson, D., Redhead, M., Lee, P., Moskaljuk, A. and Dimitroulis, G., 2017. A personalized 3D-printed prosthetic joint replacement for the human temporomandibular joint: From implant design to implantation. *Journal of the Mechanical Behavior of Biomedical Materials*, 69, pp.404-411.

Al-Ahmari, A., Nasr, E., Moiduddin, K., Anwar, S., Kindi, M. and Kamrani, A., 2015. A comparative study on the customized design of mandibular reconstruction plates using finite element method. *Advances in Mechanical Engineering*, 7(7), p.168781401559389.

Allard, F. and Ashman, R., 1991. A comparison between cancellous bone compressive moduli determined from surfaced strain and total specimen deflection. *Transactions of the Orthopedic Society*, 16(151).

Anderson, D., 1956. Measurement of Stress in Mastication. I. *Journal of Dental Research*, 35(5), pp.664-670.

Andersen, K., Pedersen, E. and Melsen, B., 1991. Material parameters and stress profiles within the periodontal ligament. *American Journal of Orthodontics and Dentofacial Orthopedics*, 99(5), pp.427-440.

Aquilina, P., Chamoli, U., Parr, W., Clausen, P. and Wroe, S., 2013. Finite element analysis of three patterns of internal fixation of fractures of the mandibular condyle. *British Journal of Oral and Maxillofacial Surgery*, 51(4), pp.326-331.

Arce, K., Bell, R., Potter, J., Buehler, M., Potter, B. and Dierks, E. (2012). Vascularized free tissue transfer for reconstruction of ablative defects in oral and oropharyngeal cancer patients undergoing salvage surgery following concomitant chemoradiation. *International Journal of Oral and Maxillofacial Surgery*, 41(6), pp.733-738.

Arbag, H., Korkmaz, H., Ozturk, K. and Uyar, Y., 2008. Comparative Evaluation of Different Miniplates for Internal Fixation of Mandible Fractures Using Finite Element Analysis. *Journal of Oral and Maxillofacial Surgery*, 66(6), pp.1225-1232.

Barral, J. and Croibier, A. (2009). *Manual therapy for the cranial nerves*. Edinburgh: Elsevier, pp.139-146.

Bertl, K., Subotic, M., Heimel, P., Schwarze, U., Tangl, S. and Ulm, C., 2014. Morphometric characteristics of cortical and trabecular bone in atrophic edentulous mandibles. *Clinical Oral Implants Research*, 26(7), pp.780-787.

Bialek, E., Zajkowski, P. and Jakubowski, W. (2003). Ultrasonography as the first method of detection of mandible lesions. *Ultrasound in Medicine & Biology*, 29(5), pp.S140-S141.

Biglioli, F., Frigerio, A., Colombo, V., Colletti, G., Rabbiosi, D., Mortini, P., Dalla Toffola, E., Lozza, A. and Brusati, R. (2012). Masseteric–facial nerve anastomosis for early facial reanimation. *Journal of Cranio-Maxillofacial Surgery*, 40(2), pp.149-155.

Breeland, G. and Patel, B. (2019). *Anatomy, Head and Neck, Mandible*. [online] Ncbi.nlm.nih.gov. Available at: https://www.ncbi.nlm.nih.gov/books/NBK532292/ [Accessed 22 Jul. 2019].

Bohr, C. and Shermetaro, C. (2019). *Anatomy, Head and Neck, Temporoparietal Fascia*. [online] Ncbi.nlm.nih.gov. Available at: https://www.ncbi.nlm.nih.gov/books/NBK507912/ [Accessed 27 Jun. 2019].

Bose, S., Roy, M. and Bandyopadhyay, A. (2012). Recent advances in bone tissue engineering scaffolds. *Trends in Biotechnology*, 30(10), pp.546-554.

Bujtár, P., Simonovics, J., Váradi, K., Sándor, G. and Avery, C., 2014. The biomechanical aspects of reconstruction for segmental defects of the mandible: A finite element study to assess the optimisation of plate and screw factors. *Journal of Cranio-Maxillofacial Surgery*, 42(6), pp.855-862.

Cancer.org. (2019). *Imaging (Radiology) Tests for Cancer*. [online] Available at: https://www.cancer.org/treatment/understanding-your-diagnosis/tests/imaging-radiology-tests-for-cancer.html [Accessed 10 Jun. 2019].

Carlson, D. and Ribbens, K. (1985). *Developmental Aspects of Temporomandibular Joint Disorders (Craniofacial Growth)*. University of Michigan, pp.19-35.

Carpentier, P., Yung, J., Marguelles-Bonnet, R. and Meunissier, M. (1988). Insertions of the lateral pterygoid muscle: An anatomic study of the human temporomandibular joint. *Journal of Oral and Maxillofacial Surgery*, 46(6), pp.477-482.

Chen, S., Chen, H., Horng, S., Tai, H., Hsieh, J., Yeong, E., Cheng, N., Hsieh, T., Chien, H. and Tang, Y. (2014). Reconstruction for Osteoradionecrosis of the Mandible. *Annals of Plastic Surgery*, p.1.

Chi, A., Magliocca, K., Martinez, A., Morrison, A. and Pernick, N. (2019). *Mandible & maxilla*. [online] Pathologyoutlines.com. Available at: https://www.pathologyoutlines.com/mandiblemaxilla.html [Accessed 13 Jun. 2019].

Coletti, D., Ord, R. and Liu, X., 2009. Mandibular reconstruction and second-generation locking reconstruction plates: Outcome of 110 patients. *International Journal of Oral and Maxillofacial Surgery*, 38(9), pp.960-963.

Collins, C., Pirinjian-Leonard, G., Tolas, A. and Alcalde, R., 2004. A prospective randomized clinical trial comparing 2.0-mm locking plates to 2.0-mm standard plates in treatment of mandible fractures. *Journal of Oral and Maxillofacial Surgery*, 62(11), pp.1392-1395.

Comsol.com. 2020. *Detailed Explanation Of The Finite Element Method (FEM)*. [online] Available at: <https://www.comsol.com/multiphysics/finite-element-method> [Accessed 20 May 2020].

Cootes, T., Baldock, E. and Graham, J. (2000). An introduction to active shape models. *Image processing and analysis*, pp. 223–248.

Daegling, D. and Hylander, W., 2000. Experimental observation, theoretical models, and biomechanical inference in the study of mandibular form. *American Journal of Physical Anthropology*, 112(4), pp.541-551.

Damron, T. (2014). *Chondroblastoma: Background, Pathophysiology, Etiology*. [online] Emedicine.medscape.com. Available at: https://emedicine.medscape.com/article/1254949-overview [Accessed 11 Jun. 2019].

Darkwah, W., Kadri, A., Adormaa, B. and Aidoo, G. (2018). Cephalometric study of the relationship between facial morphology and ethnicity: Review article. *Translational Research in Anatomy*, 12, pp.20-24.

Dashnyam, K., Lee, J., Mandakhbayar, N., Jin, G., Lee, H. and Kim, H. (2018). Intra-articular biomaterials-assisted delivery to treat temporomandibular joint disorders. *Journal of Tissue Engineering*, 9, p.204173141877651.

Davidson, J., Metzinger, S., Tufaro, A. and Dellon, A. (2003). Clinical Implications of the Innervation of the Temporomandibular Joint. *Journal of Craniofacial Surgery*, 14(2), pp.235-239.

Dittmer, J., Jensen, C., Gottschalk, M. and Almy, T., 2006. Mesh Optimization Using a Genetic Algorithm to Control Mesh Creation Parameters. *Computer-Aided Design and Applications*, 3(6), pp.731-740.

Dubrul, E. (1988). *Sicher and Dubrul's Oral Anatomy*. 8th ed. Ishiyaku Euroamerica, pp.87-99.

Dumont, E., Piccirillo, J. and Grosse, I., 2005. Finite-element analysis of biting behavior and bone stress in the facial skeletons of bats. *The Anatomical Record Part A: Discoveries in Molecular, Cellular, and Evolutionary Biology*, 283A(2), pp.319-330.

Earth's Lab. (2019). *Maxillary Tuberosity (Tuberosity of Maxilla) – Earth's Lab*. [online] Available at: https://www.earthslab.com/anatomy/maxillary-tuberosity-tuberosity-of-maxilla/ [Accessed 2 Jul. 2019].

El-Anwar, M. and Mohammed, M., 2014. Comparison between two low profile attachments for implant mandibular overdentures. *Journal of Genetic Engineering and Biotechnology*, 12(1), pp.45-53.

Emes, Y., Aybar, B. and Dergin, G., 2018. *Temporomandibular Joint Pathology*. p.185.

Ettl, T., Driemel, O., Dresp, B., Reichert, T., Reuther, J. and Pistner, H., 2010. Feasibility of alloplastic mandibular reconstruction in patients following removal of oral squamous cell carcinoma. *Journal of Cranio-Maxillofacial Surgery*, 38(5), pp.350-354.

Feller, K., Schneider, M., Hlawitschka, M., Pfeifer, G., Lauer, G. and Eckelt, U., 2003. Analysis of complications in fractures of the mandibular angle—a study with finite element computation and evaluation of data of 277 patients. *Journal of Cranio-Maxillofacial Surgery*, 31(5), pp.290-295.

Garcia, C. (1975). Cephalometric evaluation of Mexican Americans using the Downs and Steiner analyses. *American Journal of Orthodontics*, 68(1), pp.67-74.

Gaillard, F. (2019). *Pterygoid muscles - illustration | Radiology Case | Radiopaedia.org*. [online] Radiopaedia.org. Available at: https://radiopaedia.org/cases/pterygoid-muscles-illustration [Accessed 2 Jul. 2019].

Gatterman, M. (2012). *Whiplash*. St. Louis: Elsevier Mosby, pp.85-119.

George, S. and Saravana Kumar, G. (2013). Patient specific parametric geometric modelling and finite element analysis of cementless hip prosthesis. *Virtual and Physical Prototyping*, 8(1), pp.65-83.

Giavarina, D. (2015). Understanding Bland Altman Analysis. *Biochemia Medica* vol. 25(2), pp 141-151.

Gibbs, C., Mahan, P., Wilkinson, T. and Mauderli, A. (1984). EMG activity of the superior belly of the lateral pterygoid muscle in relation to other jaw muscles. *The Journal of Prosthetic Dentistry*, 51(5), pp.691-702.

Ghassemi, T., Shahroodi, A., Ebrahimzadeh, M., Mousavian, A., Movaffagh, J. and Moradi, A. (2018). Current Concepts in Scaffolding for Bone Tissue Engineering. *The Archive of Bone and Joint Surgery*, 6(2), pp.90-99.

Gribel, B., Gribel, M., Frazão, D., McNamara, J. and Manzi, F. (2011). Accuracy and reliability of craniometric measurements on lateral cephalometry and 3D measurements on CBCT scans. *The Angle Orthodontist*, 81(1), pp.26-35.

Guruprasad, Y., Shetty, J., Prabhakar, C. and Hemavathy, O., 2011. Efficacy of 2-mm locking miniplates in the management of .1-8.

Hsiao, T., Chang, H. and Liu, K. (1996). Sex Determination by Discriminant Function Analysis of Lateral Radiographic Cephalometry. *Journal of Forensic Sciences*, 41(5), p.13999J.

Hylander, W. (1984). Stress and strain in the mandibular symphysis of primates: A test of competing hypotheses. *American Journal of Physical Anthropology*, 64(1), pp.1-46.

Honee, G. (1972). The anatomy of the lateral pterygoid muscle. *Acta Morphol Neerl Scand*, 10(4), pp.331-340.

Hurmerinta, K., Rahkamo, A. and Haavikko, K. (1997). Comparison between cephalometric classification methods for sagittal jaw relationships. *European Journal of Oral Sciences*, 105(3), pp.221-227.

Hylander, William. (2006). Functional anatomy and biomechanics of the masticatory apparatus. Temporomandibular Disorders: An Evidenced Approach to Diagnosis and Treatment. 1-34.

Kenhub.(2019). *Pterygoidmuscles*.[online]Availableat:https://www.kenhub.com/en/library/anatomy/pterygoid-muscles [Accessed 2 Jul. 2019].

Klineberg, I. and Eckert, S. (2016). *Functional Occlusion in Restorative Dentistry and Prosthodontics*. Elsevier Mosby, pp.173-187.

Koolstra, J., Naeije, M. and Van Eijden, T. (2001). The Three-dimensional Active Envelope of Jaw Border Movement and its Determinants. *Journal of Dental Research*, 80(10), pp.1908-1912.

Knoll, W., Gaida, A. and Maurer, P., 2006. Analysis of mechanical stress in reconstruction plates for bridging mandibular angle defects. *Journal of Cranio-Maxillofacial Surgery*, 34(4), pp.201-209.

Korioth, T., Romilly, D. and Hannam, A., 1992. Three-dimensional finite element stress analysis of the dentate human mandible. *American Journal of Physical Anthropology*, 88(1), pp.69-96.

Koen, E. (2013). *Skull - Right lateral View by Emily Sylvia Koehn*. [online] Thinglink.com. Available at: https://www.thinglink.com/scene/406468365398310914 [Accessed 3 Jul. 2019].

Kumar, B., Venkatesh, V., Kumar, K., Yadav, B. and Mohan, S. (2015). Mandibular Reconstruction: Overview. *Journal of Maxillofacial and Oral Surgery*, 15(4), pp.425-441.

Jacobs, P. (1984). Limb Salvage and Rotationplasty for Osteosarcoma in Children. *Clinical Orthopaedics and Related Research*, (188).

Jaffe, N., Bruland, Ø. and Bielack, S. (2009). *Pediatric and adolescent osteosarcoma*. New York: Springer, pp.3-13.

Jones, R. and Dillon, J. (2016). Nonodontogenic Cysts of the Jaws and Treatment in the Pediatric Population. *Oral and Maxillofacial Surgery Clinics of North America*, 28(1), pp.31-44.

Jnjmedicaldevices.com. 2020. Synthes Matrixmandible™ | Plating System | J&J Medical Devices. [online] Available at: <https://www.jnjmedicaldevices.com/en-US/product/matrixmandibletm-preformed-reconstruction-plates> [Accessed 11 June 2020].

Katsuragi, Y., Kayano, S., Akazawa, S., Nagamatsu, S., Koizumi, T., Matsui, T., Onitsuka, T., Yurikusa, T., Huang, W.-C. and Nakagawa, M. (2011). Mandible reconstruction using the calcium-sulphate three-dimensional model and rubber stick: A new method, 'mould technique', for more accurate, efficient and simplified fabrication. *Journal of Plastic, Reconstructive & Aesthetic Surgery*, 64(5), pp.614–622.

Kryger, M., Roth, T., Powell, N. and Riley, R. (2011). *Principles and practice of sleep medicine*. 5th ed. p.Chapter 108.

Lam, D. and Carlson, E. (2014). The Temporalis Muscle Flap and Temporoparietal Fascial Flap. *Oral and Maxillofacial Surgery Clinics of North America*, 26(3), pp.359-369.

Li, P., Shen, L., Li, J., Liang, R., Tian, W. and Tang, W., 2014. Optimal design of an individual endoprosthesis for the reconstruction of extensive mandibular defects with finite element analysis. *Journal of Cranio-Maxillofacial Surgery*, 42(1), pp.73-78.

Linde, F., Hvid, I. and Pongsoipetch, B., 1989. Energy absorptive properties of human trabecular bone specimens during axial compression. *Journal of Orthopaedic Research*, 7(3), pp.432-439.

Loya-Solis, A., González-Colunga, K., Pérez-Rodríguez, C., Ramírez-Ochoa, N., Ceceñas-Falcón, L. and Barboza-Quintana, O. (2015). Ameloblastic Fibrosarcoma of the Mandible: A Case Report and Brief Review of the Literature. *Case Reports in Pathology*, 2015, pp.1-5.

Ludlow, J., Gubler, M., Cevidanes, L. and Mol, A. (2009). Precision of cephalometric landmark identification: Cone-beam computed tomography vs conventional cephalometric views. *American Journal of Orthodontics and Dentofacial Orthopedics*, 136(3), pp.312.e1-312.e10.

Magliocca, K. and Martinez, A. (2019). *Benign tumors / tumor-like conditions: ameloblastoma*. [online] Pathologyoutlines.com. Available at: https://www.pathologyoutlines.com/topic/mandiblemaxillaameloblastoma.html [Accessed 13 Jun. 2019].

Magliocca, K. and Martinez, A. (2019). *Malignant tumors: ameloblastic fibrosarcoma*. [online] Available at: https://www.pathologyoutlines.com/topic/mandiblemaxillaameloblasticfibrosarcoma.html [Accessed 13 Jun. 2019].

Magliocca, K. and Morrison, A. (2019). *Odontogenic cysts: dentigerous*. [online] Pathologyoutlines.com. Available at: https://www.pathologyoutlines.com/topic/mandiblemaxilladentigerous.html [Accessed 11 Jun. 2019].

Manikkam, S., Masthan, K., Anitha, N. and Krupaa, J. (2015). Ameloblastoma. *Journal of Pharmacy and Bioallied Sciences*, 7(5), p.169.

Martinez, A. and Magliocca, K. (2019). *Fissural and other nonodontogenic cysts: General*. [online] Pathologyoutlines.com. Available at: https://www.pathologyoutlines.com/topic/mandiblemaxillafissuralgeneral.html [Accessed 11 Jun. 2019].

Martinez, A. and Magliocca, K. (2019). *Malignant tumors: osteosarcoma*. [online] Pathologyoutlines.com.

Mast, H., Haller, J. and Solomon, M. (1992). Benign lesions of the mandibular and maxillary region in children: Characterization by CT and MRI. *Computerized Medical Imaging and Graphics*, 16(1), pp.1-9.

Matic, D. and Yoo, J. (2019). *Facial nerve paralysis - Reduction & Fixation - Temporalis muscle (antidromic) mini-sling - Irreversible paralysis, midface, and mouth - AO Surgery Reference*. [online] Www2.aofoundation.org.

Maurer, P., Pistner, H. and Schubert, J. (2005). Computergestützte Kaukraftanalyse bei Patienten mit Unterkieferkontinuitätsresektionen. *Mund-, Kiefer- und Gesichtschirurgie*, 10(1), pp.37–41.

Mayo Clinic. (2019). *Bone cancer - Symptoms and causes*. [online] Available at: https://www.mayoclinic.org/diseases-conditions/bone-cancer/symptoms-causes/syc-20350217 [Accessed 22 Jul. 2019].

(2019). *CT scan - Mayo Clinic*. [online] Available at: https://www.mayoclinic.org/tests-procedures/ct-scan/about/pac-20393675 [Accessed 10 Jun. 2019].

Mayoclinic.org. (2019). *X-ray: Imaging test quickly helps diagnosis - Mayo Clinic*. [online] Available at: https://www.mayoclinic.org/tests-procedures/x-ray/about/pac-20395303 [Accessed 10 Jun. 2019].

McNeill, C. (1997). *Science and practice of occlusion*. Chicago: Quintessence Publishing Co, pp.115-124.

Med-college.de. (2019). *Non-Odontogenic Jaw Cysts*. [online] Available at: http://www.med-college.de/en/wiki/artikel.php?id=485 [Accessed 11 Jun. 2019].

Meyenberg, K., Kubik, S. and Palla, S. (1986). Relationships of the muscles of mastication to the articular disc of the temporomandibular joint. *Swiss Dental Journal*, 96(6), pp.815-834.

Mohammed, M., P. Fitzpatrick, A. and Gibson, I. (2017). Customised design of a patient specific 3D printed whole mandible implant. KnE Engineering, 2(2), p.104.

Moorrees, C. and Kean, M. (1958). Natural head position, a basic consideration in the interpretation of cephalometric radiographs. American Journal of Physical Anthropology, 16(2), pp.213-234.

Morrison, A. (2019). *Odontogenic cysts: calcifying odontogenic cyst*. [online] Pathologyoutlines.com. Available at: http://www.pathologyoutlines.com/topic/mandiblemaxillacalcifyingodontogenic.html [Accessed 11 Jun. 2019].

Morrison, A. (2019). *Odontogenic cysts: general*. [online] Pathologyoutlines.com. Available at: https://www.pathologyoutlines.com/topic/mandiblemaxillaodontogeniccyst.html [Accessed 11 Jun. 2019].

Morrison, A. (2019). *Odontogenic cysts: residual cyst*. [online] Pathologyoutlines.com. Available at: http://www.pathologyoutlines.com/topic/mandiblemaxillaresidualcyst.html [Accessed 11 Jun. 2019].

Morrison, A. (2019). *Osteomyelitis: general*. [online] Pathologyoutlines.com. Available at: https://www.pathologyoutlines.com/topic/mandiblemaxillaosteomyelitis.html [Accessed 11 Jun. 2019].

Motosugi, U., Ogawa, I., Yoda, T., Abe, T., Sugasawa, M., Murata, S., Yasuda, M., Sakurai, T., Shimizu, Y. and Shimizu, M. (2009). Ghost cell odontogenic carcinoma arising in calcifying odontogenic cyst. *Annals of Diagnostic Pathology*, 13(6), pp.394-397.

Moshiri, M., Scarfe, W., Hilgers, M., Scheetz, J., Silveira, A. and Farman, A. (2007). Accuracy of linear measurements from imaging plate and lateral cephalometric images derived from cone-beam computed tomography. *American Journal of Orthodontics and Dentofacial Orthopedics*, 132(4), pp.550-560.

Murphy, C., Haugh, M. and O'Brien, F. (2010). The effect of mean pore size on cell attachment, proliferation and migration in collagen–glycosaminoglycan scaffolds for bone tissue engineering. *Biomaterials*, 31(3), pp.461-466.

Murugan, J., Kurian, T., Jayaprakash, J. and Sreedharapanickar, S., 2015. 3-D Analysis of Flanged Joints Through Various Preload Methods Using ANSYS. *Journal of The Institution of Engineers (India): Series C*, 96(4), pp.407-417.

Nagasao, T., Miyamoto, J., Tamaki, T. and Kawana, H., 2010. A comparison of stresses in implantation for grafted and plate-and-screw mandible reconstruction. Oral Surgery, Oral Medicine, Oral Pathology, Oral Radiology, and Endodontology, 109(3), pp.346-356.

Narra, N., Valášek, J., Hannula, M., Marcián, P., Sándor, G., Hyttinen, J. and Wolff, J., 2014. Finite element analysis of customized reconstruction plates for mandibular continuity defect therapy. *Journal of Biomechanics*, 47(1), pp.264-268.

Nccn.org. 2020. *Understanding the Effects Of Cancer Treatment On Bone Health*. [online] Available at: <https://www.nccn.org/patients/resources/life_with_cancer/treatment/bone_health.aspx> [Accessed 15 April 2020].

nhs.uk. (2019). *MRI scan*. [online] Available at: https://www.nhs.uk/conditions/mri-scan/ [Accessed 10 Jun. 2019].

Nomura, T., Gold, E., Powers, M., Shingaki, S. and Katz, J., 2003. Micromechanics/structure relationships in the human mandible. *Dental Materials*, 19(3), pp.167-173.

Odin, G., Savoldelli, C., Bouchard, P. and Tillier, Y., 2010. Determination of Young's modulus of mandibular bone using inverse analysis. *Medical Engineering & Physics*, 32(6), pp.630-637.

Oguz, Y., Uckan, S., Ozden, A., Uckan, E. and Eser, A., 2009. Stability of locking and conventional 2.0-mm miniplate/screw systems after sagittal split ramus osteotomy: finite element analysis. *Oral Surgery, Oral Medicine, Oral Pathology, Oral Radiology, and Endodontology*, 108(2), pp.174-177.

Olszta, M., Cheng, X., Jee, S., Kumar, R., Kim, Y., Kaufman, M., Douglas, E. and Gower, L. (2007). Bone structure and formation: A new perspective. *Materials Science and Engineering: R: Reports*, 58(3-5), pp.77-116.

Ortho Baltic Implants. (n.d.). *Patient-specific Medical Devices | Baltic Implants*. [online] Available at: http://balticimplants.eu/patient-specific-medical-devices/ [Accessed 17 Nov. 2020].

Orthopaedicsone.com.(2019). *Temporomandibular-ligament*.[online]-Available: https://www.orthopaedicsone.com/display/Main/Temporomandibular+ligament [Accessed 3 Jul. 2019].

O'Toole, B., Karpanan, K., Feghhi, M. 2006. 'Experimental and Finite Element Analysis of Preloaded Bolted Joints Under Impact Loading.' 47th AIAA/ASE/ASCE/AHS/ASC Structures, Structural Dynamics, and Materials Conference. 01 – 04 May. Rhode Island.

Pandit, N., Pandit, I., Malik, R., Bali, D. and Jindal, S. (2012). Autogenous bone block in the treatment of teeth with hopeless prognosis. *Contemporary Clinical Dentistry*, 3(4), p.437.

Pernick, N. (2019). *Benign tumors / tumor-like conditions: adenomatoid odontogenic tumor*. [online] Pathologyoutlines.com.

Petrova, R., Wong, R., Loh, J. and Islam, I. (2016). *Perusal of the Finite Element Method*. Croatia: InTech, pp.191-213.

Ponnam, S., Srivastava, G. and Smitha, B. (2012). Ameloblastic fibroma. *Journal of Oral and Maxillofacial Pathology*, 16(3), p.444.

Predoctoral Orthodontic Laboratory Manual. (2008). New Jersey: Department of Undergraduate Orthodontics, New Jersey Dental School.

Proffit, W., Fields, H., Larson, B. and Sarver, D. (1986). *Contemporary orthodontics*. 3rd ed.

Raith, S., Wolff, S., Steiner, T., Modabber, A., Weber, M., Hölzle, F. and Fischer, H. (2016). Planning of mandibular reconstructions based on statistical shape models. *International Journal of Computer Assisted Radiology and Surgery*, 12(1), pp.99-112.

Rcpath.org. (2019). *What is pathology?* [online] Available at: https://www.rcpath.org/discover-pathology/what-is-pathology.html [Accessed 10 Jun. 2019].

Reilly, D. and Burstein, A. (1975). The elastic and ultimate properties of compact bone tissue. *Journal of Biomechanics*, 8(6), pp.393-405.

Resnik, R. and Misch, C. (2017). *Misch's avoiding complications in oral implantology*. 1st ed. Elsevier, pp.294-329.

Richmond, B., Wright, B., Grosse, I., Dechow, P., Ross, C., Spencer, M. and Strait, D., 2005. Finite element analysis in functional morphology. *The Anatomical Record Part A: Discoveries in Molecular, Cellular, and Evolutionary Biology*, 283A(2), pp.259-274.

Ricketts, R. (1960). A foundation for cephalometric communication. *American Journal of Orthodontics*, 46(5), pp.330-357.

Rho, J., Ashman, R. and Turner, C. (1993). Young's modulus of trabecular and cortical bone material: Ultrasonic and microtensile measurements. *Journal of Biomechanics*, 26(2), pp.111-119.

Ross, C., Patel, B., Slice, D., Strait, D., Dechow, P., Richmond, B. and Spencer, M., 2005. Modeling masticatory muscle force in finite element analysis: Sensitivity analysis using principal coordinates analysis. *The Anatomical Record Part A: Discoveries in Molecular, Cellular, and Evolutionary Biology*, 283A(2), pp.288-299.

Rothschild, B. (2019). *Calcium Pyrophosphate Deposition Disease: Practice Essentials, Etiology, Epidemiology*. [online] Emedicine.medscape.com. Available at: https://emedicine.medscape.com/article/330936-overview [Accessed 11 Jun. 2019].

Rouwkema, J., Rivron, N. and van Blitterswijk, C. (2008). Vascularization in tissue engineering. *Trends in Biotechnology*, 26(8), pp.434-441.

Toman, H., Nasir, A., Hassan, R. and Hassan, R. (2011). Skeletal, dentoalveolar, and soft tissue cephalometric measurements of Malay transfusion-dependent thalassaemia patients. *The European Journal of Orthodontics*, 33(6), pp.700-704.

Turcotte, R., Kurt, A., Sim, F., Krishnan Unni, K. and McLeod, R. (1993). Chondroblastoma. *Human Pathology*, 24(9), pp.944-949.

Salguiero, M. and Stevens, M. (2010). Experience with the Use of Prebent Plates for the Reconstruction of Mandibular Defects. *Craniomaxillofacial Trauma Reconstruction* vol. 3(4), pp. 201-208.

Sakkas, A., Wilde, F., Heufelder, M., Winter, K. and Schramm, A. (2017). Autogenous bone grafts in oral implantology—is it still a "gold standard"? A consecutive review of 279 patients with 456 clinical procedures. *International Journal of Implant Dentistry*, 3(1).

Sava, A. and Scutariu, M. (2012). Functional anatomy of the temporomandibular joint. *Rev Med Chir Soc Med Nat Iasi*, 116(3), pp.902-906.

Schepers, R., Raghoebar, G., Vissink, A., Stenekes, M., Kraeima, J., Roodenburg, J., Reintsema, H. and Witjes, M., 2015. Accuracy of fibula reconstruction using patient-specific CAD/CAM reconstruction plates and dental implants: A new modality for functional reconstruction of mandibular defects. *Journal of Cranio-Maxillofacial Surgery*, 43(5), pp.649-657.

Schwartz, L. (1959). *Disorders of the Temporomandibular Joint. Diagnosis, management, relation to occlusion of teeth. By L. Schwartz ... and eighteen contributors. (Illustrated by Robert J. Demarest.)*. Saunders (W.B.) co Ltd.

Shibahara, T., Noma, H., Furuya, Y. and Takaki, R., 2002. Fracture of mandibular reconstruction plates used after tumor resection. *Journal of Oral and Maxillofacial Surgery*, 60(2), pp.182-185.

Sphweb.bumc.bu.edu. (2020). *Central Limit Theorem*. [online] Available at: https://sphweb.bumc.bu.edu/otlt/mphmodules/bs/bs704_probability/BS704_Probability12.html#:~:text=The%20central%20limit%20theorem%20states,will%20be%20approximately%20normally%20distributed

Stevens, J. and Ray, R., 1962. An Experimental Comparison of Living and Dead Bone in Rats. I. Physical Properties. *The Journal of Bone and Joint Surgery. British volume*, 44-B(2), pp.412-423.

Surveysystem.com. (2012). Sample Size Calculator - Confidence Level, Confidence Interval, Sample Size, Population Size, Relevant Population - Creative Research Systems. [online] Available at: https://www.surveysystem.com/sscalc.htm.

Tate, G., Ellis, E. and Throckmorton, G., 1994. Bite forces in patients treated for mandibular angle fractures: Implications for fixation recommendations. *Journal of Oral and Maxillofacial Surgery*, 52(7), pp.734-736.

Thompson, M. and Thompson, J., 2017. *ANSYS Mechanical APDL For Finite Element Analysis*. pp.181-199.

Turner, C., Cowin, S., Rho, J., Ashman, R. and Rice, J. (1990). The fabric dependence of the orthotropic elastic constants of cancellous bone. *Journal of Biomechanics*, 23(6), pp.549-561.

Vajgel, A., Camargo, I., Willmersdorf, R., de Melo, T., Filho, J. and de Holanda Vasconcellos, R., 2013. Comparative Finite Element Analysis of the Biomechanical Stability of 2.0 Fixation Plates in Atrophic Mandibular Fractures. *Journal of Oral and Maxillofacial Surgery*, 71(2), pp.335-342.

Van Eijden, T. (1990). Jaw Muscle Activity in Relation to the Direction and Point of Application of Bite Force. *Journal of Dental Research*, 69(3), pp.901-905.

Van Eijden, T., 1991. Three-dimensional analyses of human bite-force magnitude and moment. *Archives of Oral Biology*, 36(7), pp.535-539.

Van Eijden, T. (2000). Biomechanics of the Mandible. *Critical Reviews in Oral Biology & Medicine*, 11(1), pp.123-136.

van Zyl, O. and Fagan, J. (2017). [online] Vula.uct.ac.za. Available at: https://vula.uct.ac.za/access/content/group/ba5fb1bd-be95-48e5-81be-586fbaeba29d/Vascularised%20free%20fibula%20flap%20_FFF_%20in%20head%20and%20neck%20reconstruction.pdf [Accessed 8 Jul. 2019].

Wagner, A., Krach, W., Schicho, K., Undt, G., Ploder, O. and Ewers, R., 2002. A 3-dimensional finite-element analysis investigating the biomechanical behavior of the mandible and plate osteosynthesis in cases of fractures of the condylar process. *Oral Surgery, Oral Medicine, Oral Pathology, Oral Radiology, and Endodontology*, 94(6), pp.678-686.

Walia, M., Arora, N., Rathee, M. and Arora, S. (2014). Temporomandibular Joint (TMJ): A Weight Bearing Joint?. *Indian J Stomnatol*, 5(1), pp.22-24.

Wang, C. (2005). Parameterization and parametric design of mannequins. *Computer-Aided Design*, 37(1), pp.83-98.

Washmuth, D. (2019). *Masseter Muscle: Definition, Innervation & Function | Study.com*. [online] Study.com. Available at: https://study.com/academy/lesson/masseter-muscle-definition-innervation-function.html [Accessed 24 Jun. 2019].

Watanabe, S., Nakajima, K., Mizokami, A., Yaegashi, H., Noguchi, N., Kawashiri, S., Inokuchi, M. and Kinuya, S. (2016). Bone scan index of the jaw: a new approach for evaluating early-stage anti-resorptive agents-related osteonecrosis. *Annals of Nuclear Medicine*, 31(3), pp.201-210.

Werner, M. (2006). Giant cell tumor of bone: morphological, biological and histogenetical aspects. *International Orthopaedics*, 30(6), pp.484-489.

Williams, D. (2008). On the mechanisms of biocompatibility. *Biomaterials*, 29(20), pp.2941-2953.

Wong, R., Tideman, H., Merkx, M., Jansen, J. and Goh, S., 2012. The modular endoprosthesis for mandibular body replacement. Part 2: Finite element analysis of endoprosthesis reconstruction of the mandible. *Journal of Cranio-Maxillofacial Surgery*, 40(8), pp.e487-e497.

Wilde, F., Hanken, H., Probst, F., Schramm, A., Heiland, M. and Cornelius, C., 2015. Multicenter study on the use of patient-specific CAD/CAM reconstruction plates for mandibular reconstruction. International Journal of Computer Assisted Radiology and Surgery, 10(12), pp.2035-2051.

Wood, W., Takada, K. and Hannam, A. (1986). The electromyographic activity of the inferior part of the human lateral pterygoid muscle during clenching and chewing. *Archives of Oral Biology*, 31(4), pp.245-253.

Wu, C., Lin, Y., Liu, Y. and Lin, C., 2017. Biomechanical evaluation of a novel hybrid reconstruction plate for mandible segmental defects: A finite element

Yamada, H., Nakaoka, K., Sonoyama, T., Kumagai, K., Ikawa, T., Shigeta, Y., Harada, N., Kawamura, N., Ogawa, T. and Hamada, Y. (2016). Clinical Usefulness of Mandibular Reconstruction Using Custom-Made Titanium Mesh Tray and Autogenous Particulate Cancellous Bone and Marrow Harvested from Tibia and/or Ilia. *Journal of Craniofacial Surgery*, 27(3), pp.586-592.

Yang, W., Choi, W., Leung, Y., Curtin, J., Du, R., Zhang, C., Chen, X. and Su, Y., 2018. Three-dimensional printing of patient-specific surgical plates in head and neck reconstruction: A prospective pilot study. *Oral Oncology*, 78, pp.31-36.

Zachow, S., Lamecker, H., Elsholtz, B. and Stiller, M. (2005). Reconstruction of mandibular dysplasia using a statistical 3d shape model. *International Congress Series, vol. 1281, pp. 1238 – 1243. ISSN 0531-5131. CARS 2005: Computer Assisted Radiology and Surgery.*

# Appendices

# Appendix A – Mandible Measurements

## A.1. Mandible Measurements

*Table A.1: Male Reconstruction Plate Measurements*

| Model # | Co_Go_R | Co_Go_L | Go_Sag_R | Go_Sag_L | Go_Me | Co_Sag_L | Co_Sag_R | Angle_R | Angle_L |
|---|---|---|---|---|---|---|---|---|---|
| **M1** | 28.08 | 29.78 | 26.4 | 51.73 | 86.033 | 51.26 | 52.6 | 111.5 | 117 |
| **M2** | 33.87 | 35.2 | 32.5 | 42.56 | 93.745 | 48.78 | 53.7 | 105.7 | 109 |
| **M3** | 24.24 | 24.42 | 24.1 | 48.27 | 85.955 | 51.06 | 51.9 | 114.5 | 115 |
| **M4** | 34.55 | 34.41 | 34.7 | 41.7 | 91.95 | 48.72 | 50.6 | 107.1 | 111 |
| **M5** | 29.09 | 27.53 | 30.7 | 40.8 | 82.766 | 47.09 | 48.9 | 116.6 | 116 |
| **M6** | 30.61 | 30.97 | 30.3 | 43.75 | 83.17 | 47.74 | 51.8 | 104.4 | 107 |
| **M7** | 23.02 | 27.29 | 29.2 | 50.34 | 93.835 | 52.61 | 51.5 | 107.5 | 100 |
| **M8** | 25.36 | 25.62 | 25.1 | 47.86 | 94.231 | 50.04 | 51.2 | 118.1 | 119 |
| **M9** | 32.83 | 30.8 | 34.9 | 51.1 | 85.735 | 52.95 | 49.5 | 120.4 | 114 |
| **M10** | 28.46 | 28.56 | 28.4 | 41.76 | 85.289 | 46.11 | 47.9 | 112.5 | 111 |
| **M11** | 29.82 | 28.44 | 27.3 | 46.35 | 80.142 | 48.49 | 50.2 | 116.9 | 120 |
| **M12** | 31.32 | 31.04 | 31.6 | 48.94 | 88.702 | 51.81 | 51.3 | 113.8 | 116 |
| **M13** | 27.93 | 28.57 | 27.3 | 45.93 | 86.041 | 49.26 | 49.3 | 120.9 | 115 |
| **M14** | 30.85 | 29.78 | 31.9 | 49.2 | 93.476 | 49.79 | 50 | 107.6 | 114 |
| **M15** | 30.57 | 29.95 | 31.2 | 43.04 | 83.393 | 46.25 | 47.8 | 115.2 | 115 |
| **M16** | 30.09 | 30.98 | 29.2 | 44.73 | 82.46 | 49.35 | 45.9 | 105 | 111 |
| **M17** | 25.76 | 25.36 | 26.1 | 40.96 | 88.004 | 48.18 | 50.9 | 105.4 | 111 |
| **M18** | 27.53 | 25.65 | 29.4 | 49.38 | 90.295 | 52.08 | 51.6 | 111.1 | 107 |
| **M19** | 27.62 | 34.73 | 31.4 | 48.14 | 86.899 | 50.92 | 53.5 | 111.8 | 112 |
| **M20** | 30.05 | 27.37 | 27 | 41.43 | 76.621 | 43.52 | 48.1 | 109 | 106 |
| **M21** | 28.06 | 26.75 | 25.7 | 52.41 | 88.159 | 52.12 | 52 | 100.4 | 102 |
| **M22** | 24.83 | 26.25 | 23.4 | 48.36 | 83.492 | 46.74 | 51.3 | 111.7 | 110 |
| **M23** | 26.21 | 25.79 | 26.6 | 49.33 | 97.323 | 49.92 | 49.3 | 108.2 | 106 |
| **M24** | 26.88 | 26.56 | 27.2 | 42.96 | 86.273 | 49.54 | 48.6 | 110.8 | 109 |
| **M25** | 24.3 | 23.36 | 25.2 | 50.9 | 89.285 | 54.11 | 51.8 | 109.6 | 108 |
| **M26** | 29 | 28.93 | 29.1 | 40.71 | 80.233 | 46.25 | 49.9 | 100.5 | 103 |
| **M27** | 25.88 | 21.66 | 30.1 | 40.89 | 89.735 | 45.16 | 49.1 | 109.2 | 111 |
| **M28** | 28.25 | 28.47 | 28 | 46.79 | 88.034 | 50.1 | 49.4 | 106.6 | 106 |
| **M29** | 24.79 | 22.57 | 27 | 47.9 | 93.473 | 50.45 | 50.1 | 111.3 | 106 |
| **M30** | 25.94 | 22.72 | 29.1 | 42.14 | 81.604 | 46.47 | 47.8 | 112.2 | 115 |
| **M31** | 26.92 | 25.06 | 28.8 | 48.78 | 80.091 | 47.08 | 48.3 | 108.9 | 112 |
| **M32** | 30.61 | 30.01 | 31.2 | 50.13 | 85.391 | 52.63 | 53.5 | 110.6 | 115 |
| **M33** | 26.71 | 23.98 | 29.4 | 40.51 | 85.548 | 46.93 | 47.7 | 101.4 | 105 |
| **M34** | 28.57 | 28.23 | 28.9 | 45.04 | 79.555 | 49.72 | 51.2 | 106.4 | 108 |
| **M35** | 33.34 | 35.57 | 31.1 | 42.68 | 84.502 | 46.63 | 52.4 | 107.8 | 108 |

| | | | | | | | | | |
|---|---|---|---|---|---|---|---|---|---|
| **M36** | 29.31 | 29.89 | 28.7 | 43.43 | 89.155 | 49.69 | 51.3 | 105.8 | 108 |
| **M37** | 31.51 | 25.61 | 26.8 | 50.08 | 84.559 | 51.23 | 47.9 | 117.9 | 116 |

*Table A.2: Female Reconstruction Plate Measurements*

| Model # | Co_Go_R | Co_Go_L | Go_Sag_R | Go_Sag_L | Go_Me | Co_Sag_L | Co_Sag_R | Angle_R | Angle_L |
|---|---|---|---|---|---|---|---|---|---|
| **F1** | 26.65 | 26.65 | 46.9 | 46.22 | 82.5 | 50 | 51.5 | 113 | 113 |
| **F2** | 25.28 | 25.28 | 45.3 | 47.29 | 87.623 | 50.8 | 49 | 115.9 | 116 |
| **F3** | 22.81 | 22.81 | 47.6 | 49.19 | 83.46 | 49.29 | 48.6 | 117.8 | 118 |
| **F4** | 27.48 | 27.48 | 44.5 | 42.91 | 88.46 | 51.26 | 51 | 102.8 | 109 |
| **F5** | 27.99 | 27.99 | 48.4 | 46.12 | 88.569 | 50.1 | 50.6 | 110 | 110 |
| **F6** | 29.8 | 29.8 | 46.4 | 49.57 | 90.802 | 54.5 | 50.3 | 113.9 | 108 |
| **F7** | 29.34 | 29.34 | 44 | 43.15 | 89.264 | 49.63 | 50.9 | 113.2 | 114 |
| **F8** | 30.04 | 31.46 | 45.7 | 44.38 | 84.384 | 47.82 | 46.8 | 104.9 | 104 |
| **F9** | 25.63 | 25.63 | 45.1 | 43.4 | 86.507 | 48.63 | 51.4 | 113 | 118 |
| **F10** | 27.61 | 27.61 | 47.6 | 47.41 | 90.216 | 50.68 | 51.7 | 118.5 | 114 |
| **F11** | 27.81 | 27.81 | 44.9 | 44.21 | 86.499 | 48.53 | 49.8 | 112.9 | 114 |
| **F12** | 33.65 | 33.65 | 49.6 | 47.49 | 86.299 | 45.31 | 48.2 | 101.2 | 103 |
| **F13** | 29.45 | 29.45 | 50.2 | 49.13 | 88.51 | 49.76 | 49.9 | 110 | 106 |
| **F14** | 27.15 | 27.15 | 50.5 | 51.85 | 89.675 | 54.09 | 52.8 | 113.5 | 114 |
| **F15** | 30.4 | 30.4 | 45.3 | 40.33 | 97.967 | 50.55 | 52.7 | 104.9 | 108 |
| **F16** | 26.07 | 26.07 | 42.4 | 42.96 | 82.268 | 48.95 | 47.4 | 117.2 | 121 |
| **F17** | 27.4 | 27.4 | 44.8 | 45.47 | 92.283 | 50.47 | 49.4 | 112.3 | 113 |
| **F18** | 26.42 | 26.42 | 42.7 | 41.89 | 86.159 | 47.69 | 46.4 | 107.4 | 106 |
| **F19** | 23.19 | 23.19 | 46.1 | 45.43 | 89.49 | 50.78 | 51 | 113.7 | 118 |
| **F20** | 29.33 | 29.33 | 44.9 | 43.57 | 97.676 | 49.39 | 50.4 | 110.6 | 110 |
| **F21** | 27.54 | 27.54 | 46 | 44.84 | 87.004 | 46.71 | 46.9 | 106.5 | 114 |
| **F22** | 26.91 | 26.91 | 44.9 | 42.83 | 80.166 | 44.98 | 46.4 | 113.2 | 114 |
| **F23** | 28.25 | 28.25 | 47.5 | 47.13 | 87.741 | 50.87 | 51.8 | 114.5 | 116 |
| **F24** | 27.6 | 27.6 | 43.9 | 42.06 | 91.165 | 48.83 | 50 | 106.8 | 114 |
| **F25** | 24.42 | 24.42 | 41.9 | 38.35 | 84.466 | 45.03 | 47.5 | 114.6 | 118 |
| **F26** | 28.54 | 28.54 | 45.4 | 48.32 | 81.251 | 50.48 | 47.9 | 118.9 | 110 |
| **F27** | 29.55 | 29.55 | 46.6 | 44.4 | 93.246 | 50.02 | 49.4 | 110.8 | 107 |
| **F28** | 27.09 | 27.09 | 45.7 | 45.5 | 86.773 | 48.05 | 50.1 | 114 | 115 |
| **F29** | 25.75 | 30 | 47.2 | 44.22 | 86.235 | 45.99 | 48.3 | 102 | 109 |
| **F30** | 28.21 | 28.21 | 47.9 | 47.97 | 96.35 | 51.6 | 51.3 | 113.3 | 113 |
| **F31** | 28.56 | 28.56 | 47.5 | 47.72 | 94.973 | 56.42 | 55.3 | 118.6 | 115 |
| **F32** | 28.62 | 28.62 | 45.8 | 45.7 | 81.681 | 47.91 | 48.6 | 109.8 | 109 |
| **F33** | 29.6 | 29.6 | 46.2 | 46.14 | 84.606 | 50.42 | 50.1 | 108.9 | 112 |
| **F34** | 20.53 | 20.53 | 45.2 | 44.05 | 87.843 | 47.79 | 48.8 | 113.8 | 116 |
| **F35** | 26.29 | 26.29 | 40.7 | 38.45 | 85.657 | 48.74 | 48.4 | 109.6 | 109 |
| **F36** | 28.33 | 28.33 | 44.4 | 44.08 | 95.651 | 54.03 | 53.1 | 112.2 | 114 |
| **F37** | 27.29 | 27.29 | 46.7 | 46.99 | 93.592 | 52.06 | 51 | 110.3 | 110 |

# Appendix B – Comparison Data

## B.1. Bland and Altman Plots

The following Figures are the Bland and Altman Plots for the Male Anatomical Measurements. The green bound is +2 σ, the red bound is the μ, the purple bound is -2 σ and the data is represented by blue points. 95 % of the data should lie between 2 σ either side of the mean. This allows for 2 irregular data points.

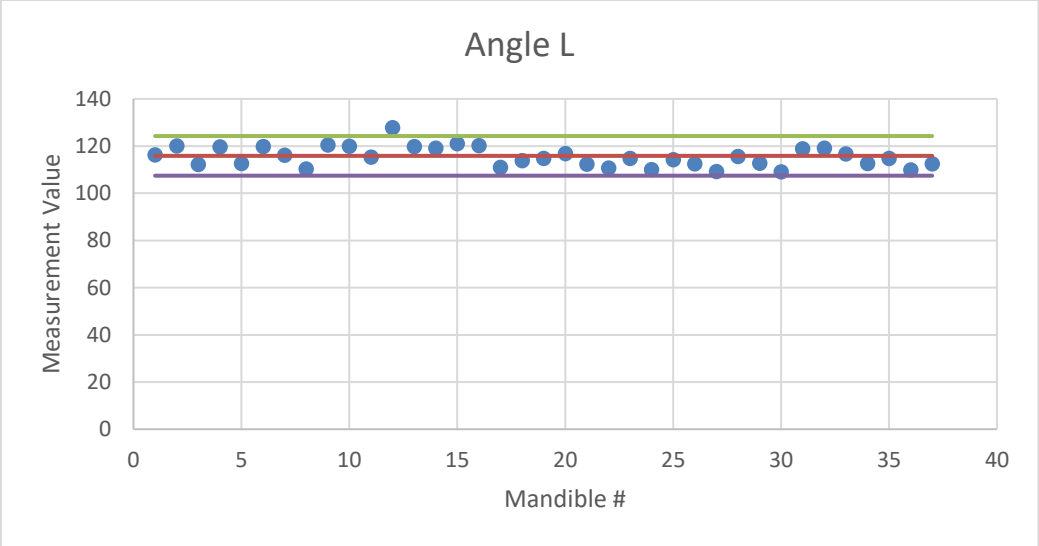


*Figure B.1: Angle L B&A Plot*

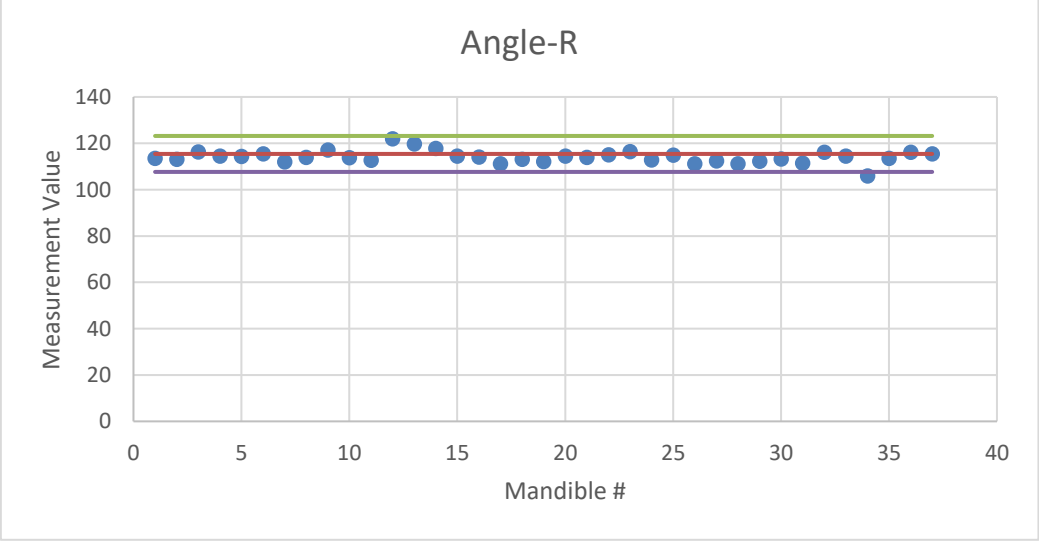


*Figure B.2: Angle R B&A Plot*

Appendix B – Comparison Data

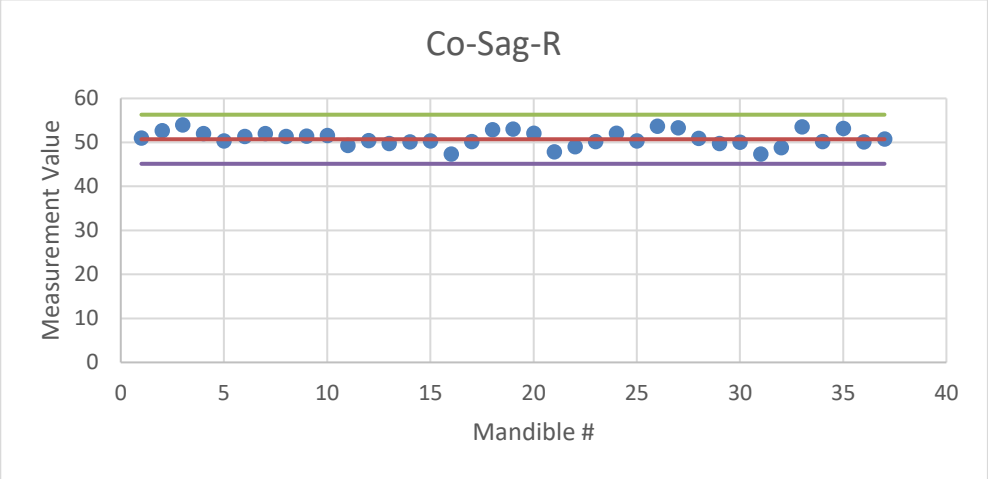


*Figure B.3: Co-Sag-R B&A Plot*

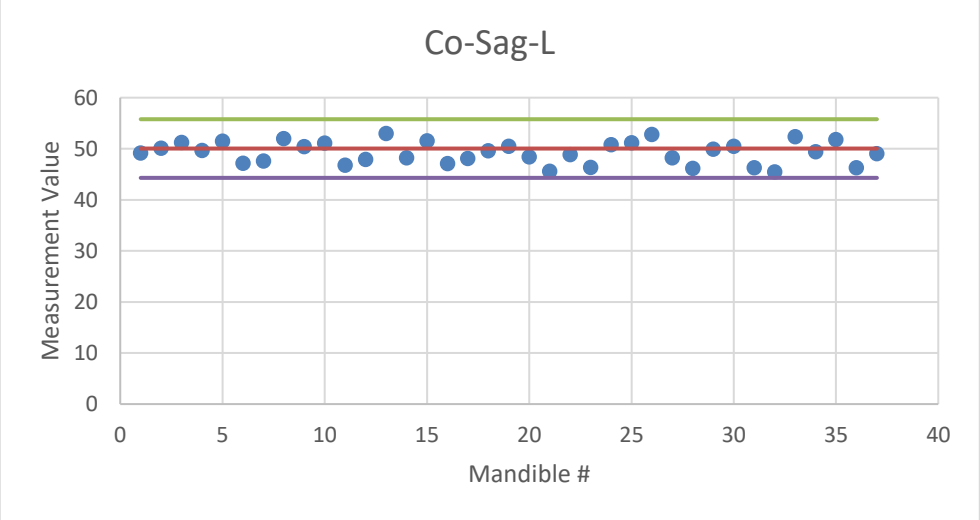


*Figure B.4: Co-Sag-L B&A Plot*

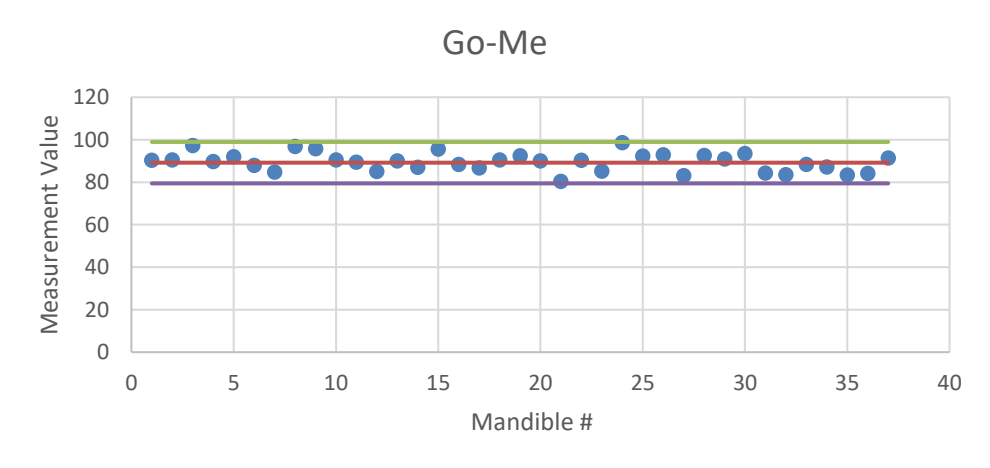


*Figure B.5: Go–Me B&A Plot*

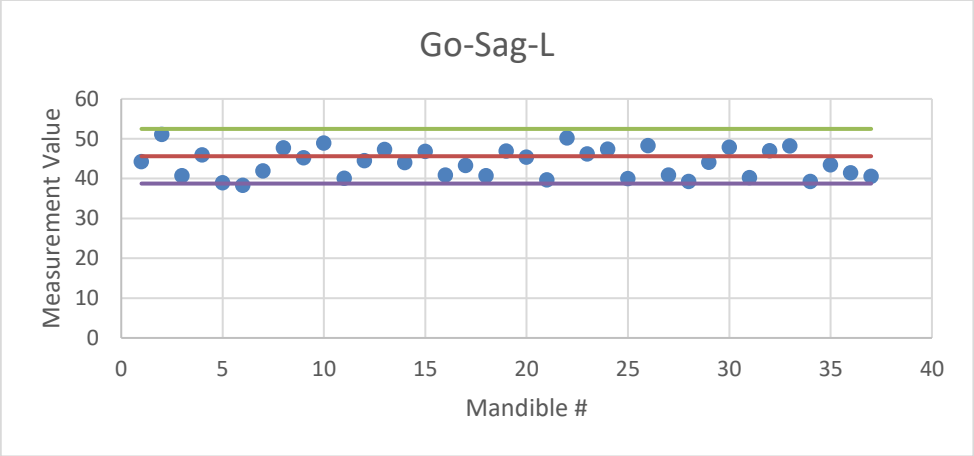


*Figure B.6: Go-Sag-L B&A Plot*

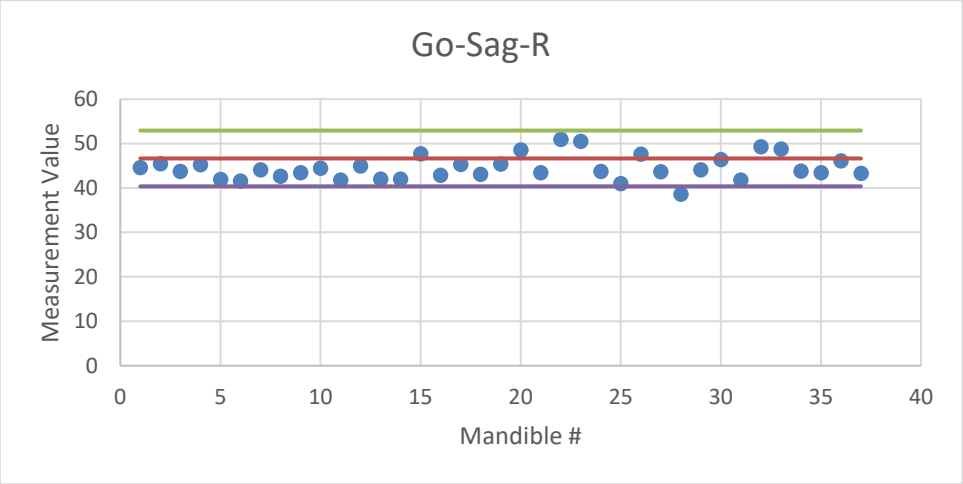


*Figure B.7: Go-Sag-R B&A Plot*

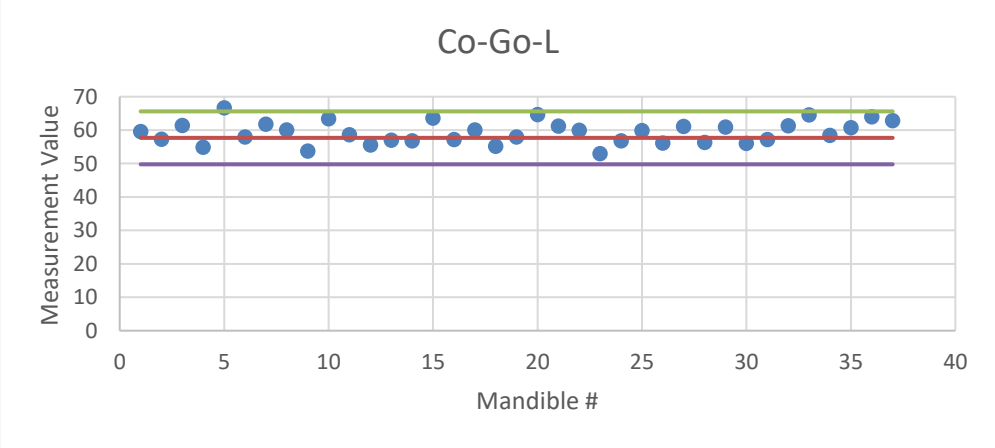


*Figure B.8: Co-Go-L B&A Plot*

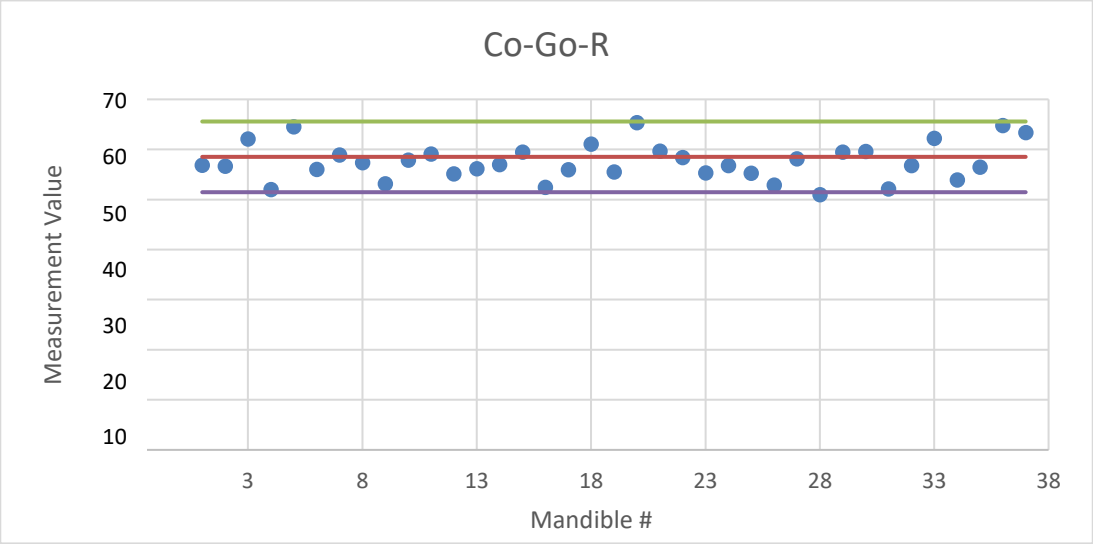


*Figure B.9: Co-Go-R B&A Plot*

## B.2. Hausdorff Measurements

The following tables include the Hausdorff distance measurements for each male and female mandible/plate configuration.

*Table B.1: Male Symphyseal Hausdorff distance Measurements*

| | Min | Max | Mean | RMS |
|---|---|---|---|---|
| **PF1** | 0.000366 | 3.438156 | 1.317881 | 1.611261 |
| **PF2** | 0.002853 | 5.585297 | 2.16949 | 2.627913 |
| **PF3** | 0.002327 | 5.347275 | 2.086699 | 2.540307 |
| **PF4** | 0.013466 | 4.516418 | 2.311718 | 2.574453 |
| **PF5** | 0.000824 | 5.40474 | 2.201498 | 2.707924 |
| **PF6** | 0.000755 | 5.009851 | 2.183258 | 2.520925 |
| **PF7** | 0.000481 | 3.776596 | 1.512946 | 1.827107 |
| **PF8** | 0.000671 | 3.716026 | 1.628941 | 1.974711 |
| **PF9** | 0.004112 | 4.644043 | 2.018403 | 2.427763 |
| **PF10** | 0.000397 | 4.795609 | 2.072819 | 2.41728 |
| **PF11** | 0.00132 | 4.393135 | 1.713377 | 2.057648 |
| **PF12** | 0.004578 | 5.451149 | 2.236324 | 2.630569 |
| **PF13** | 0.001206 | 4.80925 | 1.590303 | 1.959142 |
| **PF14** | 0.004784 | 5.952705 | 2.591688 | 3.090479 |
| **PF15** | 0.003441 | 4.629105 | 2.038162 | 2.375096 |
| **PF16** | 0.001907 | 5.484711 | 2.513055 | 2.902353 |
| **PF17** | 0.000114 | 4.021027 | 1.799655 | 2.102827 |
| **PF18** | 0.002403 | 3.893326 | 1.530116 | 1.843551 |
| **PF19** | 0.010597 | 5.380873 | 2.339916 | 2.738055 |
| **PF20** | 0.002411 | 5.181717 | 2.323884 | 2.734204 |
| **PF21** | 0.000031 | 4.623718 | 1.711509 | 2.054579 |

| | | | | |
|---|---|---|---|---|
| **PF22** | 0.002602 | 5.62117 | 2.519604 | 2.908766 |
| **PF23** | 0.003838 | 5.433624 | 1.864416 | 2.222146 |
| **PF24** | 0.002594 | 4.829133 | 2.01706 | 2.363467 |
| **PF25** | 0.000793 | 4.776772 | 1.884224 | 2.249104 |
| **PF26** | 0.00029 | 4.357483 | 1.631562 | 1.959375 |
| **PF27** | 0.003319 | 3.613754 | 1.622423 | 1.940946 |
| **PF28** | 0.011185 | 4.991119 | 1.918699 | 2.306919 |
| **PF29** | 0.003273 | 4.913239 | 2.168622 | 2.516784 |
| **PF30** | 0.000168 | 4.519897 | 2.103525 | 2.454135 |
| **PF31** | 0.001625 | 4.311646 | 1.606153 | 1.912348 |
| **PF32** | 0.000771 | 3.99888 | 1.642926 | 1.949326 |
| **PF33** | 0.000839 | 4.461417 | 1.922955 | 2.241232 |
| **PF34** | 0.001404 | 4.720982 | 1.65111 | 1.936447 |
| **PF35** | 0.002892 | 4.651214 | 2.117688 | 2.467759 |
| **PF36** | 0.004135 | 4.014893 | 1.939842 | 2.250079 |
| **PF37** | 0.003998 | 4.669387 | 1.669286 | 2.028186 |

*Table B.2: Male Hemimandible Hausdorff distance Measurements*

| | **Min** | **Max** | **Mean** | **RMS** |
|---|---|---|---|---|
| **PH1** | 0.004364 | 8.895209 | 2.966452 | 3.60442 |
| **PH2** | 0.009949 | 8.962955 | 3.16604 | 3.74248 |
| **PH3** | 0.018097 | 6.971642 | 2.626618 | 3.080611 |
| **PH4** | 0.008606 | 5.334435 | 1.978074 | 2.377405 |
| **PH5** | 0.012093 | 7.326405 | 2.638556 | 3.139935 |
| **PH6** | 0.010601 | 6.330933 | 3.03249 | 3.430353 |
| **PH7** | 0.00061 | 5.838379 | 2.791928 | 3.169626 |
| **PH8** | 0.011543 | 5.51408 | 2.295424 | 2.706886 |
| **PH9** | 0.008583 | 4.901054 | 2.18929 | 2.550779 |
| **PH10** | 0.006729 | 6.280205 | 2.418395 | 2.872275 |
| **PH11** | 0.019051 | 6.33675 | 2.586843 | 2.967469 |
| **PH12** | 0.055031 | 6.08709 | 2.206662 | 3.549978 |
| **PH13** | 0.000496 | 6.106689 | 2.395758 | 2.823539 |
| **PH14** | 0.001213 | 7.230324 | 2.399319 | 2.943058 |
| **PH15** | 0.002377 | 6.193825 | 2.589134 | 2.995293 |
| **PH16** | 0.008926 | 7.302078 | 2.115837 | 2.736536 |
| **PH17** | 0.007565 | 5.864227 | 2.050996 | 2.529732 |
| **PH18** | 0.002823 | 5.93861 | 2.156705 | 2.569785 |
| **PH19** | 0.006107 | 6.038795 | 2.71488 | 3.174503 |
| **PH20** | 0.005264 | 6.329498 | 2.999615 | 3.360125 |
| **PH21** | 0.000601 | 7.916016 | 3.13238 | 3.664813 |
| **PH22** | 0.006638 | 4.747231 | 2.555691 | 2.808642 |
| **PH23** | 0.001495 | 5.679344 | 2.320525 | 2.770413 |

| | | | | |
|---|---|---|---|---|
| **PH24** | 0.821053 | 6.397935 | 2.896289 | 3.245281 |
| **PH25** | 0.003487 | 7.324038 | 2.928658 | 3.528547 |
| **PH26** | 0.002747 | 7.084412 | 2.503854 | 3.021878 |
| **PH27** | 0.004955 | 6.023712 | 1.960006 | 2.42266 |
| **PH28** | 0.000168 | 6.73423 | 2.946074 | 3.410757 |
| **PH29** | 0.003502 | 7.563538 | 2.630166 | 3.260622 |
| **PH30** | 0.001671 | 4.84172 | 2.026529 | 2.44119 |
| **PH31** | 0.002853 | 5.416193 | 2.478565 | 2.877563 |
| **PH32** | 0.000175 | 6.427597 | 2.499472 | 3.022187 |
| **PH33** | 0.007355 | 6.918867 | 2.665767 | 3.045491 |
| **PH34** | 0.002174 | 6.878247 | 2.642482 | 3.166642 |
| **PH35** | 0.022697 | 6.673141 | 2.690925 | 3.17107 |
| **PH36** | 0.001015 | 7.507118 | 2.228595 | 2.801908 |
| **PH37** | 0.018147 | 6.425667 | 3.09095 | 3.451109 |

*Table B.3: Male Lateral Short Hausdorff distance Measurements*

| | **Min** | **Max** | **Mean** | **RMS** |
|---|---|---|---|---|
| **PS1** | 0.01442 | 4.631393 | 1.969252 | 2.306046 |
| **PS2** | 0.010483 | 4.315224 | 2.102513 | 2.41793 |
| **PS3** | 0.029381 | 5.00631 | 2.335996 | 2.613758 |
| **PS4** | 0.00354 | 5.349129 | 1.776837 | 2.183503 |
| **PS5** | 0.131699 | 6.071587 | 2.372815 | 2.748716 |
| **PS6** | 0.245064 | 5.797707 | 2.354926 | 2.682329 |
| **PS7** | 0.002693 | 4.967979 | 1.743097 | 2.095415 |
| **PS8** | 0.032112 | 4.889883 | 1.912395 | 2.240262 |
| **PS9** | 0.000732 | 4.281727 | 1.916578 | 2.236677 |
| **PS10** | 0.00384 | 4.721585 | 1.738982 | 2.206851 |
| **PS11** | 0.004776 | 4.854859 | 1.584524 | 1.944677 |
| **PS12** | 0.251049 | 4.713631 | 2.462183 | 2.713631 |
| **PS13** | 0.001556 | 3.925354 | 1.851102 | 2.159301 |
| **PS14** | 0.003967 | 5.070419 | 1.625873 | 2.022014 |
| **PS15** | 0.007713 | 4.386818 | 1.695574 | 2.030359 |
| **PS16** | 0.001022 | 4.110622 | 1.351625 | 1.637307 |
| **PS17** | 0.003693 | 4.428581 | 1.592563 | 1.938922 |
| **PS18** | 0.001503 | 4.143379 | 1.528713 | 1.878009 |
| **PS19** | 0.048386 | 5.043228 | 2.062747 | 2.416296 |
| **PS20** | 0.005135 | 4.779678 | 1.63962 | 1.982531 |
| **PS21** | 0.003021 | 3.517863 | 1.240103 | 1.474419 |
| **PS22** | 0.001183 | 4.516808 | 1.882538 | 2.222578 |
| **PS23** | 0.000694 | 4.733498 | 2.198346 | 2.523305 |
| **PS24** | 0.005791 | 4.870274 | 1.784013 | 2.132652 |
| **PS25** | 0.01049 | 4.352699 | 1.84722 | 2.177125 |
| **PS26** | 0.123339 | 3.820381 | 1.806981 | 2.127732 |

| | | | | |
|---|---|---|---|---|
| **PS27** | 0.00563 | 4.672467 | 1.764439 | 2.135415 |
| **PS28** | 0.001221 | 3.891373 | 1.475758 | 1.807759 |
| **PS29** | 0.016983 | 4.37616 | 1.931516 | 2.240597 |
| **PS30** | 0.008423 | 3.207123 | 1.151084 | 1.356321 |
| **PS31** | 0.002197 | 5.06292 | 2.281187 | 2.601407 |
| **PS32** | 0.000633 | 4.626755 | 1.511602 | 1.871829 |
| **PS33** | 0.00016 | 4.538799 | 1.495 | 1.828272 |
| **PS34** | 0.000946 | 5.768452 | 1.972871 | 2.414957 |
| **PS35** | 0.007774 | 4.327927 | 1.709131 | 2.04093 |
| **PS36** | 0.003832 | 4.115108 | 1.737343 | 2.082647 |
| **PS37** | 0.00946 | 5.341995 | 2.09278 | 2.436778 |

*Table B.4: Female Symphyseal Hausdorff distance Measurements*

| | **Min** | **Max** | **Mean** | **RMS** |
|---|---|---|---|---|
| **PF1** | 0.000809 | 4.152084 | 1.763151 | 2.0718 |
| **PF2** | 0.004074 | 4.754108 | 2.103801 | 2.4046 |
| **PF 3** | 0.000731 | 4.745557 | 2.056382 | 2.46850 |
| **PF4** | 0.009 | 4.176666 | 1.849742 | 2.194005 |
| **PF5** | 0.000465 | 4.252769 | 1.715314 | 2.00701 |
| **PF6** | 0.001678 | 3.835663 | 1.64104 | 1.935021 |
| **PF7** | 0.000259 | 4.299808 | 1.821094 | 2.127959 |
| **PF8** | 0.002487 | 4.130829 | 1.74493 | 2.032393 |
| **PF9** | 0.001827 | 4.22041 | 1.450228 | 2.339042 |
| **PF10** | 0.001053 | 3.713654 | 1.627889 | 1.941018 |
| **PF11** | 0.001648 | 3.611826 | 1.435479 | 1.69936 |
| **PF12** | 0.002289 | 3.651108 | 1.375392 | 1.616559 |
| **PF13** | 0.000122 | 4.818474 | 1.713337 | 2.064148 |
| **PF14** | 0.000122 | 4.276978 | 1.697927 | 2.004796 |
| **PF15** | 0.001328 | 4.96048 | 2.113095 | 2.436518 |
| **PF16** | 0.001686 | 3.961502 | 1.602284 | 1.891321 |
| **PF17** | 0.004807 | 3.754387 | 1.708448 | 2.0468 |
| **PF18** | 0.004639 | 3.53318 | 1.678348 | 1.962808 |
| **PF19** | 0.000153 | 4.42041 | 1.868935 | 2.229083 |
| **PF20** | 0.001717 | 4.376511 | 1.915312 | 2.239042 |
| **PF21** | 0.01268 | 4.331772 | 1.874742 | 2.19414 |
| **PF22** | 0.002625 | 4.008596 | 1.851582 | 2.146397 |
| **PF23** | 0.006302 | 3.423269 | 1.394706 | 1.658296 |
| **PF24** | 0.003006 | 4.499603 | 1.96658 | 2.348901 |
| **PF25** | 0.00145 | 3.600804 | 1.515163 | 1.809566 |
| **PF26** | 0.005913 | 3.733093 | 1.905628 | 2.218453 |
| **PF27** | 0.003693 | 4.408478 | 2.150714 | 2.453181 |
| **PF28** | 0.010803 | 4.561943 | 2.280549 | 2.551992 |
| **PF29** | 0.001114 | 4.795364 | 2.555768 | 2.821031 |

| | | | | |
|---|---|---|---|---|
| **PF30** | 0.002518 | 4.709747 | 2.002233 | 2.329027 |
| **PF31** | 0.000256 | 4.632904 | 1.745586 | 2.069311 |
| **PF32** | 0.001816 | 4.548018 | 1.950351 | 2.272766 |
| **PF33** | 0.006958 | 3.653915 | 1.727666 | 2.035934 |
| **PF34** | 0.009827 | 4.935684 | 2.383519 | 2.728921 |
| **PF35** | 0.005005 | 4.387001 | 1.726446 | 1.986091 |
| **PF36** | 0.002319 | 3.915878 | 1.972328 | 2.287274 |
| **PF37** | 0.004837 | 4.839996 | 2.151464 | 2.461381 |

*Table B.5: Female Hemimandible Hausdorff distance Measurements*

| | **Min** | **Max** | **Mean** | **RMS** |
|---|---|---|---|---|
| **PH1** | 0.004795 | 6.066101 | 2.442384 | 2.84833 |
| **PH2** | 0.01368 | 5.897686 | 2.251761 | 2.631138 |
| **PH3** | 0.005007 | 6.277131 | 2.174722 | 2.452759 |
| **PH4** | 0.001701 | 5.188748 | 2.468113 | 1.935654 |
| **PH5** | 0.009151 | 5.178146 | 2.281277 | 2.675516 |
| **PH6** | 0.002235 | 5.632839 | 2.761127 | 2.206249 |
| **PH7** | 0.006721 | 6.599762 | 2.348099 | 2.778007 |
| **PH8** | 0.000309 | 5.473343 | 2.099691 | 2.530463 |
| **PH9** | 0.004775 | 5.157932 | 2.326466 | 2.74833 |
| **PH10** | 0.003536 | 5.176811 | 1.543029 | 1.939015 |
| **PH11** | 0.001305 | 5.250824 | 2.39039 | 2.739501 |
| **PH12** | 0.000076 | 4.587357 | 1.795968 | 2.144351 |
| **PH13** | 0.000046 | 4.894126 | 1.663699 | 2.06017 |
| **PH14** | 0.000717 | 5.436577 | 1.987224 | 2.403313 |
| **PH15** | 0.000496 | 5.570786 | 2.426466 | 2.616446 |
| **PH16** | 0.002365 | 5.52166 | 2.004636 | **2.523825** |
| **PH17** | 0.006943 | 5.457932 | 2.016523 | 2.419749 |
| **PH18** | 0.002556 | 5.583664 | 2.037845 | 2.477534 |
| **PH19** | 0.001812 | 5.110199 | 2.689089 | 3.280362 |
| **PH20** | 0.005703 | 5.556899 | 2.554343 | 3.09053 |
| **PH21** | 0.003281 | 5.599383 | 2.132378 | 2.569642 |
| **PH22** | 0.004181 | 6.147425 | 2.246523 | 2.730116 |
| **PH23** | 0.012306 | 4.828278 | 2.06778 | 2.464298 |
| **PH24** | 0.003929 | 6.157776 | 2.646521 | 3.145358 |
| **PH25** | 0.005775 | 6.924671 | 2.442351 | 2.882001 |
| **PH26** | 0.000229 | 4.410568 | 1.989968 | 2.35411 |
| **PH27** | 0.000923 | 5.999672 | 2.881267 | 3.307516 |
| **PH28** | 0.00322 | 6.886307 | 2.897972 | 3.41707 |
| **PH29** | 0.002777 | 4.82193 | 1.70928 | 2.086529 |
| **PH30** | 0.020988 | 5.471917 | 2.432242 | 2.748631 |
| **PH31** | 0.002274 | 6.773418 | 2.359815 | 2.833232 |
| **PH32** | 0.001747 | 5.229274 | 2.040659 | 2.453879 |

| | | | | |
|---|---|---|---|---|
| **PH33** | 0.01569 | 6.5634 | 2.706011 | 3.219332 |
| **PH34** | 0.006615 | 6.788269 | 2.685069 | 3.433079 |
| **PH35** | 0.266945 | 7.400177 | 3.533792 | 3.990921 |
| **PH36** | 0.010929 | 7.016415 | 3.07893 | 3.607447 |
| **PH37** | 0.006145 | 7.385227 | 3.098706 | 3.585969 |

*Table B.6: Female Lateral Short Hausdorff distance Measurements*

| | **Min** | **Max** | **Mean** | **RMS** |
|---|---|---|---|---|
| **PS1** | 0.00132 | 4.292313 | 1.903774 | 2.289173 |
| **PS2** | 0.003952 | 4.677803 | 1.582753 | 1.974557 |
| **PS3** | 0.025457 | 3.770939 | 1.391188 | 2.427809 |
| **PS4** | 0.002026 | 4.217951 | 1.558618 | 1.91533 |
| **PS5** | 0.004143 | 3.935941 | 1.547903 | 1.944782 |
| **PS6** | 0.007431 | 4.028679 | 1.555371 | 1.893773 |
| **PS7** | 0.008289 | 4.059493 | 1.520565 | 1.885422 |
| **PS8** | 0.005684 | 4.757561 | 1.865546 | 2.212966 |
| **PS9** | 0.00205 | 4.561214 | 2.13028 | 2.501125 |
| **PS10** | 0.000137 | 2.643822 | 1.201074 | 1.441862 |
| **PS11** | 0.000763 | 4.1007 | 1.711712 | 2.071816 |
| **PS12** | 0.000114 | 4.409042 | 1.474082 | 1.783581 |
| **PS13** | 0.00029 | 4.361214 | 1.69875 | 2.06356 |
| **PS14** | 0.013054 | 4.300125 | 1.758413 | 2.097086 |
| **PS15** | 0.006195 | 3.670939 | 1.326522 | 1.634623 |
| **PS16** | 0.011131 | 3.069481 | 1.191188 | 1.455243 |
| **PS17** | 0.001205 | 3.076736 | 1.237613 | 1.504452 |
| **PS18** | 0.022263 | 4.421326 | 1.70492 | 2.055668 |
| **PS19** | 0.020752 | 3.765457 | 1.676256 | 2.014594 |
| **PS20** | 0.002163 | 3.687789 | 1.48356 | 1.872413 |
| **PS21** | 0.001686 | 4.567524 | 1.855962 | 2.201125 |
| **PS22** | 0.015457 | 4.308952 | 1.95973 | 2.266106 |
| **PS23** | 0.004837 | 4.256218 | 1.833806 | 2.168895 |
| **PS24** | 0.022133 | 4.611099 | 1.782116 | 2.147366 |
| **PS25** | 0.003021 | 3.912674 | 2.03028 | 2.320925 |
| **PS26** | 0.013313 | 3.776871 | 1.752794 | 2.073742 |
| **PS27** | 0.002838 | 3.797882 | 1.490663 | 1.846572 |
| **PS28** | 0.00267 | 3.768852 | 1.610515 | 1.953826 |
| **PS29** | 0.003586 | 4.079007 | 1.768242 | 2.136593 |
| **PS30** | 0.012577 | 3.565903 | 1.650169 | 1.981882 |
| **PS31** | 0.003838 | 4.228577 | 1.720117 | 2.064489 |
| **PS32** | 0.008583 | 4.756256 | 1.806889 | 2.127809 |
| **PS33** | 0.024811 | 3.987854 | 1.543655 | 1.857157 |
| **PS34** | 0.00288 | 4.66717 | 1.689581 | 2.055566 |
| **PS35** | 0.025246 | 3.954597 | 1.710004 | 2.086021 |

Appendix B – Comparison Data

| | | | | |
|---|---|---|---|---|
| **PS36** | 0.001717 | 4.024094 | 2.117558 | 2.53408 |
| **PS37** | 0.00518 | 4.141372 | 1.596621 | 2.001671 |

# Appendix C - Model Validation Data

## C.1. Vector Tables

*Table C.1: Male Boundary Condition Vectors*

| | Positional Vectors | | | Muscle Force Vectors | | |
|---|---|---|---|---|---|---|
| | x | y | z | x | y | z |
| **Left Fixed Support** | -8.83E+01 | -1.64E+01 | 7.47E+01 | | | |
| **Right Fixed Support** | 11.13 | -20.9 | 64.91 | | | |
| **Right Deep Masseter** | 1.58E+00 | -1.29E+01 | 1.06E+01 | 7.78E+00 | 2.27E+01 | 1.27E+02 |
| **Right Temporalis** | 3.92E+00 | 9.14E+00 | 4.55E+01 | 6.40E-02 | 1.21E+01 | 1.84E+02 |
| **Right Superficial Masseter** | 5.40E+00 | -2.29E+01 | 2.33E+01 | 1.29E+01 | -7.73E+01 | 2.38E+02 |
| **Right Medial Pterygoid** | -1.30E-01 | -2.20E+01 | 2.53E+01 | 1.40E+02 | -1.30E-01 | 3.70E-01 |
| **Right Medial Temporalis** | -2.05E+00 | -5.31E+00 | 3.87E+01 | 9.70E-01 | -7.44E+00 | 5.68E+00 |
| **Left Deep Masseter** | -7.67E+01 | -2.69E+01 | 1.58E+01 | 7.78E+00 | 2.27E+01 | 1.27E+02 |
| **Left Temporalis** | -7.92E+01 | 9.41E+00 | 4.97E+01 | 6.40E-02 | 1.21E+01 | 1.84E+02 |
| **Left Superficial Masseter** | -8.22E+01 | -2.96E+01 | 2.69E+01 | 1.29E+01 | -7.73E+01 | 2.38E+02 |
| **Left Medial Pterygoid** | -7.22E+01 | -1.79E+01 | 1.13E+01 | 1.40E+02 | -1.30E-01 | 3.70E-01 |
| **Left Medial Temporalis** | -7.92E+01 | 9.41E+00 | 4.97E+01 | 9.70E-01 | -7.44E+00 | 5.68E+00 |

*Table C.2: Female Boundary Condition Vectors*

| | Postional Vectors | | | Muscle Vectors | | |
|---|---|---|---|---|---|---|
| | x | y | z | x | y | z |
| **Left Fixed Support** | -8.83E+01 | -1.64E+01 | 7.47E+01 | | | |
| **Right Fixed Support** | 11.13 | -20.9 | 64.91 | | | |
| **Right Deep Masseter** | 3.63E+00 | -8.90E+00 | 2.38E+01 | 7.78E+00 | 2.27E+01 | 1.27E+02 |
| **Right Temporalis** | 1.93E+00 | 1.09E+01 | 6.49E+01 | 6.40E-02 | 1.21E+01 | 1.84E+02 |
| **Right Superficial Masseter** | -3.53E+00 | -2.15E+01 | 2.91E+01 | 1.29E+01 | -7.73E+01 | 2.38E+02 |
| **Right Medial Pterygoid** | -7.04E+00 | -2.28E+01 | 3.16E+01 | 1.40E+02 | -1.30E-01 | 3.70E-01 |
| **Right Medial Temporalis** | 1.93E+00 | 1.09E+01 | 6.49E+01 | 9.70E-01 | -7.44E+00 | 5.68E+00 |
| **Left Deep Masseter** | -7.89E+01 | -4.64E+00 | 1.32E+01 | 7.78E+00 | 2.27E+01 | 1.27E+02 |
| **Left Temporalis** | -8.71E+01 | 1.12E+01 | 6.68E+01 | 6.40E-02 | 1.21E+01 | 1.84E+02 |
| **Left Superficial Masseter** | -8.10E+01 | -1.89E+01 | 2.11E+01 | 1.29E+01 | -7.73E+01 | 2.38E+02 |
| **Left Medial Pterygoid** | -7.67E+01 | -7.89E+00 | 2.20E+01 | 1.40E+02 | -1.30E-01 | 3.70E-01 |
| **Left Medial Temporalis** | -8.71E+01 | 1.12E+01 | 6.68E+01 | 9.70E-01 | -7.44E+00 | 5.68E+00 |

*Table C.3: Male Positional Vectors*

| Vector Right | x | y | z | Vector Left | x | y | z |
|---|---|---|---|---|---|---|---|
| **rDRL** | -8.99E+01 | -3.55E+00 | 6.41E+01 | **rDRR** | 9.55E+00 | -8.05E+00 | 5.44E+01 |
| **rTRL** | -9.23E+01 | -2.55E+01 | 2.91E+01 | **rTRR** | 7.21E+00 | -3.00E+01 | 1.94E+01 |
| **rSRL** | -9.37E+01 | 6.53E+00 | 5.14E+01 | **rSRR** | 5.73E+00 | 2.03E+00 | 4.16E+01 |
| **rPRL** | -8.82E+01 | 5.56E+00 | 4.94E+01 | **rPRR** | 1.13E+01 | 1.06E+00 | 3.97E+01 |
| **rMRL** | -8.63E+01 | -1.11E+01 | 3.60E+01 | **rMRR** | 1.32E+01 | -1.56E+01 | 2.62E+01 |
| **rDLL** | -1.16E+01 | 1.05E+01 | 5.89E+01 | **rDLR** | 8.78E+01 | 5.04E+00 | 4.91E+01 |
| **rTLL** | -9.11E+00 | -1.98E+01 | 2.50E+01 | **rTLR** | 9.04E+01 | 2.03E+01 | 1.53E+01 |
| **rSLL** | -6.18E+00 | 3.32E+01 | 4.78E+01 | **rSLR** | 9.33E+01 | 8.71E+00 | 3.80E+01 |
| **rPLL** | -1.61E+01 | 3.53E+00 | 6.34E+01 | **rPLR** | 8.34E+01 | -2.97E+00 | 5.37E+01 |
| **rMLL** | -9.11E+00 | -5.81E+00 | 2.50E+01 | **rMLR** | 9.04E+01 | -3.03E+01 | 1.53E+01 |

*Table C.4: Female Positional Vectors*

| Vector Right | x | y | z | Vector Left | x | y | z |
|---|---|---|---|---|---|---|---|
| **rDRL** | -9.20E+01 | -7.50E+00 | 5.09E+01 | **rDRR** | 9.50E+00 | 1.20E+01 | 4.11E+01 |
| **rTRL** | -2.03E+01 | -2.73E+01 | 9.82E+00 | **rTRR** | 7.20E+00 | -4.18E+01 | 6.00E-02 |
| **rSRL** | -8.48E+01 | -5.06E+00 | 4.55E+01 | **rSRR** | 1.47E+01 | -5.60E-01 | 3.58E+01 |
| **rPRL** | -8.13E+01 | 6.36E+00 | 4.31E+01 | **rPRR** | 1.82E+01 | -8.60E-01 | 3.33E+01 |
| **rMRL** | -8.13E+01 | 6.36E+00 | 4.31E+01 | **rMRR** | 9.20E+00 | -3.18E+01 | 6.00E-02 |
| **rDLL** | -9.47E+00 | -1.18E+01 | 6.15E+01 | **rDLR** | 9.00E+01 | -1.63E+01 | 5.18E+01 |
| **rTLL** | 3.20E+00 | -7.76E+01 | 7.87E+00 | **rTLR** | 9.83E+01 | -3.21E+01 | -1.89E+00 |
| **rSLL** | 9.38E+00 | 2.47E+00 | 5.36E+01 | **rSLR** | 9.21E+01 | -2.03E+00 | 4.38E+01 |
| **rPLL** | 1.16E+01 | -8.51E+00 | 5.27E+01 | **rPLR** | 8.79E+01 | -1.30E+01 | -2.29E+01 |
| **rMLL** | 1.12E+01 | 2.76E+01 | 7.87E+00 | **rMLR** | 9.83E+01 | -3.21E+01 | -1.89E+00 |

Each vector, in Table C.3 and C.4, was given abbreviations to reduce the risk of making a mistake during the calculation process as well as transferring the vectors into MATLAB. The lowercase “r” is the positional vector designation, the following two letters stand for the muscle. Where, DR – Deep Masseter Right, TR – Temporalis Right, SR – Superficial Masseter Right, PR – Medial Pterygoid Right, MR – Medial Temporalis Right etc. The final letter refers to the left or right fixed support, L means the right support is suppressed and the moments are calculated about the Left support, and vice-versa.